SYNTHESIS AND CHARACTERIZATION OF DOWN−CONVERSION NANOPHOSPHORS

by

Kamohelo George Tshabalala

(MSc)

A thesis submitted in fulfillment of the requirements for the degree

PHILOSOPHIAE DOCTOR

in the

Faculty of Natural and Agricultural Sciences

Department of Physics/Fisika

at the

University of the Free State

Promoter: **Professor. O.M. Ntwaeaborwa**

Co-Promoter: **Professor. H.C. Swart**

October 2014

UNIVERSITY OF THE FREE STATE
UNIVERSITEIT VAN DIE VRYSTAAT
YUNIVESITHI YA FREISTATA

UFS·UV
NATURAL AND AGRICULTURAL SCIENCES
NATUUR- EN LANDBOUWETENSKAPPE

Dedicated to the memory of my mom the late

Nomvula Martha Tshabalala

(1958−2007)

DECLARATION

I, the undersigned, hereby declare that the work contained in this thesis is my own original work except as indicated in the references. It has not been submitted before for any degree or examination in this or any other university.

-Kamohelo George Tshabalala-

Signed at ……

On the …….. day of …… 2014

ACKNOWLEDGEMENTS

First, I would like to acknowledge my intellectual advisor and mentor, Professor Martin Odirileng Ntwaeaborwa for his unconditional guidance, support, advice, lessons in research (and also in life) and especially his patience during my whole doctoral study. I have considered him to be one of the greatest teachers and role models around. I feel very fortunate to have the opportunity to work under his tutelage.

To Professor Hendrik, Swart my co-promoter and former Head of the Department of Physics. I am deeply honored for your outstanding leadership, securing funding in many ways and making sure that this study was completed without any financial burdens.

Over and above that, thanks should be given to Dr. So-Hye Cho (KIST, South Korea –Seoul) and the research members in her group during the preparation of the samples and their hospitality during my sojourn at the Institute-South Korea in 2010 and 2011. To Dr. Jong-Ku Park, I have no words to describe how grateful I am for allowing me the lifetime opportunity to be part of the South Africa – South Korea Collaboration team in my doctoral study. A million thanks are duly summoned to you!

To all the members of Phosphor, NRG groups and former Post docs, more especially Drs Shreyas and Indrajit. I would like to say thank you so much for availing yourselves during some robust discussions about the subject of Luminescence and invaluable guidance during the preparation of the materials and manuscripts.

I would like to thank all of the members of Prof. J.R Botha's group at NMMU Physics Department. I think they are great bunches who are kind and willing to help each other whenever help is needed during PL measurements using a Laser system (He-Cd laser).

To the late Dr Jappie Dolo, former subject head at the Qwa-Qwa campus and the entire staff in the Physics Department where I am currently working, I would like to say thank you like I have never said it before. You have been wonderful indeed from the first

day I joined your department as a Lecturer. Keep up the good work and the wheels of unearthing new talent from young emerging researchers rolling. I am also thankful to both my parents. I particularly owe my late mother *Martha Nomvula Tshabalala* (1958 – 2007) a big thank you for all the support that she gave me since I started my university studies way back in Qwa-Qwa and Western Cape where I received my BSc and Masters degrees to date when I am now done with my PhD. I wish to state that though neither of my parents received as much education as I have, throughout this journey they have always been a source of inspiration for me. When reading for my PhD, whenever I visited my home town *Thaba-Bosiu Village,* each time I thought about coming back to Bloemfontein to resume my studies was always a painful thing for me. But grandmother on behalf of my mother who passed on in 2007 always gave me that warm motherly encouragement. Repeatedly, she assured me that someday I would get done with my studies. I also thank my siblings Mangaka, Makhoba, Monicca, Sipho"*zinja*", Lindiwe "*mbode*"and Tshepo for their support in various ways. To my best friends, Prof Simon Dhlamini, Dr Patrick Nsimama, Dr Joseph Hato, Tholoana, Dr Bataung Kunene, Palo, Maibi, Mamoqebelo, Molise Habasisa and Dr Lukisi Masiteng, thank you so much for your valuable support when I needed you.

I really want to express my gratitude to Malekgotla Mokoena, Tumelo Tshepiso, Paballo Lethabo Sabata, Bohlokwa and Siyanda, for their everlasting support, understanding and especially everyday prayers for me. To the towering and prolific English Lecturer Mr Mathobela MV, thanks very much for taking out your precious time to proof read my thesis. To Nontombi Velelo, thanks a lot for some life lessons and teaching me the power of prayer.

This project would not have been possible without generous funding from the Physics Department (UFS); South African National Research Foundation (NRF), National Research Foundation of Korea and Nanomaterials Cluster fund of the University of the Free State. Over and above that, I would like to thank GOD for allowing me this wonderful opportunity to remain intact and standing through thick and thin in this milestone journey.

ABSTRACT

SYNTHESIS AND CHARACTERIZATION OF DOWN-CONVERTING NANOPHOSPHORS

Tshabalala, Kamohelo George

PhD Thesis, Department of Physics, University of the Free State

Luminescent zinc aluminate ($ZnAl_2O_4$) nanoparticles, crystalline–low quartz and amorphous silica powders were incorporated with Ce^{3+} and Tb^{3+} ions. These powders were successfully synthesized by the solution combustion and sol-gel routes. Phase analysis, particle sizes and morphology of the $ZnAl_2O_4$ nanoparticles were determined with X-ray diffraction (XRD), high resolution transmission electron microscopy (HRTEM) and scanning electron microscopy (SEM). Similarly, both low-quartz and amorphous phases of silica were determined the same way. The photoluminescence (PL) data were collected at room temperature using a variable UV Xenon lamp mounted into the F7000 Fluorescence and Cary Eclipse fluorescence spectrophotometers. The cathodoluminescence (CL) data were collected at room temperature using Ocean Optics CL spectrometer attached to the vaccum chamber of the Physical Electronics PHI 549 Auger electron spectrometer. The surface characterization was carried out using Auger electron spectroscopy (AES) and X-ray photoelectron spectroscopy (XPS).

The average crystallite sizes for zinc aluminate powder phosphors reduced in the hydrogen atmosphere were ranging from 20 nm to 50 nm. The results from XRD and HRTEM showed that $ZnAl_2O_4$:Ce^{3+}, Tb^{3+} powder phosphors were crystalline and the lattice spacing estimated form SAED was 0.24 nm, corresponding to the (311) lattice of $ZnAl_2O_4$. The PL intensity of the green line emission from Tb^{3+} at 544 nm ($^5D_4 \rightarrow {}^7F_5$ transition) increased as a result of Ce^{3+} co-doping. The fact that the increase was simultaneous with the

decrease in blue emission from Ce^{3+} (5d → 4f transition) suggests that excitation energy was transferred from Ce^{3+} to Tb^{3+}.

The AES and CL data were collected simultaneously when the powders were irradiated with a beam of electrons (for 10 hours) in a vacuum chamber maintained at 1×10^{-7} TorrO_2 atmosphere. The AES elemental composition data for the degraded powder phosphors gave all the main elements in the $ZnAl_2O_4$:Ce^{3+}, Tb^{3+}, namely; Zn, Al, O and adventitious C. The ratio of Zn APPH to that of oxygen was almost stable during the electron beam irradiation. The Al/O ratio increased from 0 – 300 C.cm^{-2} and then stabilized while the adventitious C peak decreased drastically from 0 – 600 C.cm^{-2} before stabilizing. The simultaneous increase of the CL intensity with the removal of C between 0 – 600 C.cm^{-2} suggests that the presence of C on the surface inhibited light emission from the surface. The decrease in the C/O APPH ratio was due to removal of C from the surface due to the presence of Al_2O_3 investigated using electron stimulated surface chemical reactions (ESSCRs) model. The CL intensity then decreased slightly after 600 C.cm^{-2} electron dose and then remained stable. According to ESSCR model, electron beam irradiation may dissociate the O-O (from O_2 introduced in the vacuum chamber) and Zn-Al-O bonds resulting in highly reactive O^{2-}, Zn^{2+}, and Al^{3+}. The XPS data collected from the sample of $ZnAl_2O_4$:Ce^{3+}, Tb^{3+} proved that there was structural readjustment from inversion to normal spinel as a result of annealing in reduced H_2 atmosphere.

In a low quartz and amorphous silica samples, efficient energy transfer from Ce^{3+} to Tb^{3+} ions was observed when the powder phosphors were excited at the wavelength of 322 nm. The transfer rate was shown to be more efficient for samples reduced in a mixture of N_2 and H_2 compared to those annealed in air. Thus, the maximum energy transfer was observed from the sample co-doped with SiO_2: 2 mol%Ce^{3+}, 4 mol%Tb^{3+}. The excitation of 322 nm is ascribed to direct excitation of Ce^{3+} ions from 4f → 5d transition of Ce. The

improved down-converted emission indicates that our materials can be used as wavelength shifting layer in Si photovoltaic cells to improve their power conversion efficiency.

KEYWORDS

Combustion, sol-gel, aluminates, silica, cerium, terbium, annealing, energy transfer, X-ray diffraction, Photoluminescence, X-ray photoelectron

AES − Auger electron spectroscopy

CL − Cathodoluminescence

CPU - Central processing unit

D/A - Digital /Analog

EM - Emission

EQE − External quantum efficiency

EX - Excitation

HRTEM − High resolution transmission electron microscopy

OR − Alkoxide

PC - Personal computer

PL − Photoluminescence

RAM - Random access memory

RE − Rare earths

SAED − Selected area electron diffraction

SEM − Scanning electron microscopy

SH1/2 - Super Hitachi1/2

TEOS − Tetraethylorthosilicate

USB - Universal serial bus

UV − Ultraviolet

XPS − X-ray photoelectron spectroscopy

XRD − X- ray diffraction

Table of Contents

LIST OF FIGURES

CHAPTER 1 GENERAL INTRODUCTION;

1.1 Overview

Among the forms of green energiey sources (e.g. hydropower, wind power, geothermal power and biomass) solar power is one of the most sustainable energy due to its abundance and renewability. Using the photovoltaic (PV) effect, sunlight can be converted directly into electricity. However, the classical efficiency limit of silicon-based solar cells is currently estimated to be in the range of 30% from the calculations reported by Shockley and Queisser [1,2]. There are three spectral modification methods in place to be used, namely: downconversion (DC), photoluminescence (PL) and upconversion [3].

Shalav et al. suggested that light with energy lower than the threshold of ~1.25 eV would be suited for upconversion (UC), whereas light with energy higher than the threshold of ~ 1.25 eV would be better suited for downconversion (DC) applications for an ideal semiconductor with a threshold of ~ 1.35 eV [4]. Furthermore, for wavelengths less than 500 nm or more than 1100 nm, the DC and UC can be used to convert high/low energy photon such that is it suitable for the solar cell applications [5].

The possibility of achieving two-photon emission via energy transfer was first predicted by Dexter [6]. Recently, several groups reported downconversion from ultraviolet (UV) or visible (VIS) light to near-infrared (NIR) light using rare-earth ion pairs [7-12]. Vergeer et al. [13] have established experimentally the mechanism for the downconversion in the $Tb^{3+}-Yb^{3+}$ system in these compounds $Yb_xY_{1-x}PO_4:Tb^{3+}$. Now the research of DC is focused mainly on the RE ($Tb^{3+}-Yb^{3+}$) ion pairs [14-15]. However, several issues have not been solved yet: the f-f transition which leads to a narrowband excitation, the very low energy transfer efficiency from Tb^{3+} to Yb^{3+} since the Tb^{3+} ions show weak absorption in the UV/blue region due to the forbidden nature of 4f−4f transitions.

In this study, we focus more on investigating downconversion process on the Ce^{3+} −Tb^{3+} co-dopants in the $ZnAl_2O_4$ and SiO_2 host lattices. One of the advantages for the use of Ce^{3+} ions is the fact that the transition of Ce^{3+}: 4f →5d has relative strong absorption at the wavelengths less than 350 nm, unlike Tb^{3+} ions which show a weak absorption in the UV/blue region. The investigation of the downconversion phenomena is mainly focused on the evaluation of an efficient energy transfer between Ce^{3+} and Tb^{3+} ions. Here, Ce^{3+} ions will be classified as sensitizers by absorbing UV photons and transfer them to Tb^{3+} ions which are classified as activators/absorbers and they will subsequently emit green photons in the visible region of the electromagnetic spectrum. In principle, downconversion concept is particularly based on using a combination of two rare-earths (Ce^{3+} and Tb^{3+}) ions whereby a single absorbed high energy photon produces an emission of two visible photons. Therefore, the downconversion nanophosphors will be studied from $ZnAl_2O_4$: Ce^{3+}, Tb^{3+} and SiO_2: Ce^{3+}, Tb^{3+} nanoparticulate phosphors where $ZnAl_2O_4$ and SiO_2 are host matrices and Ce^{3+} is a dopant, and Tb^{3+} is a co-dopant.

Traditionally, $ZnAl_2O_4$ with normal, intermediate or inverse spinel structure is widely used as a catalyst or ceramic [16]. Today, it is used in many applications such as optoelectronics, sensor technology and information display technology [17-20] because of its excellent optical, hydrophobic properties, high chemical and thermal stability [21]. For application in display technologies, $ZnAl_2O_4$ is used as host matrix for trivalent rare-earth ions (e.g. Tb^{3+}, Eu^{3+} and Dy^{3+}) [22,23] or transition metals (e.g. Mn^{2+} and Cr^{3+}) [24] to prepare phosphors emitting mostly in the visible range of the electromagnetic spectrum.

In this study, we are particularly interested in the performance of a nanocrystalline $ZnAl_2O_4$ because the nanocrystalline materials indeed have better optical properties than their bulk counterparts [25]. It has been shown recently [26,27] that colour tuning in zinc gallate ($ZnGa_2O_4$), another member of zinc-based spinels is highly possible depending on the

synthesis process. Another important feature of this class of material is that the luminescence properties are highly dependent on the atmosphere of synthesis [27]. As a result, colour tuning in $ZnGa_2O_4$ may be achieved by heat treatment under reducing or oxidizing atmosphere. Since some optical properties of $ZnGa_2O_4$ resemble those of $ZnAl_2O_4$, colour tuning in the latter might also be possible, opening up a broader range of applications for this phosphor.

In the case of SiO_2, we focus on downconversion process on the Ce^{3+} −Tb^{3+} in both amorphous and crystallized forms. Taking into account that SiO_2 can exist in an amorphous or crystalline form, it has stimulated the interest to be investigated both experimentally and theoretically. In this study our objective was to investigate the performance for the efficient energy transfer from Ce^{3+} to Tb^{3+} in low quartz and the amorphous phases of SiO_2. SiO_2 has proved to be a good host matrix for rare-earth dopant ions because of its transparency, compositional variety and ease of production [28].

Different synthesis methods such as sol-gel [29,30], hydrothermal [31], combustion [25], [20], [32] and solid state reaction [33] are commonly used to prepare rare-earths/transition metals doped nanocrystalline $ZnAl_2O_4$ phosphors. Amongst the synthesis techniques used to prepare $ZnAl_2O_4$ phosphor, the solution combustion compared to other methods has advantages such as cost-effectiveness, low processing temperature, extremely shorter reaction time, high purity and homogeneity of the final product. On the other hand, SiO_2 is commonly prepared by the sol gel process. The sol-gel derived SiO_2 offers advantages such as cost-effectiveness, production of materials with low density, and low co-efficient of thermal expansion [28]. The current research on $ZnAl_2O_4$:Ce^{3+}, Tb^{3+} and SiO_2:Ce^{3+}, Tb^{3+} include the study of the combustion and sol-gel syntheses, luminescent

properties (photoluminescence –PL), structural analysis (X-ray diffraction-XRD and high-resolution transmission electron microscopy-HRTEM), absorbance and diffused reflectance cathodoluminescence (CL), decay characteristics and electronic states (X-ray photoelectron spectroscopy –XPS).

1.2 Statement of the problem

To lower the cost of harvesting high energy photons from the solar spectrum or how to enhance the efficiency of photovoltaic cells has been a challenge for several decades. On that note, the application of the luminescent down-conversion nano-materials has been proposed as a method for improving the poor spectral response (SR) of solar cells typically the silicon (Si) to the exposure of short-wavelength light. This poor spectral response is due to thermalisation of minority carriers generated by photons with energy higher than twice the band gap of Si (E>2.24 eV) [3]. Therefore, the approach of photon conversion is basically different from the other third generation concepts discussed in detail by Werner [34]. The introduction of luminenscent down-conversion layer speculates the new design of the PV device which will create the first encounter with additional interactions of the light resulting in extra loss mechanisms which contribute to poor performance of a solar cell. Basically, the down-conversion processes aim at converting via luminescence the solar spectrum to match the absorption properties of the PV device.

The materials which can be used as luminescence down-converters must satisfy specific requirements in order to maximize the benefits from its application. Therefore, the host material must exhibit high transmittance, particularly in the region where the cell's response is high, as well as low scattering light. In addition, the host needs to provide an optimum environment for the dissolvement of the luminescent centers. On the other hand,

luminescent centers used should ideally exhibit good separation between the absorption and emission bands in order to minimize losses due to re-absorption.

Intensive laboratory research investigations need to be carried out to understand the use of $ZnAl_2O_4$ as best host candidate, whereas Ce^{3+} and Tb^{3+} also need to be investigated as potential luminescent centers for downconversion through energy transfer processes. There are quite a few results reported already in the current study for nanocrystals $ZnAl_2O_4$:Ce^{3+}, Tb^{3+} as luminescent material for down-conversion studies, unlike as a catalyst. Thus, the development of this material could make a huge impact on solar energy technology.

Several researchers have discovered one of the best features for enhancing the luminescence intensities of the luminescent material and that is called the study of an energy transfer between the host and the dopant ions or via dopant ions only in a given matrix. Hence the study of energy transfer between a pair of non-identical trivalent rare-earth ions such as Ce^{3+} and Tb^{3+} has really been a subject of intensive research lately. However, the energy transfer efficiency has not yet been perfected. As a result, more development in getting optimum concentrations from rare earth activated phosphors is still required. The optical properties of the luminescent materials doped and co-doped with different concentrations of the rare earth ions were investigated.

1.3 Research Objectives

- To synthesize $ZnAl_2O_4$:Ce^{3+}, Tb^{3+} and SiO_2:Ce^{3+}, Tb^{3+} powder phosphors using solution combustion.

- To investigate the structural and morphological properties of the $ZnAl_2O_4$:Ce^{3+}, Tb^{3+} and SiO_2:Ce^{3+},Tb^{3+} powder phosphors.

- To study the photoluminescence properties of the $ZnAl_2O_4:Ce^{3+}$, Tb^{3+} and $SiO_2:Ce^{3+}$, Tb^{3+} powder phosphors.

- To investigate cathodoluminescence degradation of $ZnAl_2O_4:Ce^{3+}$, Tb^{3+} powder phosphor.

- To investigate the chemical and electronic states of the elements present in $ZnAl_2O_4:Ce^{3+}$, Tb^{3+} and $SiO_2:Ce^{3+}$, Tb^{3+} powder phosphors.

- To investigate energy transfer efficiency from Ce^{3+} to Tb^{3+} into $ZnAl_2O_4$ and SiO_2 matrices

1.4 Thesis Outline

Chapter 2 provides a theoretical background on luminescence processes such as; photoluminescence, cathodoluminescence, and downconversion processes mainly for the application in the field of photovoltaic technology. Brief background on the rare earth ions, namely Ce^{3+} and Tb^{3+} is highlighted. A detailed information on the structural analysis of both $ZnAl_2O_4$ and SiO_2 matrices is presented. Finally, brief information on the energy transfer in rare earth co-activated phosphors is provided.

Chapter 3 presents a brief description of the research techniques used in this study.

Chapter 4 presents synthesis, structure and UV-Vis properties of $ZnAl_2O_4$ and SiO_2 host lattices.

Chapter 5 mainly discusses the luminescence properties and X-ray photoelectron spectroscopy study of $ZnAl_2O_4:Ce^{3+}$, Tb^{3+} phosphor.

In **Chapter 6** the luminescence properties of Ce^{3+} and Tb^{3+} co-activated $ZnAl_2O_4$ phosphor are discussed.

Enhanced green emission from UV-down-converting Ce^{3+} - Tb^{3+} co-activated $ZnAl_2O_4$ phosphor is presented in **Chapter 7**. The structure, photoluminescence properties and XPS studies of low quartz SiO_2 host are presented in **Chapter 8**.

In **Chapter 9** the energy transfer from Ce^{3+} to Tb^{3+} in amorphous silica host is discussed.

Finally, in **Chapter 10** the summary of the thesis and suggestions for future work are presented. The list of publications resulting from this current research and the conferences presentations are also presented.

1.5 References

[1] W. Shockley and H. Queisser, J Appl Phys. 32−3 (1961) 510.

[2] T. Trupke, M. Green, P. Würfel, *J. Appl. Phys*. **92** (2002) 1668.

[3] T. Trupke, M. Green, P. Würfel, *J. Appl. Phys*. **92** (2002) 4117.

[4] A Shalav, B. S Richards, M.A Green, *Sol. Energy Mater. Sol. Cells*, **91**, (2007) 829.

[5] Q.Y Zhang, X.Y Huang, *Prog.Mater. Sci*, **55**, (2010) 353.

[6] C. Strümpel M. McCann, G. Beaucarne, V. Arkhipov, A. Slaoui, V. Švrček, C. del Canizo and I. Tobias., *Sol. Energy Mater. Sol. Cells* **91** (2007) 238.

[7] D. Dexter, *Phys. Rev*. **108** (1957) 630.

[8] Q. Zhang, G. Yang, Z. Jiang, *Appl. Phys. Lett*. **91** (2007) 051903.

[9] J. Ueda, S. Tanabe, *J. Appl. Phys*. **106** (2009) 043101.

[10] S. Ye, B. Zhu, J. Chen, J. Luo, G. Lakshminarayana, J. Qiu, *Opt. Express* **16** (2008) 8989.

[11] D. Chen, Y. Wang, Y. Yu, P. Huang, F. Weng, *Opt. Lett*. **33** (2008) 1884.

[12] B. Ende, L. Aarts, A. Meijerink, *Adv. Mater*. **21** (2009) 1.

[13] P. Vergeer, T. Vlugt, M. Kox, M. Hertog, J. Eerden, A. Meijerink, *Phys. Rev*. **B 71** (2005) 014119.

[14] S. Ye, B. Zhu, J. Chen, J. Luo, J. Qiu, *Appl. Phys. Lett*. **92** (2008) 141112.

[15] Q. Zhang, C. Yang, Y. Pan, *Appl. Phys. Lett*. **90** (2007) 021107.

[16] X. Duan, D. Yuan, X. Wang, H. Xu, *J. Sol–Gel Sci. Technol*. **35** (2005) 221–224.

[17] Z. Lou, J. Hao, *Appl. Phys*. **A 80** (2005) 151–154.

[18] S. Mathur, M. Veith, M. Haas, H. Shen, N. Lecerf, V. Huch, S. Hufner, R. Haberkon,H.P. Beck, M. Jilavi, *J. Am. Ceram. Soc*. **84 (9)** (2001) 1921–1928.

[19] X. Wang, M. Zhang, H. Ding, H. Li, Z. Sun, *J. Alloys Compd*. **509** (2011) 6317–6320.

[20] F. Davar, M. Salvati-Niasari, *J. Alloys Compd*. **509** (2011) 2481–2492.

[21] M. Zawadzki, J. Wrzdyszcz, W. Strek, D. Hreniak, *J. Alloys Compd*. **332–324** (2001) 279–282.

[22] B.S. Barros, P.S. Mellow, R.H.G.A. Kiminami, A.C.F.M. Costa, G.F. de Sa, S. Alves Jr., *J. Mater. Sci*. **41** (2006) 4744 – 4748.

[23] I. Mindru, G. Marinescu, D. Gingasu, L. Patron, L. Diamandescu, C. Ghica, B. Mironov, *Mater. Sci. Eng*. **B 170** (2010) 99–106.

[24] S.S. Pitale, V. Kumar, I.M. Nagpure, O.M. Ntwaeaborwa, H.C. Swart, *Appl. Surf.Sci.* **257** (2011) 3298–3306.

[25] R.N. Bhargava, D. Gallagher, X. Hong and A. Nurmikko, Phys. Rev. Lett. 72 (1994) 416.

[26] J.S. Kim, H.I. Kang, W.N. Kim, J.I. Kim, J.C. Choi, H.L. Park, G.C. Kim, T.W Kim, Y.H. Hw ang, S.I. Mho, M.C. Jung, and M. Han, *Appl. Phys. Lett*. **82,** (2003) 2029.

[27] J.S. Kim, H.L. P ark, C.M. Chon, H.S. Moon, and T.W . Kim, *Solid State Commun*. **129**, (2004) 163.

[28] O.M. Ntwaeaborwa, H.C. Swart, R.E. Kroon, P.H. Holloway and J.R. Botha, *Surf. Interface, Anal*. **38,** (2006) 458 -461

[29] Y. Wu, J. Du, K.-L. Choy, L.L. Hench, J. Guo, *Thin Solid Films* **472** (1–2) (2005) 150–156.

[30] M.-T. Tsai, Y.-X. Chen, P.-J. Tsai, Y.-K. Wang, *Thin Solid Films* **518 (24)** (2010) e9–e11.

[31] C.-C. Yang, S.-Y. Chen, S.-Y. Cheng, *Powder Technol*. **148 (1)** (2004) 3–6.

[32] V. Singh, V. Natarajan, J.-J. Zhu, *Opt. Mater*. **29** (2007) 1447–1451.

[33] N.J. van der Laag, M.D. Snel, P.C.M.M. Magusin, G. de With, *J. Eur. Ceram. Soc*. **24 (8)** (2004) 2417–2424.

[34] J. Werner, *Adv. Solid State Phys*. **44** (2004) 51.

[35] K.G. Tshabalala, S.-H. Cho, J.-K. Park , Shreyas S. Pitale, I.M. Nagpure, R.E. Kroon, H.C. Swart ,O.M. Ntwaeaborwa, *J. Alloys. Compd*. **509** (**41**) (2011) 10115−10120.

[36] K. G. Tshabalala, I. M. Nagpure, H. C. Swart, O. M. Ntwaeaborwa, S.-H. Cho, and J.-K. Park, *J. Vac. Sci Technol*. **B 30**(**3**) (2012) 03141.1−031401.6

[37] K.G. Tshabalala, S.-H. Cho , J.-K. Park, Shreyas S. Pitale, I.M. Nagpure, R.E. Kroon, H.C. Swart ,O.M. Ntwaeaborwa, Phys. B: Condens. Matter. **407** (2012) 1489−1492

CHAPTER 2 THEORETICAL BACKGROUND

2.1 Luminescence

The thermodynamic equilibrium prevailing in a system may be disturbed by an external agent such as a beam of radiation from an external source. On that note, the system turns to undergo a transition to an excited state and as a result of processes developed within it, tends to restore their original state. It is noted that luminescence is one such process. Luminescence can primarily be classified into two principal processes namely: fluorescence and phosphorescence which can be distinguished by the delay in reaction to external electromagnetic radiation. Fluorescence is a type of luminescence whereby a substance absorbs radiation and almost instantly begins to re-emit the radiation. Thus, it comes to an end almost as quickly as it begins. Usually, the wavelength of the re-emitted radiation is longer than the wavelength of the radiation the substance absorbed [1]. In contrast to the nearly instantaneous "on-off" of fluorescence, phosphorescence involves a delayed emission of radiation following absorption. The delay may take as much as several minutes and phosphorescence continues to appear after the energy source has been removed.

Primarily, luminescent materials known as phosphors are mostly solid inorganic materials consisting of a host lattice, usually intentionally doped with luminescent centers (transition metals or rare-earths [2-4]. The dopant concentrations are in most cases very low in view of the fact that at higher concentrations, the efficiency of the luminescence process is usually reduced. This is known as concentration quenching effect mainly ascribed to the migration of excitation energy to the traps due to the increased delocalization of the excitation or to the cross relaxation (exchange interaction) between luminescent centers [5]. Furthermore, the absorption of energy, which is normally used to excite the luminescent material, usually takes place by either the host lattice or by intentionally doped impurities. In most cases, the impurity ions normally called activator ions are the ones responsible for

generating the desired emission. When the activator ions show relatively a weak absorption, another kind of impurities can be co-doped (added) and these impurities are classified as sensitizers, which absorb the energy and subsequently transfer their energy to the activator ions and result in the emission of the visible light [6].

2.1.1 Charge Transfer Luminescence

The optical transition in case of charge transfer normally takes place between different kinds of orbitals or between electronic states of different ions. Quite frequently, the change of the charge distribution on the optical center is observed mainly due to an excitation. Finally, the chemical bonding also changes. As a result, one can observe very broad emission spectra. The $CaWO_4$ [7] compound is a well known example used for decades for the detection of X-rays which shows luminescence emanating from the $(WO_4)^{2-}$ group as shown in (Fig 2.1) below.

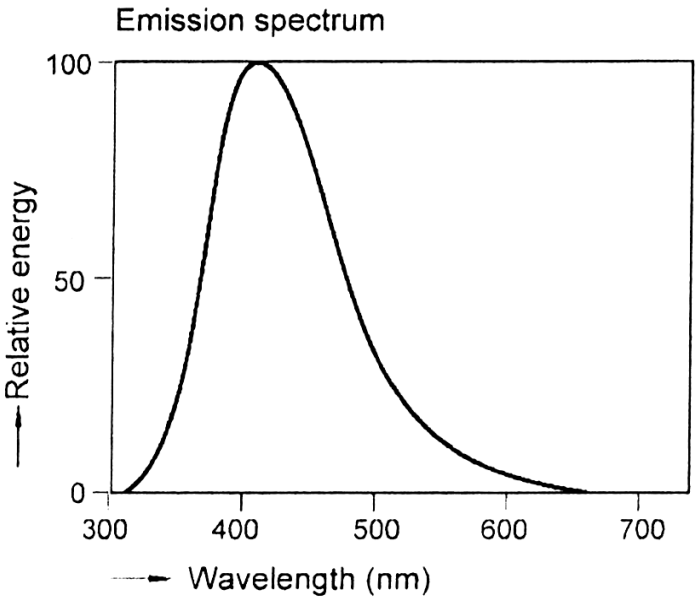

Figure 2-1 Emission Spectrum of CaWO4 [7]

2.1.2 Excitation and quenching of luminescence

Photoluminescence arises due to excitation by primary radiation (photons), whereas cathodoluminescence is produced through excitation by a beam of electrons. Furthermore, the excitation of luminescence may be associated with the effect of a beam of heavy ions, neutral particles, or various mechanical, electrical and magnetic phenomena. In cases where the system is found to be in a non-equilibrium state due to a chemical reaction, the light emission process is referred to as chemi-luminescence [8]. On the other hand, any penetration of an electric field into a phosphor may give rise to electroluminescence [9].

The magnitude of the external effect is mainly and directly related to the intensity of the luminescence. For instance, in the case of excitation by radiation, it depends on the magnitude of the luminous flux. Also, it can depend on the degree of interaction between the system and incident radiation. If the radiation is poorly absorbed, the resulting luminescence becomes weak.

However, the quenching (suppressing) of luminescence essentially involves the restoration of the equilibrium distributions of the activator ions over the energy levels. Thus, the disappearance of luminescence may be associated with an increase in the probability of photochemical disintegration of the ions on collision. In addition, an increase in the concentration of molecules frequently leads to associations and reduction in the number of luminescing ions [5].

2.1.3 Optical excitation of Luminescence and Energy Transfer

The optical excitation of luminescence is mainly viewed as an absorption of UV or even visible light which can lead to emission. Furthermore, optical absorption can take place on the already discussed impurities (optical centers), being either the activator ions or the sensitizer ions. Sensitizer ions as described in previous sections are used when the optical

absorption of the activator ions is too weak as a result of a forbidden optical transition so as to be used in practical devices. In such cases, energy transfer from the sensitizer ions to the activators has to take place. Moreover, energy transfer from host lattice states to the activator ions also has to take place.

2.1.4 Luminescence Lifetimes

The strength of optical transitions is manifested using two distinct properties, namely: the absorption and the emission of luminescent materials. The luminescence lifetime is defined as the rate of spontaneous emission and is set to be proportional to the square of the transition dipole moment [7]. Apparently, the luminescence lifetime has been determined experimentally in two ways [11]. First one is a sinusoidal modulation of the excitation intensity and measuring the time dependent response of the luminescent materials. Second experiment is the use of a pulsed excitation source and measuring a histogram of photon arrival times. Nevertheless, histogram method is regarded as the most popular way to measure the rate of spontaneous emission among the enormous availability of pulsed sources. In the histogram there is a special line connecting points and that line is known as a decay curve.

2.2 Cathodoluminescence

The phenomenon of the emission peak (i.e. the color) of light produced from the specimens as a result of interaction with an electron beam is called cathodoluminescence (CL). The origin of this special kind of luminescence arises due to the presence of impurity atoms, (transition metals or rare earths) in the crystal lattice. At the same time, using cathodoluminescence optical spectrometer attached to one of the ports of an Auger electron spectrometer shown in Figure 2.2 below the CL properties of the samples were measured. The samples were irradiated with a beam of high energy electron resulting in the emission of

light following the creation and subsequent recombination of electron hole pairs. The emitted light was captured by optical fibre attached to one of the ports of the chamber of the AES. Finally, the CL spectrum was displayed on the computer screen that was connected to the optical fibre.

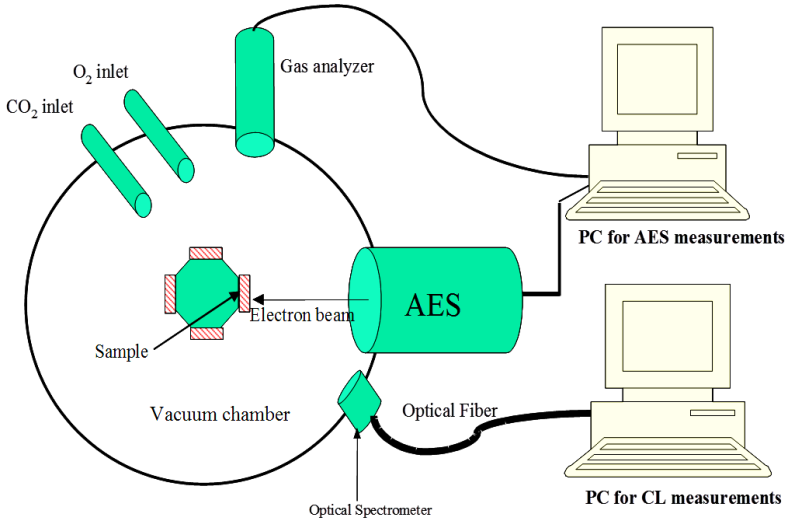

Figure 2-2 Schematic diagram of the PHI 549 Auger system [11]

The mechanisms for CL are similar to those for photoluminescence, but the external radiation or excitation source is that of an electron beam rather than a visible or ultraviolet light beam like in the case of the latter process. When an energetic (keV range) electron beam propagates within a semiconductor or insulator, the primary electrons lose energy by creation of electron-hole pairs. These electron-hole pairs then eventually diffuse through the luminescent material and transfer their energy to luminescent centers responsible for the output of the luminescent emission of visible photons [12-13]. As a result, a new recombination via radiative and non-radiative processes takes place. In this case, only the radiative recombination process responsible for creation of a photon is mainly viewed as CL through the optical fiber connected to the computer interface as shown in figure 2.2.

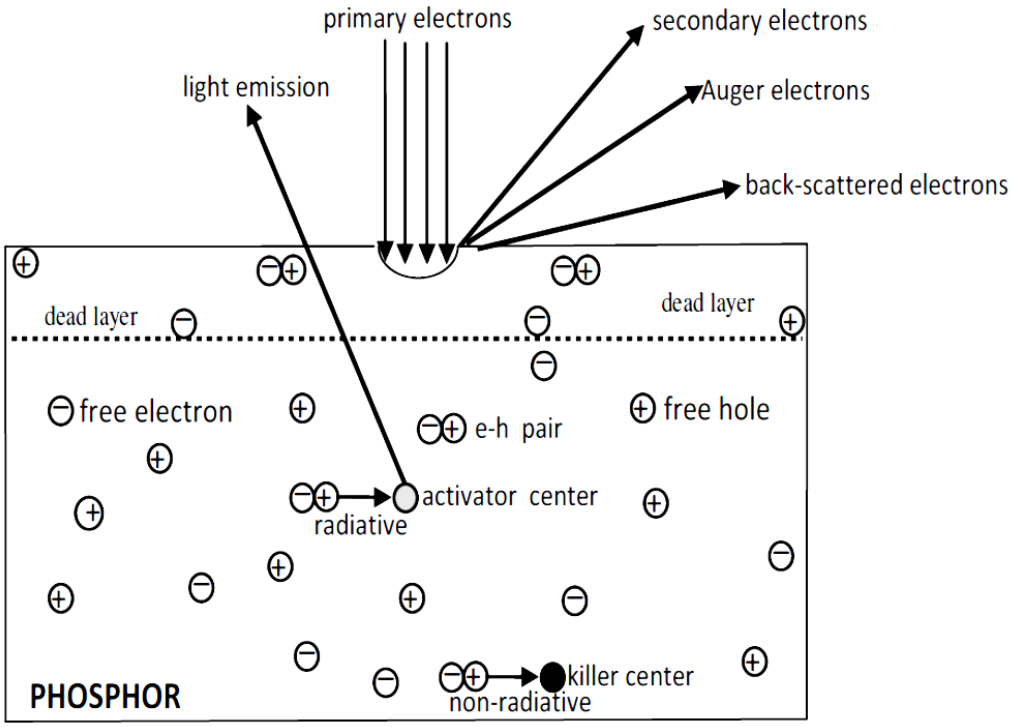

Figure 2-3 CL process in a phosphor grain [11]

Figure 2.3 shows an illustration of the free electrons and holes which may be coupled to produce electron-hole (e-h) pairs. As a result, the radiative recombination which leads to the generation of a photon (quantized light) is mainly taking place due to the diffusion process of e-h pairs through the luminescent material and subsequently, enables a light emission from activator ions by the energy transfer process [11]. In contrast, the e-h pair diffusion can also take place through the surface of the phosphor. It eventually result in a non-radiative recombination which will then form a thin dead (inactive luminescent) layer on the surface whose formation is explained in terms of the well documented electron stimulated surface chemical reaction model (ESSCR). The dead layer is known to cause reduction of the CL intensity.

2.3 Down-conversion

The luminescent properties of the trivalent rare-earth ions (REs^{3+}) are unique and fascinating because of abundant energy levels of 4f electron configurations. Taking into

consideration the behavior of these REs ions based nano-materials, there is great interest for a wide range of applications such as lighting, display materials, and efficiency enhancement for silicon solar cell devices. On that note, one should understand that the application depends solely on the corresponding luminescent behavior. Hence this requires a deep knowledge and understanding of the luminescent mechanism for new aspects in the field and any new design of REs^{3+} based luminescent materials. So, the use of REs ions to convert photons to different and more useful wavelengths is well-known from different applications (e.g. lasers, white LEDs). Based on that, a new ideal application has emerged: the boost on the conversion of the solar spectrum for energy efficiency enhancement in solar cells using REs ions. This idea is motivated by the fact that there is a spectral mismatch which can account for over 60% of the energy losses in a solar cell [14]. The thermalisation of charge carriers generated by the absorption of high-energy photons is one of the major loss mechanisms [15]. One way to alleviate this loss is by means of spectral conversion. In the last few years there has been a renewed interest in different methods to break the Shockley-Queisser limit [16] to the energy conversion efficiency of single-junction solar cells [17-18]. One of the keys to the development of a single-junction cell with conversion efficiency greater than the Shockley-Queisser limit is to split high energy photons into multiple photons each of which has energy greater than the threshold of the semiconductor material *Eg* (Down-conversion) [19]. The work on down-conversion is limited in comparison to up-conversion studies [20]. In this case the down-conversion process is mainly dealt with separately from the photovoltaic process and consequently, does not interfere with photogenerated carrier collection [18]. Therefore, the main objective of this current research is primarily to study down-conversion processes in nanoparticulate phosphors coupled with REs ions. In fact, we want to stress a point that down-shifting is different from down-conversion. Down-shifting can be defined as a process in which a single photon is absorbed at a short wavelength followed by emission of

a single photon at a longer wavelength [21]. As a result, it cannot break the Shockley-Queisser limit because detailed balance does not change. Furthermore, it has also been shown that silicon nanocrystals (Si-NC) embedded in SiO_2 matrix act as down-shifting layers and can enhance the overall system efficiency for high performing down-shifting layers [22].

On the other hand, down-conversion is a similar optical process where one high-energy photon is absorbed and converted into two lower-energy photons typically achieved by coupling REs ions to a phosphor material where energy transfer can occur [23]. Therefore, down-conversion changes detailed balance. Recently, down-conversion has been considered for increasing the conversion efficiency of Si-based solar cells and it has also been realized with Tb^{3+} $-Yb^{3+}$, Pr^{3+} $-Yb^{3+}$, Eu^{3+} $-Yb^{3+}$, Ce^{3+} $-Yb^{3+}$, and Ho^{3+} $-Yb^{3+}$ couples to down convert visible emission lines into near-infrared (NIR) emission lines [24-28]. Finally, in this work, we have focused more on the $Ce^{3+} - Tb^{3+}$ couple in the compounds $ZnAl_2O_4$ and SiO_2.

The spectrum modification: to lower energies by down-conversion mechanism as shown in Figure 2.4 is performed via host lattice states and result in incident photons with excitation energy $E_{exc} > 2E_g$ to generate e−h pairs, each with energy $\approx E_g$. This is known as an interband Auger effect [29], where the electron is excited from the valence band (VB) to energy far into the conduction band (CB), and another electron gets excited over the bandgap through the absorption of an excess energy. Consequently, one exciting photon generates two e−h pairs as shown in Figure 2.4. Later on, the e−h pairs recombine on the luminescent centers, yielding two emitted photons for every photon absorbed. Finally, this process of emission of two photons of visible light by energy transfer is the opposite of the well-known 'Addition de Photons par Transfert d'Energie (APTE, discovered by Auzel in 1966 [30], which is nowadays known as upconversion.

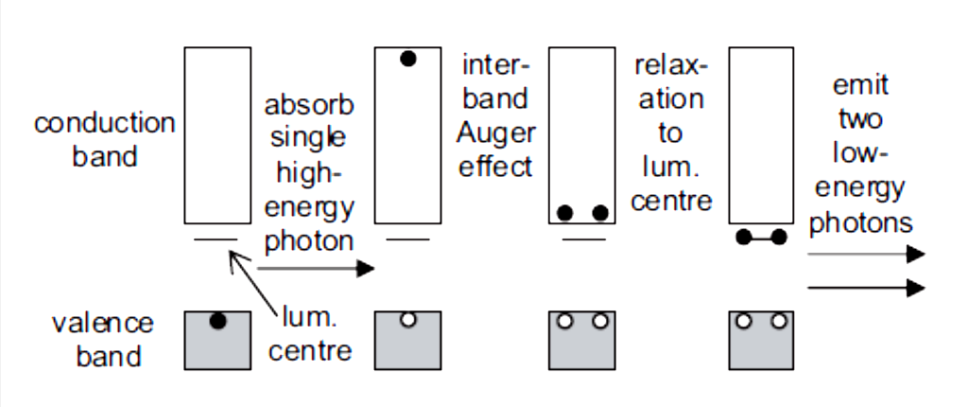

Figure 2-4 Interband Auger mechanism for the generation of two low -energy photons from each high-energy incident photon within a solid-state material doped with luminescent centers [31]

Figure 2.5 shows both down-conversion and up-conversion device fabrication. Down-coversion has so far only been observed in vacuum ultraviolet ranges; hence it is mainly being placed on the front side of the bifacial solar cell to split one high energy photon into two low energy photons. Furthermore, an up-converter is placed on the rear side of the bifacial solar cell to convert two (or more) transmitted low energy photons to one high energy photon able to generate e−h pair when re-injected into the cell.

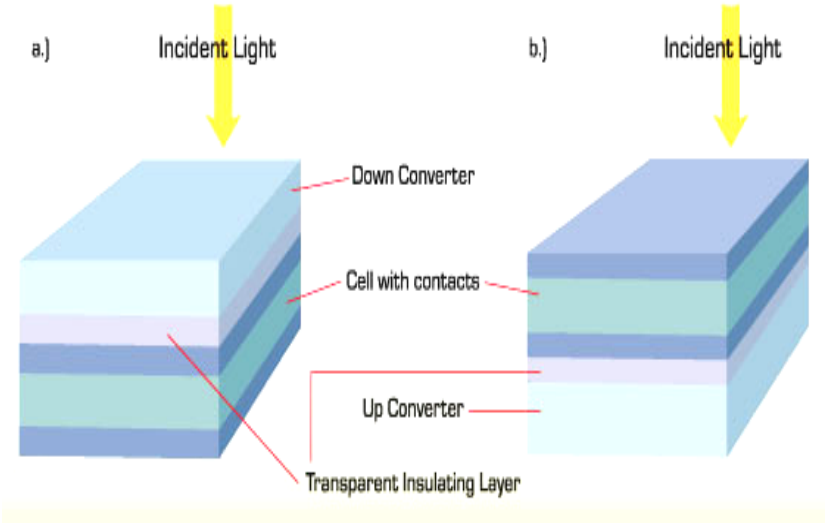

Figure 2-5 Spectrum modification: a) to lower energies by down-conversion and b) to higher energies using up-conversion [32]

2.4 Rare-earths (REs)

The term "rare earth" (RE) or sometimes called "lanthanides" refers to the elements in the periodic table ranging from lanthanum (^{57}La) up to lutetium (^{71}Lu). Yttrium (^{39}Y) and scandium (^{21}Sc) are included in this group because their chemical behavior is very similar to that of the lanthanide group. The electronic structure of the RE atoms can be described in terms of a core of filled shells equivalent to the xenon (Xe) atom, and the following configuration: $4f^n5d^{0-1}6s^2$. This gives a complete configuration as follows: $[Xe]^{54}$ $4f^n5s^25p^65d^{0-1}6s^2$ (n = 1, 2, ... , 14). Furthermore, after $5s^25p^65d^{0-1}6s^2$ orbitals have been filled, the 4f shell will be filled gradually from n = 0 to 14 electrons. The 4f electrons of RE elements are well shielded by the full $5s^25p^6$ sub-shells and are deep-seated near the nucleus because they are "localized" and have lower energies. At cerium (Ce), there is one 4f electron and the number of 4f electrons increases steadily through the group, until there is 13 ($4f^{13}$) at Ytterbium and the filled shell $4f^{14}$ at Lutetium.

A characteristic feature of the rare earths (REs) is the regular decrease in the atomic volume or 'radius' when moving from lanthanum (La) to lutetium (Lu). Most of these elements crystallize in a hexagonal closed-packed structure except for Ce, Eu and Yb, which have a cubic structure [33]. This is known as the lanthanide contraction. The $5d^16s^2$ valence electrons form the conduction bands in the solid state. As a result, the RE ions are usually trivalent both in their atomic state and in the solid state. An exception occurs for the following RE candidates, that is, Ce, Eu and Yb in the solid state. On that note, Ce can exist as trivalent Ce^{3+} or tetravalent Ce^{4+} and Tb element can also exist as trivalent Tb^{3+} or tetravalent Tb^{4+}. Both the trivalent state of Ce and Tb are optically active while the tetravalent state of Ce and Tb respectively are optically inactive.

Rare-earth doped luminescent materials are extensively used in the lighting industry [34-36] as well as plasma display panel (PDP) technologies [36-38]. Below, table 1 shows a list of the rare-earth elements and their electronic configurations.

Table 2-1 The rare-earth elements, their most common oxidation states, and the electronic configuration of the oxidation states [39]

Element	Oxidation states	Electronic configuration 2^+	3^+	4^+
La	3		$4f^0$	
Ce	3, 4		$4f^1$	$4f^0$
Pr	3, 4		$4f^2$	$4f^1$
Nd	3		$4f^3$	
Pm	3		$4f^4$	
Sm	2, 3	$4f^6$	$4f^5$	
Eu	2, 3	$4f^7$	$4f^6$	
Gd	3		$4f^7$	
Tb	3, 4		$4f^8$	$4f^7$
Dy	3		$4f^9$	
Ho	3		$4f^{10}$	
Er	3		$4f^{11}$	
Tm	2, 3	$4f^{13}$	$4f^{12}$	
Yb	2, 3	$4f^{14}$	$4f^{13}$	
Lu	3		$4f^{14}$	

Lanthanide ions with luminescent properties are readily incorporated in host materials as the f-electrons constituting the photoactive center are well shielded [40-42].

2.5 AB_2O_4 Oxide spinels

Zinc aluminate-($ZnAl_2O_4$) spinel, a mixed oxide of aluminium and zinc, is a naturally available mineral commonly called *gahnite* that has the crystal structure belonging to spinel group. The rare mineral (gahnite) was first described in 1807 for an occurrence in the Falu mine, near Falun (Sweden) and originally called *automolite*, but later named after the Swedish chemist, J.G. Gahn (1745−1818), the discoverer of the element manganese [43]. A typical oxide of this type has a cubic structure in which the oxygen ions are in an FCC close-packing array, with the cations in various arrangements in the interstices. Experimentally, the

band gaps in $ZnAl_2O_4$ and $ZnGa_2O_4$ are reported to be about 3.8−3.9 and 4.1−4.3 eV respectively [44].

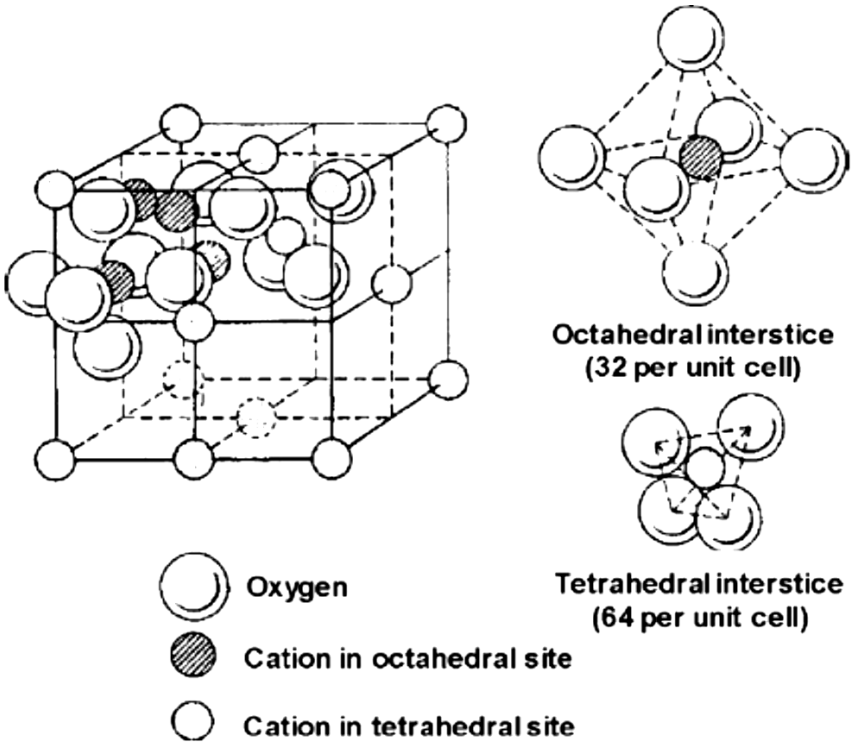

Figure 2-6 Cubic crystalline structure of spinel [45]

Figure 2.6 illustrates the basic structure of a spinel in which the complete unit cell is built by a cubic dense packing of oxygen anions, where half of the octahedral voids are occupied by aluminium cations, and every eighth tetrahedral void is occupied by zinc cations. The complete unit cell will contain 32 oxygen ions, 16 octahedral site cations, and 8 tetraheral site cations, yielding a high degree of complexity.

In the normal spinel structure with the chemical formula AB_2O_4, where A represents a divalent metal ion such as zinc, iron, mangnesium, and/or nickel, and B represents trivalent metal ions such as aluminium, chromium or manganese; the divalent A cations occupy 8 tetrahedral interstices and the trivalent B cations occupy 16 octahedral intersties. This kind of the distribution of cations is not thermodynamically favourable to be most stable, since the configurational degree of disorder counteracts the site preferential energy. As a result, A and

B cations interchange interstices via diffusion, eventually leading to a situation where all the A cations are in octahedral interstices. The latter situation is termed as spinel inversion.

Zinc aluminate is a widely used catalyst employed in chemical reactions, namely: synthesis of methanol and synthesis of styrenes from acetophenones [46-47]. Recently, the optical properties of zinc aluminate have been investigated and it was reported that polycrystalline zinc aluminate has an optical band gap nearly equal to 320 nm and is highly reflective at wavelengths less than 300 nm [48-49]. Researchers in this study focused their interest in the performance of nanocrystalline $ZnAl_2O_4$ because of the better response displayed by nanocrystalline materials through their optical properties than their bulk counterparts [50].

2.6 Silica (SiO_2)

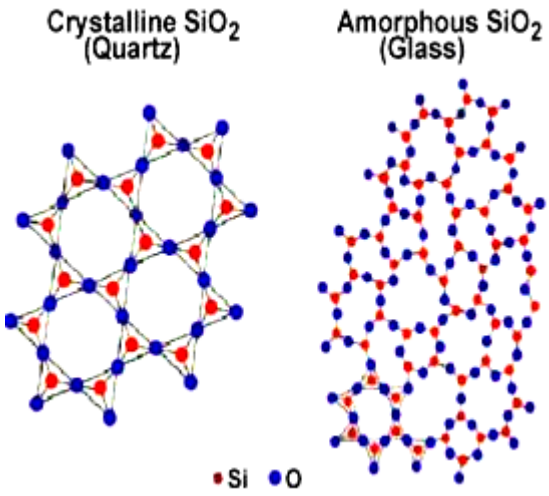

Figure 2-7 SiO_2 having both an ordered crystalline structure (Quartz, left) and a disordered amorphous structure (glass, right) [51]

Silica is widely used in many fields such as medium layer and silicon-based photoelectron material for its excellent chemical stability, thermal stability as well as interfacial combination with silicon semiconductor. Taking into consideration that it can exist as an amorphous or crystalline form as shown in figure 2.7, it has stimulated interest to

be investigated both experimentally and theoretically. Furthermore, based on the physical performance, it has been investigated as a suitable candidate for various applications, viz. surface coating, magnetic materials and gas sensor materials [52-53]. As a glass, it is homogeneous and transparent; hence it can be mixed at higher concentration of doped luminescent ions [54]. The rare earth or transition metal ions [55-58] are often used as activator ions to enhance the luminescent properties of silica for their unique electronic structures. For example, Tb^{3+} ions due to their extensive use as materials for fabricating various optical re-radiators and cathodoluminescent screens when incorporated into glasses, have developed great interest for many researchers [59-60]. However, the problem of enhancing the light output of Tb^{3+} - containing glasses upon UV excitation still remains unresolved. The reason is that the light output of these materials is limited by the occurrence of intense absorption bands in the high-frequency range due to $4f^8 \rightarrow 4f^7(^8S_{7/2})5d^1(T_2)$ and $4f^7(^8S_{7/2})5d^1(E)$ inter-configurational transitions [61] and a relatively low efficiency of excitation transfer from the luminescence sensitizers. In this study, SiO_2 was co-doped with Ce^{3+} and Tb^{3+} in both the amorphous and crystalline forms and energy transfer via a down conversion process between Ce^{3+} and Tb^{3+} was investigated and compared for in the two forms.

2.7 Energy Transfer in rare-earth co-activated phosphors

The energy transfer process in inorganic materials has been the subject of interest for many years and continues to be one focused area of fruitful research. A good understanding of the processes on how the transfer of energy can be affected is very important both fundamentally and technologically. On the fundamental side, transport phenomena are regarded as a niche area for the transfer of optical energy and it is essential to have an understanding of the mechanisms to be used to describe excitation transport, for example,

amorphous materials. On the other hand, on the technical side, there is never-ending demand for new developments of efficient phosphors which are used in solid state lighting.

In the late 1940s Förster [62] developed a basic theoretical framework on the study of energy transfer and afterwards, Dexter was able to describe the process of sensitized luminescence [6,63] by exchange interaction (spectral overlap). The exchange mechanism on the donor luminescence was theoretically interpreted in the study conducted by Inokuti and Hirayama in 1965 [64].

Energy transfer can occur between a pair of identical luminescent centers or between two non-identical centers. Energy transfer refers to a luminescence center (Donor) which is primarily excited by the incident light and subsequently transfers the excitation energy to another luminescence center (Acceptor). The process of energy transfer between the donor and the acceptor separated by a distance R_{SA} between the sensitizer (donor) ion and the activator (acceptor) ion in the host is shown below in figure 2.8.

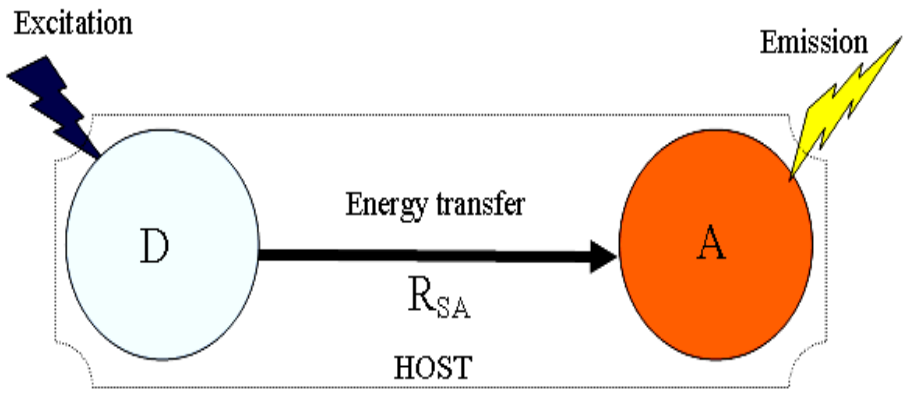

Figure 2-8 Schematic diagram of the energy transfer process. D is Donor, A is Acceptor and R_{SA} is a distance between the sensitizer ion and the activator ion

Energy transfer between two rare-earth ions can be achieved either radiatively or nonradiatively. The condition for resonant nonradiative energy transfer is that both the donor and acceptor are in resonance (e.g. wavefunction overlap), that is, the energy difference between their ground state and excited state should be equal [65].

2.8 References

[1] N. Schlager *Science of Everyday things Vol.2 Real life Physics.*

[2] B.S. Barros, P.S. Mellow, R.H.G.A. Kiminami, A.C.F.M. Costa, G.F. de Sa, S. Alves Jr., *J. Mater. Sci.* **41** (2006) 4744–4748. 23

[3] I. Mindru, G. Marinescu, D. Gingasu, L. Patron, L. Diamandescu, C. Ghica, B.Mironov, *Mater. Sci. Eng*. **B 170** (2010) 99–106. 24

[4] H.H. Le, T.L. Phung, N.L. Nguyen, T.L. Trinh, *J. Phys: Conf. Ser*. **187** (2009) 012053 (1–6).and 24 chap1

[5] D.L. Dexter and J.H. Schulman, *J. Chem. Phys*, **22**, (1954) 1063

[6] D.L. Dexter, *J. Chem. Phys*, **21** (1953) 836

[7] C. Ronda, *Lumineneschence*: *From theory to Applications by 2008 Wiley-VCH*

[8] A. Roda, *Chemiluminescence and Bioluminescence*, (2011) 26 chap.1

[9] P.D. Rock, A. Naman, P.H. Holloway, Sey Shing Sun, and R.T. Tuenge, "*Materials Used in Electroluminescent Displays*," http://www.distec.com/Electro.htm, accessed on July 13, (1999)

[10] Valeur (ed.) *Molecular Fluorescence – An Introduction: Principles, Applications, 1st Edition* (2000)

[11] O.M. Ntwaeaborwa,*Ph.D dissertation*, University of the Free State, (2006)

[12] C. Stoffers,.; S. Yang,.; S.M. Jacobsen,. and C.J. Summers,., *J. Soc. Inf. Display*. **4 (4)** (1996) 337-341

[13] R Raue., A.T. Vink and T Welker., *Phillips Tech. Rev*, **44 (12)** (1989) 335.

[14] J. T. van Wijngaarden, S. Scheidelaar, T. J. H. Vlugt,2 M. F. Reid, and A. Meijerink, *Phys. Rev* **B 81**, (2010) 155112

[15] W. Shockley and H. Queisser, *J. Appl. Phys*. **32**, (1961) 510

[16] W. Shockley, H. Queisser, *Journal of Applied Physics* **32** (1961) 510–519

[17] A Shalav, B.S Richards,. K Kramer,. H Gudel,. *Improvements of an up- conversion $NaYF_4:Er^{3+}$ phosphor/silicon solar cell system for an Enhanced response in the near-infrared*, in: Record of the IEEE Photovoltaic Specialists Conference, Institute of Electrical and Electronics Engineers (IEEE), (2005),p.114

[18] A. Shalav, B.S. Richards, K. Kramer, G. Conibeer, and M. Green, *Two-colour excitation up-conversion efficiency enhancement for a silicon photovoltaic device using Er^{3+} doped phosphors*, in: Record of the IEEE 4th World Conference on Photovoltaic Energy Conversion, Institute of Electrical and Electronics Engineers(IEEE),(2006),p.45

[19] B.M. van der Ende, L. Aarts, A. Meijerink, *Physical Chemistry Chemical Physics* **11** (2009) 11081–11095

[20] R. T. Wegh, H. Donker, K. D. Oskam, and A. Meijerink, *Science* **283**, (1999) 663

[21] H. Hovel, R. Hodgson, and J. Woodall, *Solar Energy Materials*, **2**, (1979)19–29

[22] A. M. Gabr, R. M. Beal, A. Walker, J. F. Wheeldon, J. Sacks, R. M. Savidge, T. J. Hall, R. N. Kleiman, and K. Hinzer, "*Modeling Down-Conversion and Down-Shifting for Photovoltaic Applications*," Conference proceeding for the 38th IEEE Photovoltaic Specialist Conference (PVSC), (2012)

[23] C. Strumpel, M. Mccann, G. Beaucarne, V. Arkhipov, a Slaoui, V. Svrcek, C. Delcanizo, and I.Tobias, *Solar Energy Materials and Solar Cells*, **91**, (2007) 238–249,

[24] P. Vergeer; T. J. H. Vlugt; M. H. F. Kox; M. I. den Hertog.; J. P. J. M. van der Eerden; A. Meijerink, *Phys. Rev*. **B**, **71**, (2005) 014119

[25] J.-X.Chen, S. Ye,X. Wang, J. Qiu. *Chin. Phys. Lett*. **25** (2008) 2078.

[26] J. Zhou, Y. Zhuang, S. Ye, Y. Teng, G. Lin, B. Zhu, J. Xie, J. Qiu, *Appl. Phys. Lett*. **95** (2009) 141101

[27] H. Lin, D. Chen, Y. Yu, Z. Shan, P. Huang, A. Yang, Y. Wang. *J. Alloys Compd*. **509** (2011) 3363

[28] D. Chen,Y, Yu., H. Lin, P. Huang, Z. Shan, Y. Wang,. *Opt.Lett*. **35** (2010) 220

[29] Chin-Tang San, *Fundamentals of Solid State Electronics,* World Scientific, Singapore, (1999) 278 chap. 3

[30] F.C. Auzel, *Acad. Sci. (Paris)*, **263** (1966) 819

[31] B.S. Richards, *Sol. Energy Mater. Sol. Cells*, **90** (2006) 1193

[32] C. Strümpel, M. McCann, G. Beaucarne et al, *Sol. Energy Mater. Sol. Cells* **91** (2007) 238-249

[33] K.A. Jr Gschneidner and A.H. Daane., " *Handbook on the Physics and Chemistry of Rare Earths*", eds Gschneidner K.A. Jr. and Eyring L., (Amstredam: North-Holland) vol. **11** (1988) 409

[34] C.R. Ronda, *J. Alloys Comp*. **225** (1995) 524–538

[35] C.R. Ronda, *J. Lumin*. **100** (2002) 301–305

[36] T. Ju¨ stel, H. Nikol, C. Ronda, *New developments in the field of luminescent materials for lighting and displays,* Angew Chem. Int. Ed. **37** (1998) 3084–3103

[37] P.H. Holloway, T.A. Trottier, B. Abrams, C. Kondoleon, S.L. Jones, J.S. Sebastian, W.J. Thomas, *J. Vac. Sci. Technol*. **B 17 (2)** (1999) 758–764

[38] P.D. Rack, P.H. Holloway, *Mater. Sci. Eng*. **R21** (1998) 171–219

[39] C.M. Varma *Rev. Mod. Phys.*, **48** (1976) 220

[40] V.C. Costa, M.J. Lochhead, K.L. Bray. *Chem Mater*; **8(3)** (1996)783–90

[41] M.J. Weber. *Non-Cryst Solids*;**123 (1–3)** (1990) 208–22

[42] W.R. Glomm, S. Volden, J. Sjöblom, M. Lindgren. *Chem Mater*;**17(22)** (2005) 5512–20

[43] H.St.C. O'Neill and W.A. Dollase, Phys. Chem. Minerals. 20 (1994) 541−555

[44] S.K. Sampath and T.F. Cordaro, J. Am. Ceram.Soc. 81 (1998) 649

[45] W.D. Kingery, *Structure of crystals, in: in: Introduction to Ceramics,* John Wiley & Sons, New York, (1960), 81-139

[46] N. J. van der Laag, M. D. Snela, P. C. M. M. Magusin and G. de With, *J. Eur. Ceram. Soc.* **24** (2004) 2417

[47] X. Wei and D. Chen, *Mater. Lett.* **60** (2006) 823

[48] R. Pandey, J. D. Gale, S. K. Sampath and J. M. Recio, *J. Am.Ceram. Soc.* **82** (1999) 3337

[49] V. Ciupina, I. Carazeanua and G. Prodan *J. Optoelectron. Adv.Mater.* **6** (2004)1317

[50] B.S. Barros, P.S. Mellow, R.H.G.A. Kiminami, A.C.F.M. Costa, G.F. de Sa, S. Alves Jr., *J. Mater. Sci.* **41** (2006) 4744–4748

[51] https://paulingblog.wordpress.com/2012/05/

[52] D. Panayotov, P. Kondratyuk, J.T. Yates, *Langmuir* **20** (2004) 3674–3678

[53] C.-K. Huang, C.-H. Hou, C.-C. Chen, Y.-L. Tsai, L.-M. Chang, H.-S. Wei, K.-H. Hsieh 1,C.-H. Chan, *Nanotechnology* **19** (2008) 5055701

[54] J. Bomm, A. Büchtemann, and J. Amanda. *J.Solar Energy Materials and Solar Cells*, , **95(8)** (2011) 2087-2094

[55] C.E. Chryssou, A.J. Kenyon and, C.W. Pitt, *Mater. Sci. Eng.* **B 81** (2001) 16,

[56] M. Ferrari and C. Armellini, *J. Sol-Gel Sci. Technol* **19** (2000)569

[57] M. Morita, S. Kajiyama , T. Kai, D. Rau and T. Sakurai *J. Lumin.* **94** (2001)91

[58] M.A. Garcia, E. Borsella, S.E. Paje, J. Llopis, M.A. Villegas and R. Polloni, *J. Lumin.* **93** (2001) 253 1-4

[59] G.S. Maciel, A. Biswas and P.N. Prasad, *Opt. Commun.* **178** (2000) 65

[60] G.S. Martin, A.C. Yanes, J. Mendez-Ramos, M.E. Torres and V.D. Rodriguez, *J. Appl. Phys.* **89 (5)** (2001) 2520

[61] V.I. Arbuzov, V. Ya. Grabovaskins, N.S. Kovaleva, U.T. Rogulis and M.N Tolstoĭ, *Opt. Spectrosc.* **65** (1988)555

[62] T. Förster, *Ann. Phys.* **2** (1948) 55-57

[63] D.L. Dexter, *Phys. Rev*. **B 108**, (1957) 630-633

[64] Inokuti and Hirayama, *J. Phys. Chem*. **43** (1965) 1978-1989

[65] G. Blasse. and B.C.Grabmaier, *Luminescent Material*, Springer-Verlag, Berlin, (1994)

CHAPTER 3 EXPERIMENTAL RESEARCH TECHNIQUES

3.1 Introduction

The structure, morphology and crystal sizes of the powder nanophosphor samples were analyzed using X-ray diffraction (XRD), Scanning electron microscope (SEM) and high resolution transmission electron microscopy (HRTEM). The absorption properties of the powder nanophosphors were studied using UV-VIS-NIR spectrophotometer. The photoluminescence (PL) and cathodoluminescence (CL) properties were determined using F-7000 Fluorescence and Ocean Optics S2000 spectrometers respectively. The stretching mode frequencies of the powder phosphors were determined by Fourier transform infrared spectroscopy (FT-IR). To obtain chemical analysis on the surfaces of different powder phosphors X-ray photoelectron spectroscopy (XPS) was used. Lastly, the luminescence life time measurements were performed using an inverted-type scanning confocal microscope coupled with a single-mode pulsed diode laser as an excitation.

3.2 X-ray powder diffractometer (XRD)

X- ray powder diffraction is a technique that has grown significantly lately. It is mainly used for structural analysis by identifying solid samples and determines their composition by analyzing the so-called "fingerprints" they generated when x-rayed. In 1912, [1] Max von Laue managed to develop the first description of the diffraction of X-rays by a crystal. Furthermore, Henry Bragg and his son Lawrence Bragg in 1913 [2] developed a much simpler way of understanding and predicting diffraction phenomena from a crystal. The well-known Bragg equation is given as

$$\lambda = 2d_{hkl} \sin\theta \tag{3.1}$$

In this development of the Bragg equation it was assumed that the incident X-rays are in phase and that they reflect from imaginary planes as shown in figure 3.1.

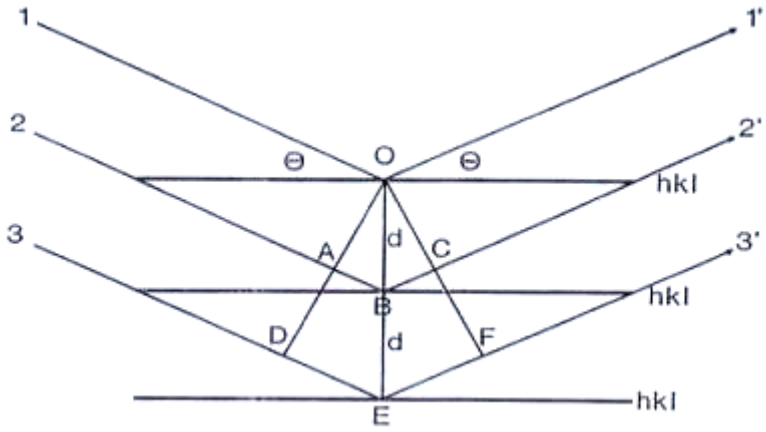

Figure 3-1 Bragg's law is easily seen to arise from an optical analogy to crystallographic planes reflecting X-rays [3].

The first X-ray powder Diffractometer was developed in 1935 by Le Galley [4]. By scanning the intensity of the diffracted x-rays as a function of 2Θ angles, all possible peaks emanating from reflection planes are observed. The x-ray diffractometer used in this current research to collect the XRD measurements was PANalytical X'Pert PRO using CuKα radiation of $\lambda = 1.5405$ nm. The technical settings of the instrument during the collection of data were set as follows; maximum power rating (30mA×40kV), ½ slit between the X-ray source and the specimen, step size of 0.034/°, 2θ range (10°−80°) with an X'Celerator detector. It should also be noted that there are five basic movements in any powder diffractometer geomentry, namely; (a) Angular motion of the X-ray tube, (b) angular motion of the specimen, (c) Angular motion of the receiving slit, (d) linear motion of the tube to specimen dimension and (e) linear motion of the receiving slit to specimen dimension. Figure 3.2 shown below is a schematic diagram of common mechanical movements in powder diffractometers. According to Bragg-Brentano [5] the common arrangements can be such a way that the tube is fixed and the specimen and receiving slit (RS) vary in the ratio of θ_1 to $2\theta_2$ (θ:2θ) or the specimen is fixed and the tube and receiving slit each vary as θ (θ:θ).

Thus, in each case the tube –specimen distance (r_1) and the specimen receiving slit distance (r_2) are fixed and equal to each other.

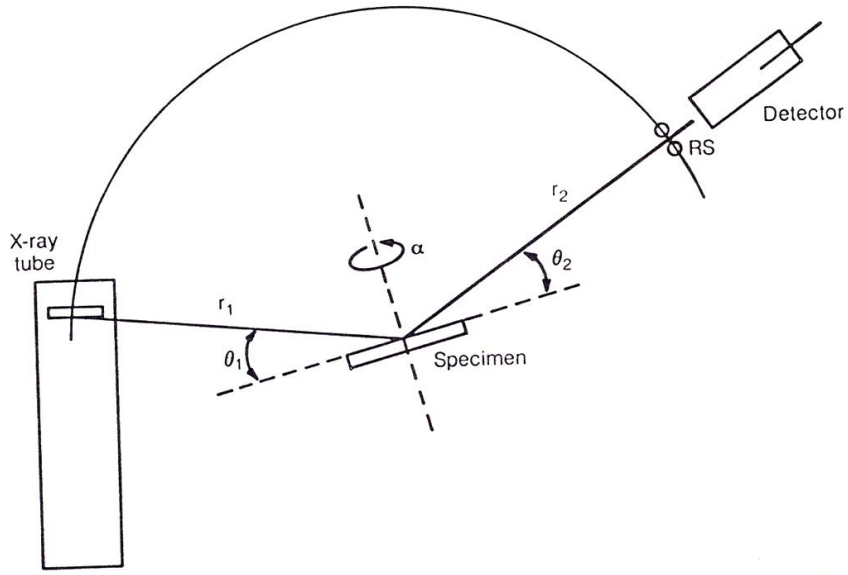

Figure 3-2 Schematic diagram of common mechanical movements in powder diffractometers [5]

3.3 Scanning electron microscopy (SEM)

The scanning electron microscope (SEM) is extremely useful for producing the imaging surface and subsurface microstructure through the scanning of the sample with a focused beam of high energy electrons. The electron-sample interaction can generate various signals that can be detected and reveal the information about the sample's surface topography, chemical composition and orientation of materials making up the sample. A selected area of the surface sample normally ranges from approximately 1 cm to 5 microns I width serves as a place where data can be collected through the use of the scanning mode from conventional SEM techniques. The magnification can range from 20 × to approximately 30, 000 × with a spatial resolution of 50 to 100 nm. The SEM is also useful to perform the point analysis or locations on the sample qualitatively or semi-quantitatively in determining the chemical compositions (using EDS). The beam of electron is focused by one or two condenser lenses to a spot about 0.4 nm to 5 nm in diameter. Therefore, the beam

passes through pairs of scanning coils or pairs of deflector plates. Accelerated electrons in an SEM carry significant amounts of kinetic energy ranging from 0.2 keV to 40 keV. The energy of these electrons will then dissipate as a variety of signals produced by electron-sample interactions when the incident electrons are decelerated in the solid sample.

During the electron-specimen interaction in the SEM there are various signals produced and these can give significant information about the penetration depths, which give rise to the different signals from thick specimens and the calculated volume. The interaction volume is mainly defined as the volume where at least 95% of the electrons are brought to rest by scattering, which has a special characteristic teardrop shape as shown in the Fig.3.3 below. Materials with high atomic number will display partial electron penetration depths and increased lateral spread relative to those of lower atomic number.

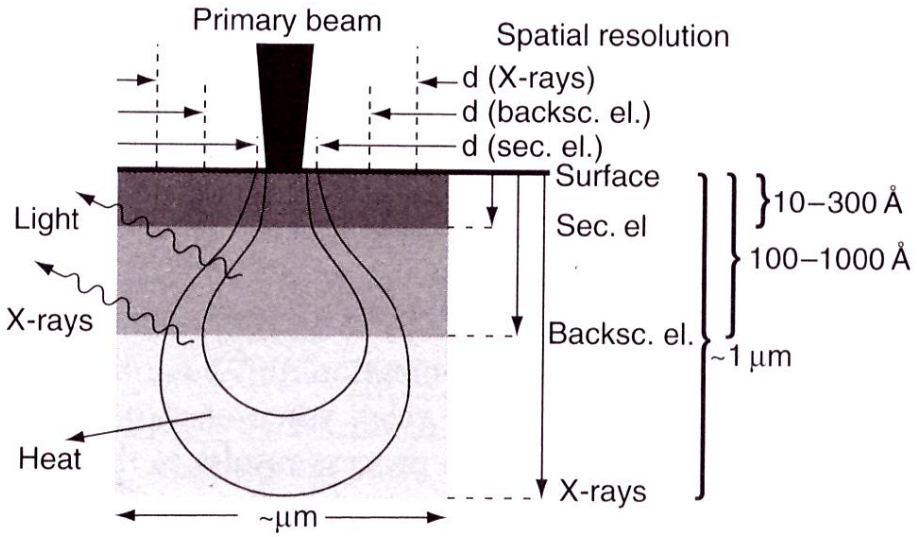

Figure 3-3 Schematic diagram of the beam-specimen interaction in a thick specimen [6]

3.4 High resolution Transmission electron microscopy (HRTEM)

High resolution transmission electron microscopy (HRTEM) is the imaging mode of the conventional transmission electron microscope (TEM) that allows an imaging of the internal microstructure of ultrathin specimens. The electron gun is usually thermionic

tungsten which can be resistively heated to 2800 K in a vacuum of 0.1 mPa to give an electron sufficient energy to overcome the work function of the metal. The anode potential is considerably higher than in an SEM and is typically 100 – 400 kV. TEM specimens in this study were normally in the form of powders. The powders were ground and dispersed onto an amorphous film (carbon tape) on a circular metal grid.

The system can also be useful for determining the electron diffraction patterns of different materials such as amorphous, polycrystalline and single crystal. Amorphous materials mainly exhibit diffuse diffraction rings related to the average interatomic separations. For crystalline materials, the periodic arrangement of atoms scatters the electrons through well-defined angles given by Bragg's law. Therefore, diffraction occurs only when the planes of atoms are closely parallel to incident beam of electrons as shown in figure 3.4 below. In this study, the HRTEM images of the powder samples were obtained using the FEI Tecnai F 20 G2 model. The operational technical settings from this system are, namely: Accelerating Voltage 50 ~ 200kV, image resolution < 0.23 nm, electron probe size < 0.3 nm, EDS detector Si(Li) detector and CCD camera.

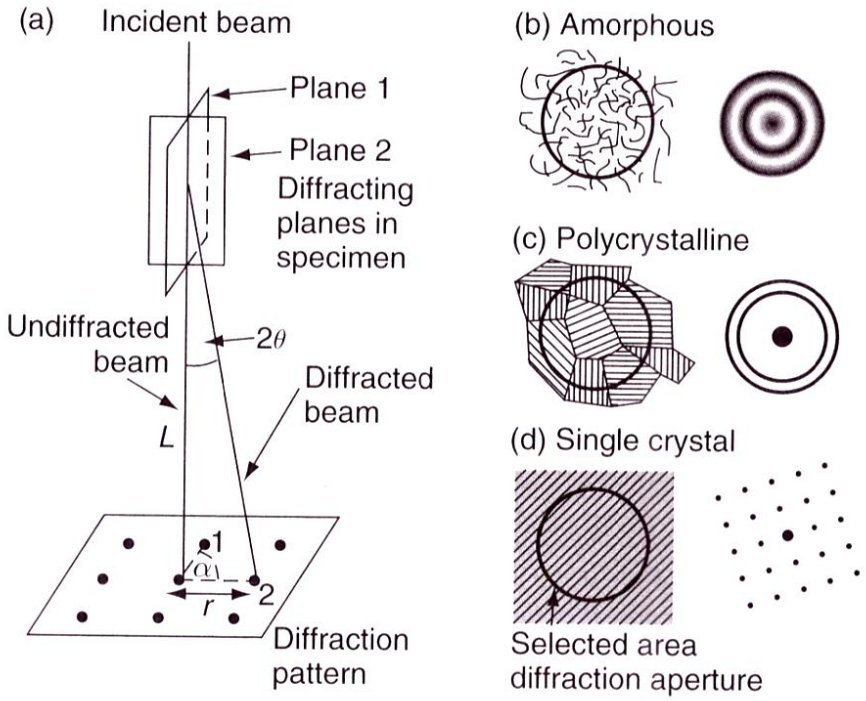

Figure 3-4 Schematic diagram of (a) the geometry of electron diffraction in the TEM and the form of the diffraction pattern for (b) amorphous, (c) polycrystalline and (d) single-crystalline sample regions [6]

3.5 UV-Vis-NIR spectrophotometer

In simple terms, absoption techniques involve a measurement of the attenuation of the intensity of a monochromatic light beam as it traverses the sample. There are also four mechanisms by which electromagnetic radiation can interact with condensed matter. These mechanisms are rotational, vibrational, electron excitation and free carrier.

For the molecular rotation, it is understood that molecules possessing permanent electric-dipole moments contribute to the complex dielectric constant by changing their orientation due to the external effect of the electric field. In special cases, molecules in gases and liquids when normally exposed to external electric field, they cause a large electric polarizability from their permanent dipole moments. However, in a solid the ability of a molecule to rotate depends on its shape and the strength of its interactions with its environment. Consequently, the more nearly spherical the molecule and the smaller its

dipole moment, the more easily it rotates. Molecules often have several stable orientations in the solid and these may vary from one orientation to another during an interval called relaxation time.

On the lattice vibrations, our focus is to consider the solid to be made up of positive and negative ions arranged in a periodic array, with each ion able to vibrate about its equilibrium position. In the quantum-mechanical description the lattice vibrations are considered to be made up of waves (phonons), with descrete, quantized energy levels. In this case the radiation can be absorbed by causing the lattice to jump from one vibrational state to another of higher energy. Thus, in order to restore the stability, the system may return to the lower state through a radiationless transition in which phonons are also being generated and the absorbed energy ultimately appearing as heat. Lastly, the strong absorption bands associated with fundermental lattice vibrations occur in the thermal infrared.

In the context of understanding the electron excitation, we need to first remember that absoption processes in the near ultraviolet, visible, and near infrared can occur by different mechanisms. Most of them can be classed as transitions in which single electrons are induced by the external radiation to jump from one state of lower energy to one of higher energy. In general, the last mechanism based on free carriers is mainly described as an absorption of light by free carriers of charge, including both electrons and holes in a solid when they are stimulated to move by the electric field of the incident radiation and the collution with the lattice, through the conversion of some of the energy of the radiation into lattice vibrations.

In the current study, the UV-VIS-NIR spectrophotometer was used as a technique which measures the intensity of light radiation passing through a solid sample (I), and compares it to the intensity of light radiation before it interacts with the sample (I_0). The main emphasis on the use of this technique was based more on applying the Tauc's relation [7] in order to

determine the band gap of our powder samples. The Varian Cary 100 Conc. UV-Vis spectrophotometer was used in this study.

3.6 Fluorescence Spectroscopy

Fluorescence spectroscopy is a type of electromagnetic spectroscopy which is used to analyze the fluorescence or phosphorescence from a sample. A beam of light, usually ultraviolet light is used to excite the electrons in a sample and causes it to emit light. The technique which is used to measure the fluorescence intensity is mainly called the fluorescence spectrophotometer. Usually this technique is used to measure the different fluorescence intensities emitted from the samples and it is mainly coupled with the following accessories in order to function very well, namely; radiation source (150 W−Xenon lamp), monochromator (excitation and emission sides), sample holders for both powder and liquid samples; a photomultiplier and sets of slits (Excitation and Emission). The light from the radiation source enters through the excitation side monochromator, and part of the light from the monochromator is directed into two directions, that is, to the monitor detector and the desired sample by beam splitter. The complete illustration of the signal processing and control system is shown in Fig.3.5. The main function of the monochromator is to provide high resolution and the spectral purity through the use of the narrow slits [8]. In the current study the photoluminescence excitation and emission spectra of the aluminates and silicates phosphor powders were recorded and analyzed. Photoluminescence (PL) spectroscopy is mainly defined as a non-destructive, non-contact method for probing an electron structure of the materials. This is mainly possible by exciting a sample with a laser tuned to a particular wavelength or the xenon lamp where the excitation wavelength can be varied. The generated photons can be collected from the front surface and be presented in the form of PL intensity as a function of wavelength.

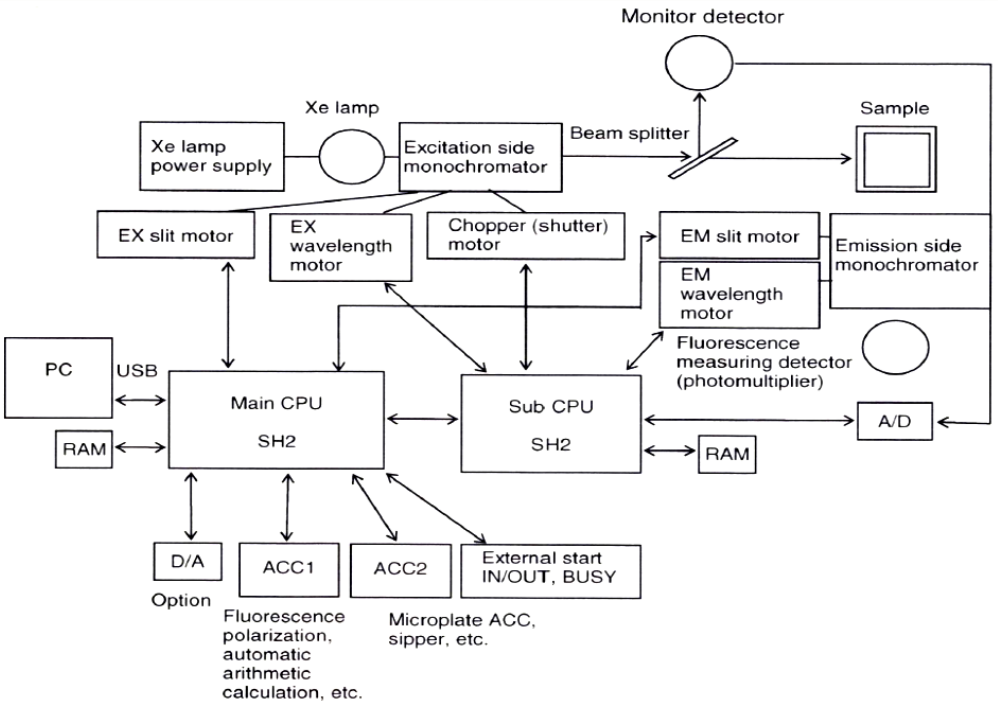

Figure 3-5 Schematic diagram of the Signal Processing and control system [9]

3.7 Cathodoluminescence spectroscopy (CL)

Cathodoluminescence (CL) is generated by the recombination of electron-hole pairs produced by probing the sample with an electron beam. The CL system used in this study was attached to a vacuum chamber of the Physical Electron (PHI 549) Auger electron spectrometer. The system uses a fibre to collect the emitted photons generated from the sample and transmit them to the CL spectrometer and get displayed on the computer screen. One interesting thing which can be performed with this combined AES-CL system is the Auger electron spectroscopic (AES) analysis whereby the surface of the sample can also be probed from the same electron beam and the CL and AES data can be correlated. The motivation to contemplate the use of the surface studies is due to the fact that CL generation occurs closely to the surface of the phosphor, whereby the surface chemistry has shown the potential of influencing the efficiency of the phosphor. In the current study the CL measurements were primarily performed in order to determine the chemical stability of our phosphor after it has been exposed to the primary electron beam for 10 hours. The technical

settings employed during data collection were as follows; Accelerating voltage 2 kV, beam current 10μA, pressure was set at 1.0×10^{-7} Torr (O_2 atmosphere), sensitivity 20 ×, scan rate 4eV/sec and the beam size /diameter 228 μm. The PHI model 549 Auger electron spectrocopy (AES) and Ocean Optics Inc. PC 2000 were used in this study to perform the CL and AES measurements as shown in the schematic Fig 3.6 below.

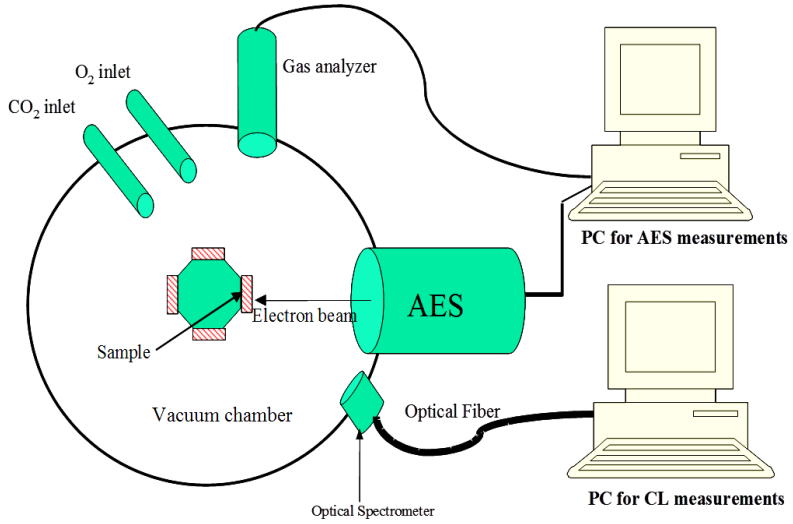

Figure 3-6 Schematic diagram of the PHI 549 Auger system (AES) [10]

3.8 Fourier transform infrared spectroscopy (FTIR)

The energy of most molecular vibrations corresponds to the infrared region of the electromagnetic spectrum. The detection of these vibrations is mainly measured in an infrared (IR), which typically covers a wavelength range of 2 – 16 μm (commonly expressed as 400 – 5000 cm^{-1}). The IR spectrometer system consists of an IR source emitting throughout the whole frequency range. While the source is emitting throughout, the beam is split, with one beam passing through the sample (transmission) or reflected (for studies of surfaces) while the other beam is employed as a reference beam. Taking into consideration that samples to be measured may be in different forms, such as; vapour or solution contained in NaCl cell, a liquid between NaCl plates e.tc. In this study the sample was in a form of a solid ground together with excess KBr and pressed into a disc. The prepared sample was then loaded into Fourier transform IR (FTIR) spectrometer which normally works by

allowing transmitted (or reflected) beam to recombine with the reference beam after a path difference has been introduced. The interference pattern generated is Fourier transformed to produce the spectrum of material being analysed as a function of wavelength or wavenumber of the incident radiation. Lastly, if the molecular vibration is excited in the sample, the molecule absorbs energy of the particular frequecy and this is detected as absorption relative to the reference beam. Furthermore, different functional groups have characteristic vibration frequency arising due to stretching, bending, rocking and twisting of bonds which allows the particular functional group to be identified. The schematic diagram of the IR spectral regions for different chemical bonds in organic materials is also shown in Fig.3.7.

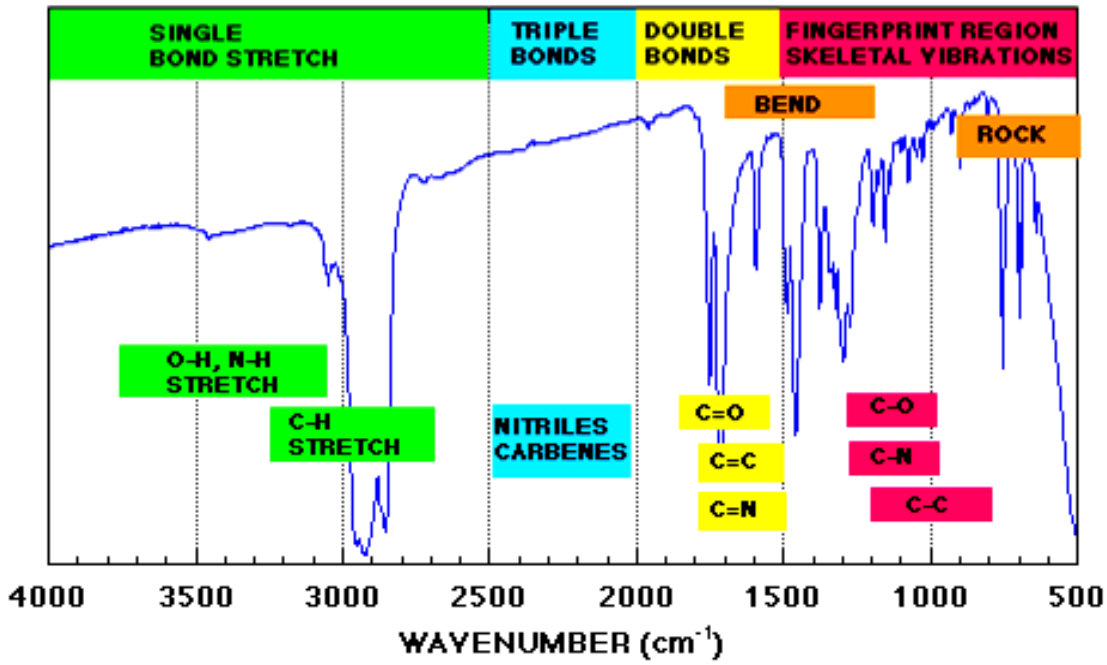

Figure 3-7 Diagram of the IR spectral regions for different chemical bonds in organic materials [11]

3.9 X-ray photoelectron spectroscopy (XPS)

X-ray photoelectron spectroscopy (XPS) has shown the greatest applicability to the widest range of materials surfaces. XPS as a technique is mainly dependent on the analysis of low-energy electrons emitted from the surfaces, in the range 10 – 3000 eV. In XPS the sample is irradiated with a beam of usually monochromatic, in this case is AlKα lines, precisely low-energy X-rays. Photoelectron emission results from the atoms in the specimen surface and the kinetic energy distribution of the ejected photoelectrons is measured directly using an electron spectrometer. The kinetic energy distribution of the ejected electron depends on the photon energy of the X-rays irradiated on the sample and as a result, it is not an intrinsic material property [12]. The binding energy of each core-level electron is characteristic of the atom and identifies the electron specifically, both in terms of its parent element and orbital to which it belongs. Since the energy of the incicent X-rays is known, the measured kinetic energy of a core-level photoelectron peak can be related directly to its characteristic binding energy. The XPS data collection was carried out using VG Scientifics-ESCALAB 250 XPS and PHI5000 XPS Versaprobe respectively. The ESCALAB 250 is equipped with a monochromatic X-ray source and optional twin anode source is also available. Any size of X-ray spot at the sample can be selected over a range of 120 μm to 650 μm. This system has the combination of lens/analyzer/detector that makes it to be unique for both imaging and small area XPS. A schematic diagram of ESCALAB 250 operating in its spectroscope mode coupled with an array of 6 channel electron multipliers is shown in Fig.3.8 below.

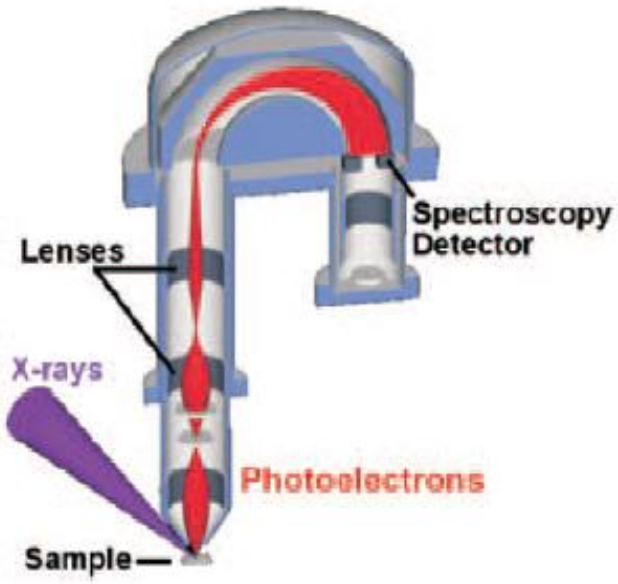

Figure 3-8 Schematic diagram of ESCALAB 250 operating in its spectroscopy mode [13]

On the other hand, the PHI VersaProbe XPS can generate a focused, highly monochromatic X-ray beam that can be scanned over the specimen surface. The focused X-ray beam can be scanned across the specimen surface by correspondingly scanning the electron beam across the surface of Al anode. The spot size can be varied between less than 10 μm diameter (for highest special resolution) to 100 μm (for highest sensitivity). The field of view can be as large as 1500 μm by 1500 mm.

3.10 Time-resolved Fluorescence Microscope

The fluorescence lifetime measurements were conducted using Micro Time – 200, Picoquant microscope. The flexible excitation subsystem of the Micro Time 200 consists of a pulsed diode laser (PDL) driver of the PDL series and different laser heads with pulses in the picosecond time regime. The range of the wavelengths available in this instrument is from 375 nm to 900 nm. This system is highly suited for the analysis of the phenomena that determine fast charge carrier dynamics in a semiconductor. Thus, the mechanism that determines the charge carrier dynamics with a particular system can be characterized directly down to the sub-nanosecond time scale. Figure 3.9 shows the schematic diagram which can

be used to perform the Time-Resolved Photoluminescence (TRPL) measurements. TRPL via Time-Correlated Single Photon Counting (TCSPC) is particularly suited for fast charge carrier dynamics in the nanosecond regime. The essential components of the a set-up for measuring fluorescence lifetimes are: pulsed laser source, single photon sensitive detector, monochromator or optical filters and TCSPC unit to measure the time between excitation and fluorescence emission. Finally, this powerful instrument can also analyze quite a large number of parameters down to the single molecule level with the use of different methods such as fluorescence lifetime imaging (FLIM) or deep UV detection.

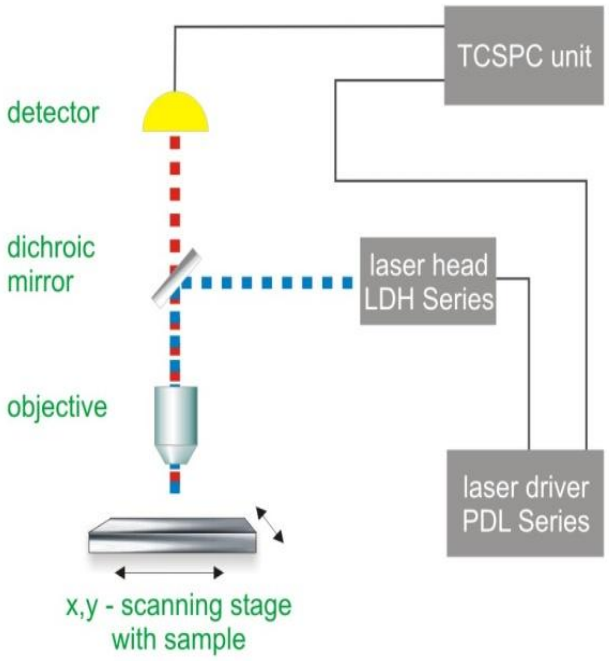

Figure 3-9 Schematic diagram of the spectrometer used for Time-Resolved Photoluminescence (TRPL) measurements [14]

3.11 References

[1] Ewald, *50 Years of X-Ray Diffraction* **Chapter 4**, pp. 37-42.

[2] *The Nobel Prize in Physics* (1915), *Nobel Foundation. Retrieved* (2008),10-09.

[3] R. Jenkins, R. L. Snyder, *Introduction to X-ray powder diffractometry*, (1996) 48.

[4] D.P. Le Galley, *Rev. Sci. Instrum.* ***6,*** (1935) 279-283.

[5] W. Parrish, E.A. Hamacher and K. Lowitzsch, *Philips Tech. Rev*. **16** (1954) 123−133.

[6] R.W Robert, I.W Hamley and M Geoghegan *Nanoscale Science and Technology*, John Wiley & Sons, (2005) 71.

[7] J. Tauc, R. Grigorovici and A. Vancu, *Phys. Status Solidi*, **15** (1966) 627.

[8] *The international Pharmacopoeia, Organization Mondiale de la santè,* World Health Organization, Fourth Edition, Volume 1, Geneva, (2006).

[9] F-7000 Fluorescence spectrophotometer manual

[10] O.M. Ntwaeaborwa, *PhD dissertation*, University of the Free State (2006)

[11] http://structureandfunction.wordpress.com/ir-spectroscopy/2013/02/05/

[12] J.K. Watts, J. Wolstenholme, *An Introduction to Surface Analysis by XPS and AES*, Copyright ©John Wiley & Sons Ltd, the Atrium, Southern Gate, Chichester, West Sussex PO 19 8SQ, England, (2003)

[13]http://www.thermoscientific.com/en/home.html/2014/04/17

[14] http://www.picoquant.com/ 2015/03/26

CHAPTER 4 SYNTHESIS, STRUCTURE AND UV-VIS PROPERTIES OF $ZnAl_2O_4$ and SiO_2 HOST LATTICES

4.1 Introduction

Traditionally, $ZnAl_2O_4$ with normal, intermediate or inverse spinel structure is widely used as a catalyst or ceramic [1]. Today, it is used in many applications such as optoelectronics, sensor technology and information display technology [2-5] because of its excellent optical and hydrophobic properties and high chemical and thermal stability [6]. For application in display technologies, $ZnAl_2O_4$ is used as host matrix for trivalent rare-earth ions (e.g. Tb^{3+}, Eu^{3+} and Dy^{3+}) [7, 8] or transition metals (e.g. Mn^{2+} and Cr^{3+}) [9, 10] to prepare phosphors emitting mostly in the visible range of the electromagnetic spectrum.

Silica (SiO_2) is widely used in many fields such as medium layer and silicon-based photoelectron material because of its excellent chemical stability, thermal stability as well as interfacial combination with silicon semiconductor. However, taking into consideration that SiO_2 can either be produced in the crystalline or amorphous form, it has then stimulated a long history of experimental and theoretical investigations. SiO_2 doped with metal ions are of particular interest from the viewpoints of physics and their applications as luminescence materials. The mostly used activator ions in order to enhance the luminescent properties of the oxide materials, is mainly selected from REs or transition metal ions [11−14] due to their unique electronic structures.

This chapter presents the combustion and sol-gel syntheses of $ZnAl_2O_4$ and SiO_2, their structure and UV-Vis properties.

4.2 Traditional preparation method

The synthesis of solid materials possessing desired structures and properties has continued to present some challenges to chemists and material scientists. The traditional

preparation method by solid state reaction is mainly controlled by the diffusion process on atoms or ionic species through reactants. Therefore, the desired products require some repeated grinding which involves a long duration during the calcinations of oxides or carbonates at high temperatures. The particle size of the as-cast samples turns to be too large for display applications and this is mainly due to the diffusion control problems of solid state synthesis [15].

Booth [16] reported the best method which can sustain itself and propagate in the form of a combustion wave until reactants decomposes completely. This method is called combustion synthesis and it makes use of highly exothermic redox chemical reactions between metals and nonmetals. The terminology used in explaining the combustion process mainly covers the gas phase (flaming), smouldering (heterogeneous) and also the explosive reaction.

Currently there is a great interest in the use of combustion synthesis because of the following advantages: ease of preparation, fast heating rates, short reaction time (~ 5 min), cost effectiveness and yielding of high purity products. The success of this method has been evident through some preparation of different technologically useful oxide materials, for example, refractory oxides, catalyst, phosphors etc. and non-oxides such as borides and silicides. In all of this, combustion synthesis has been regarded as an important technique to the preparation of advanced materials [17,18]. Combustible redox mixture of oxidiser and fuel is used, which when ignited undergoes self-propagating low temperature ($< 500^{o}C$) combustion. The type of the fuel used can also describe the nature of the combustion that will take place in obtaining a complete decomposing of reactants [19]. The well known fuels, which have demonstrated the versatility for combustion synthesis, are urea (CH_4N_2O) and glycine ($C_2H_5NO_2$) [20].

Stoichiometric composition of the redox mixture for solution combustion is calculated using the total oxidizing (O) and reduction (F) valencies of the components, which serve as the numerical coefficients for the stoichiometric balance so that equivalence ratio (Φ) is unity (i.e. O/F = 1) and the energy released by the combustion is maximum [21]. $ZnAl_2O_4$ and SiO_2 doped with different concentrations of Ce^{3+}/Tb^{3+} were prepared using the solution combustion synthesis route. The final products obtained after the synthesis had a low density and a fluffy or porous texture. The typical chemical balanced equation of the reactants and product for un-doped zinc aluminate is given below:

$$3Zn\,(NO_3)_2 \bullet 6H_2O + 6Al\,(NO_3)_3 \bullet 9H_2O + 20H_2NCONH_2 \rightarrow 3ZnAl_2O_4 + 106H_2O + 20CO_2 + 32N_2$$

4.3 Sol-gel synthesis

The sol-gel process is mainly based on wet chemistry. During the sol-gel synthesis, metal alkoxides are used to produce glasses or ceramics and the preparation process follows chemical reactions such as hydrolysis, gelation, drying and some thermal treatment. The word "sol" is typically known as a stable dispersion of colloidal particles or polymers in a solvent. Therefore, the particles may be amorphous or crystalline. On the other hand, a "gel" consists of a three dimensional continuous network, which mainly encloses a liquid phase. For example, in a colloidal gel, the network is built from agglomeration of colloidal particles. Generally, the sol particles may interact by van der Waals forces or hydrogen bonds.

In simple terms, the idea behind the sol-gel synthesis is basically to dissolve the compound in a liquid in order to bring it back as a solid in a controlled manner. An advantage about this method is that it enables mixing at an atomic level, resulting in the production of relatively smaller particles, which are easily sinterable. The precursors used in this method are a kind of metal-organic compounds, known as alkoxides of metals (e.g

tetraethyl orthosilicate $Si(OR)_4$ or titanium alkoxide $Ti(OR)_4$ where R = C_2H_5, that is organic constituent). These types of metal organic alkoxides can be found to be in liquid form or soluble in certain organic solvents. If the desired products should be a powder or ceramic samples, the gels can be baked, sintered, and powderized as in other traditional methods outlined in section 4.2

This sol-gel process offers a low temperature non-melt route that gives high purity, homogeneous composition and controlled particle size [22]. Because of being energy efficient, it turns out to be receiving a considerable attention in preparing compositions that are difficult to make by conventional methods. This is mainly achieved because of the following advantages, namely: molecule-level-homogeneity multi-component materials can be obtained; higher doping concentration due to non-existence "local" concentration quenching because of impurity clustering; and the controlled microstructure (porosity and size pores) of the materials.

In general, the sol-gel process is characterized by a series of different steps:

Step1. The sol-formation of different stable solutions

Step 2. Gelation resulting from the formation of an oxide

Step 3. Aging of the gel – a very important stage in the process

Step 4. Drying of the gel

Step 5. Dehydration

Step 6. Densification and decomposition of the gels at high temperatures

In this current study the sol-gel method was only used to prepare SiO_2, $SiO_2:Ce^{3+}$, $SiO_2:Tb^{3+}$ and co-doped $SiO_2:Ce^{3+}$, Tb^{3+} phosphor samples. The main emphasis in the study of these systems was to investigate the efficient energy transfer from Ce^{3+} to Tb^{3+} ions.

4.4 Experimental details

$ZnAl_2O_4$ samples were prepared by combustion method. The precursors used were analytical (AR) grade zinc nitrate hexahydrate, aluminium nitrate nanohydrate, and a fuel (Urea- ACS reagent). All these materials were of AR grade from Sigma Aldrich (South Korea) with ~ 99% purity. In a typical traditional method using combustion process, all the stoichiometric amounts of the starting materials were dissolved in de-ionized water. In Figure 4.1 the schematic diagram of the typical combustion process is shown. The preparation temperature which was maintained in a muffle furnace in order for the combustion reaction to take place was set to be roughly 500 ± 5ºC. One powder sample was then annealed in air at 700º C for 2 hours.

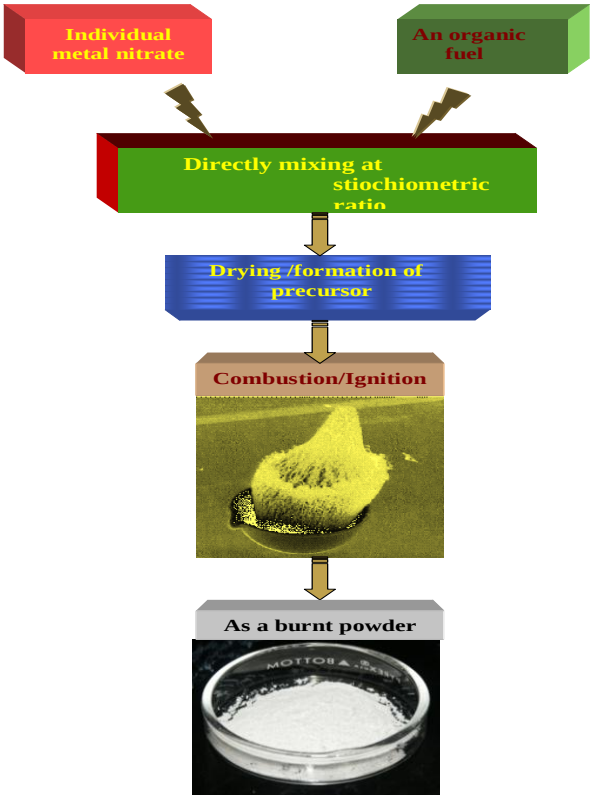

Figure 4-1 Mechanism of solution combustion synthesis of $ZnAl_2O_4$ and SiO_2

Nano sized pure SiO_2 powder sample was prepared by a solution combustion method as described in reference [23]. Silicic acid ($SiO_2 \cdot nH_2O$) and ammonium nitrate (NH_4NO_3) were used as the starting materials, urea (CH_4N_2O) was used as fuel. All these materials were dissolved in 10 mL distilled water and stirred for 2 hours in order to obtain a homogeneous transparent mixture. The mixer was then transferred into a muffle furnace which was maintained roughly at 500 ± 5ºC. Lastly, the dried powder after the incorporation of dopants was then annealed in a reducing atmosphere (4% H_2 and 96% Ar) gas at 1000ºC for 2 hours.

SiO_2 were prepared by the sol-gel process from the following starting materials: Tetraethylorthosilicate (TEOS), distilled water, ethanol (as a solvent) and nitric acid to catalyze the chemical reaction. After a vigorous stirring on a hot plate maintained at 40ºC, the gelation mixer was observed as a result of the formation of an oxide. This mixer was then transferred into an open flat-disc like container and was allowed to dry at room temperature.

When the gel was dried, it was ground by using a pestle and mortar and later annealed in a reducing atmosphere composed of 4% H_2 and 96% of Ar gas at 1000ºC for 2 hours.

4.5 Results and discussion

4.5.1 X- ray diffraction studies

Figure 4.2 shows the XRD spectra of as-prepared $ZnAl_2O_4$ and annealed sample of $ZnAl_2O_4$ in air at 700º C. The XRD spectra confirm a highly crystalline face-centered cubic spinel $ZnAl_2O_4$ with a space group *Fd3m*. These identical XRD patterns suggest that a highly crystalline $ZnAl_2O_4$ phase can be obtained without the use of post annealing directly prepared from a solution combustion method of synthesis. One interesting observation from the XRD patterns is that the peak intensities obtained corresponds well with the spinel structure reported by Zawadzki et al [24]. However, there is only $ZnAl_2O_4$ spinel as the detectable phase, the XRD also reveal the small traces of ZnO at 34.7º which appears as a secondary phase [25].

In figure 4.3 the XRD spectra of SiO_2 hosts prepared from Combustion and sol-gel routes are shown respectively. The XRD spectrum of SiO_2 in black has a peak position at $2\theta \sim 22^º$ and due to the fact that this peak shows a shift towards lower diffraction angles suggest the evolution of crystalinity due to nucleation through the formation of nuclei. It can also be stated that the presence of the uniform microstrain influences the location of the diffraction peaks from the low quartz sample. The peak shift to lower diffraction angles gives a clear evidence that the strain induced broadening calculated from Williamson-Hall method (40%) is high, and the estimated crystallite size was calculated from (100) reflection as 1.72 nm using the Scherrer equation [26]. On the other hand, the broad peak positioned at $2\theta \sim 23^º$ in red for SiO_2 is assigned to an amorphous phase [27, 28]

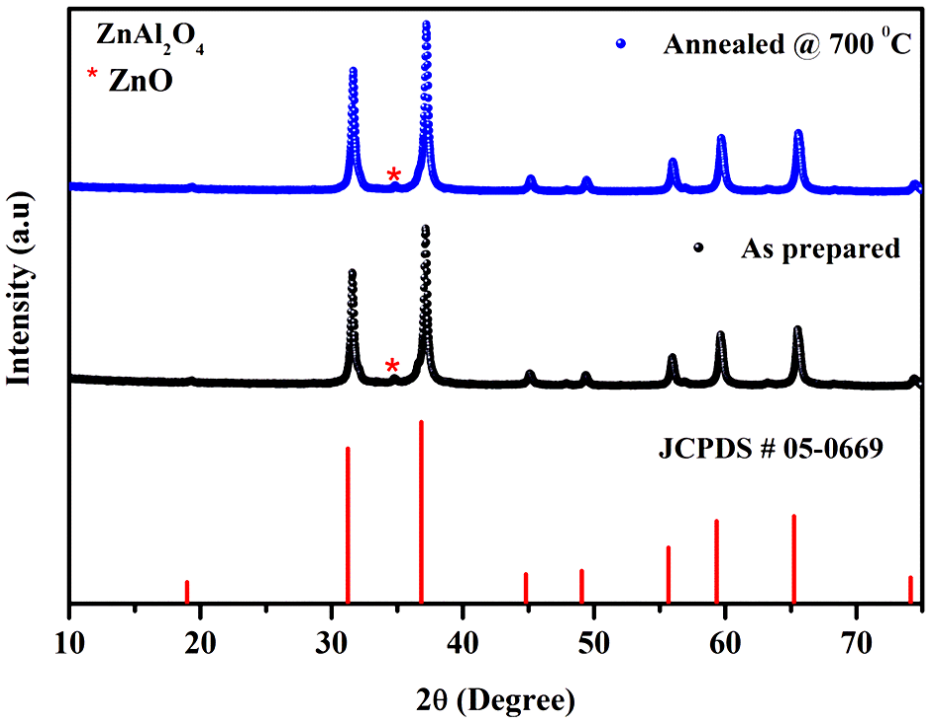

Figure 4-2 Room temperature (RT) XRD spectra of $ZnAl_2O_4$ as-prepared and $ZnAl_2O_4$ annealed at 700°C.

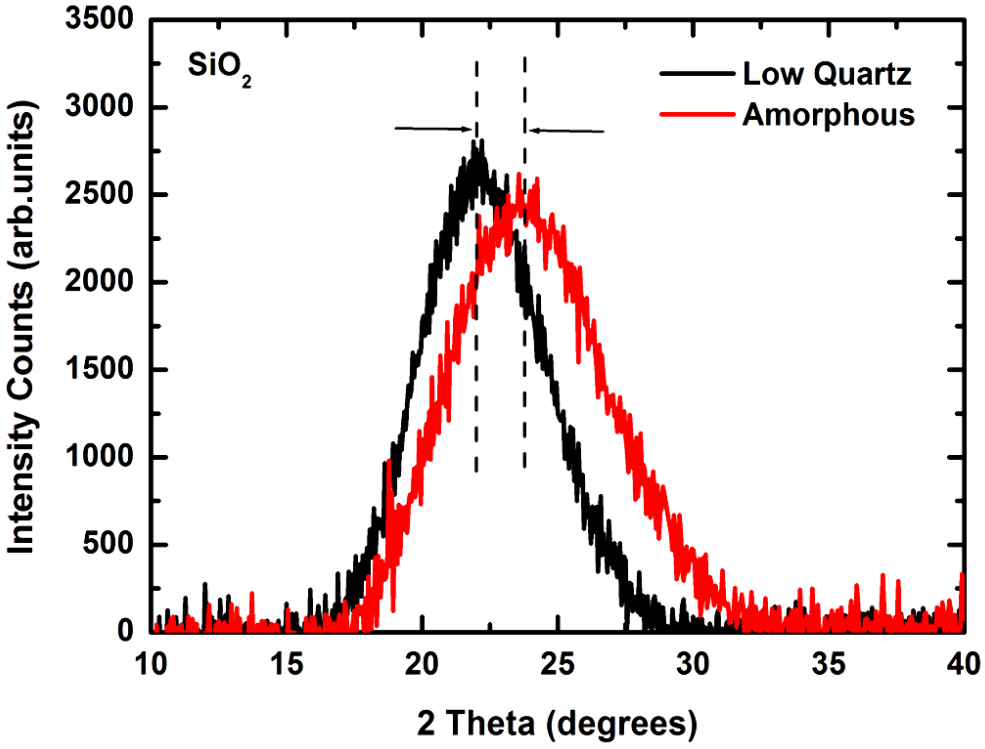

Figure 4-3 Room Temperature (RT) XRD spectra of low quartz and amorphous SiO_2 hosts

4.5.2 UV- Vis Characterization in $ZnAl_2O_4$

The UV – vis absorption spectrum of un-annealed $ZnAl_2O_4$ is compared with annealed spectrum in figure 4.4. In both spectra there is intense absorption below wavelength of 400 nm, that is, 360 nm from the annealed sample with a slight shift towards blue region compared to 358 nm of un-annealed sample. This absorption is known as a strong absorption of ZnO, and it corresponds to a charge –transfer process from the valence band (O 2p orbits) to the conduction band (Zn 4s orbits) [29, 30]. This result confirms the presence of ZnO in these samples which is in agreement with XRD results. The peak wavelength of 260 nm is a little stronger from the un-annealed sample compared to that of annealed one, and this peak is due to electronic excitations between filled O 2p orbits and empty Al 3s orbits [26].

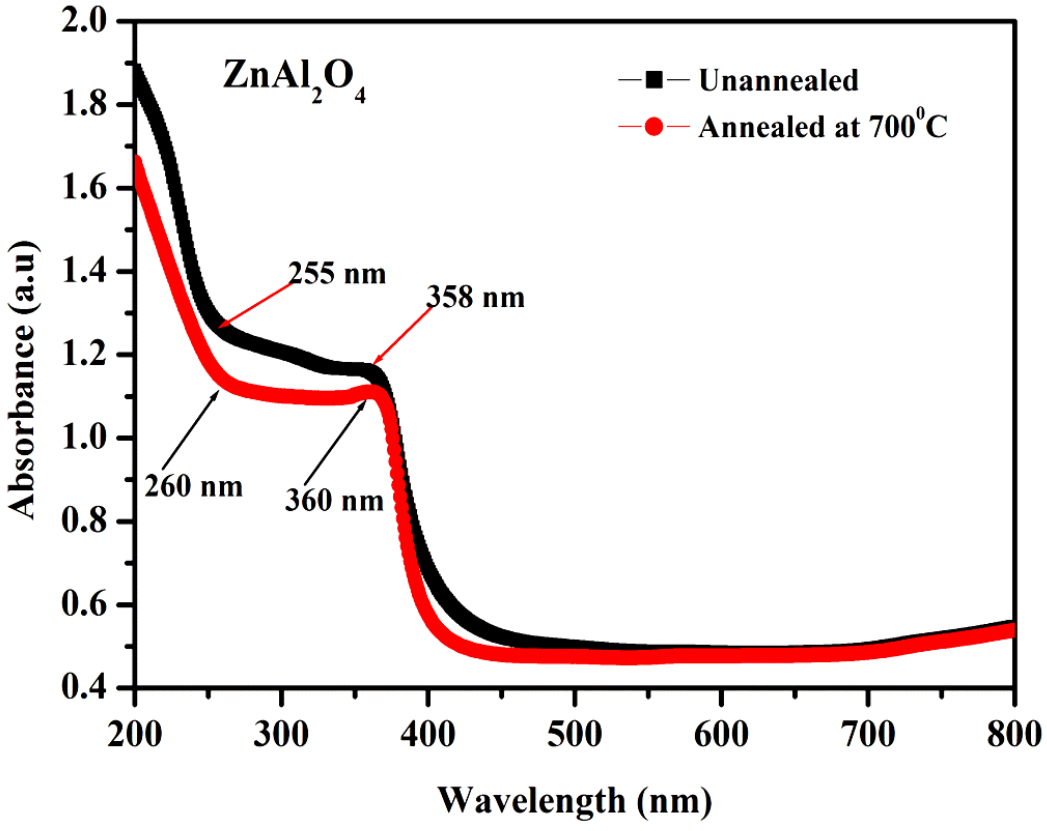

Figure 4-4 The UV-vis absorption spectra of the $ZnAl_2O_4$ (un-annealed and annealed)

4.5.3 UV- Vis Diffused reflectance in SiO_2

The UV-Vis diffused reflectance spectra of low quartz and amorphous SiO_2 hosts are shown in figure 4.5. The diffused reflectance of low quartz sample shows weak absorption at 240 and 310 nm attributed to Si-O type defect. The amorphous sample shows one absorption band at 220 nm. Another interesting observation on the diffused reflectance for low quartz is the shift towards a lower wavelength in the region 300 – 440 nm compared to that of an amorphous sample. This shift can be attributed to a decrease in particle size when the degree of disordered phase is getting reduced as evident from XRD analysis. Figure 4.6 shows the plot of transformed Kebelka-Munk reflectance versus band gap energy. The estimated values of band gap energies are 5.2 eV for low quartz and 5.3 eV for amorphous respectively. Considering the average value 5.25 eV, it can be observed that band gap energy of a bulk SiO_2 is higher (BG ~ 11.8 eV). This decrease of the average band gap energy of both low quartz and amorphous SiO_2 can be attributed to the so called shrinkage effect. The shrinkage can be due to the introduction of some impurities of continuum donor energy levels near the conduction band or a continuum of acceptor energy levels created near the valence band edge [31].

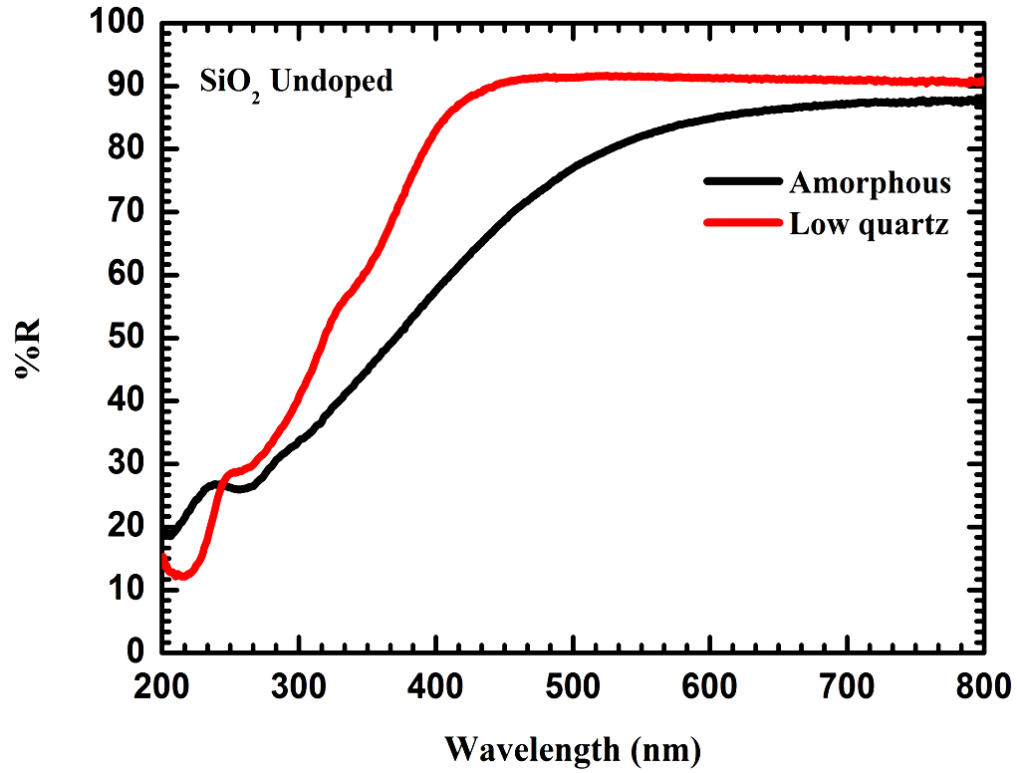

Figure 4-5 UV- Vis Diffuse reflectance spectra of low quartz and amorphous SiO_2 hosts

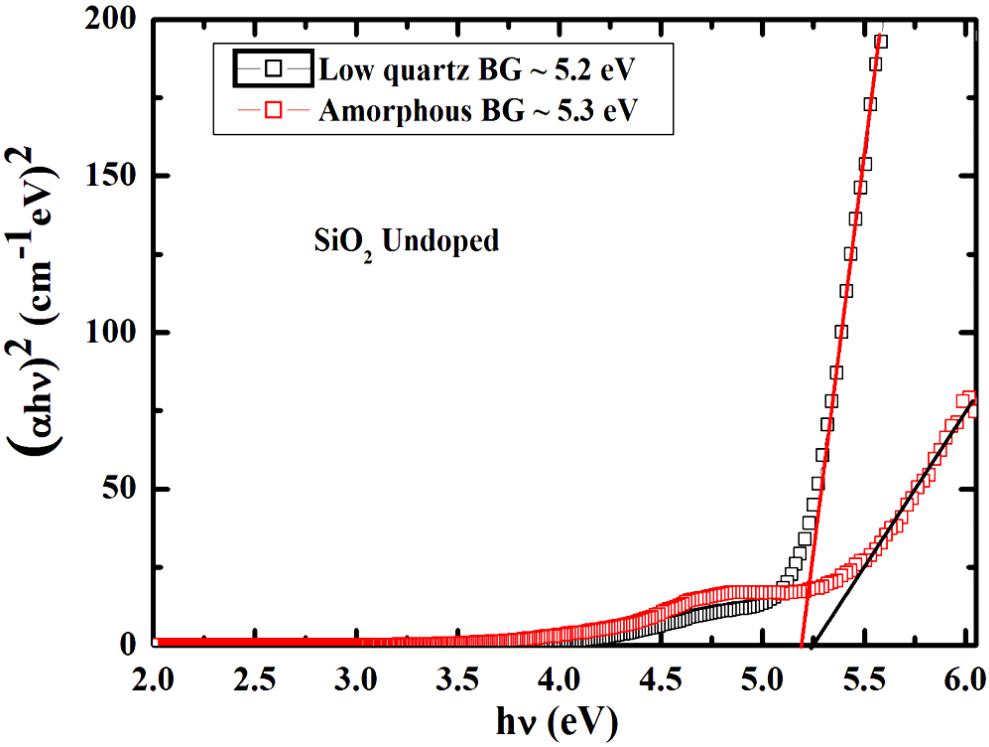

Figure 4-6 Transformed Kebelka-Munk reflectance versus band gap energy of low quartz and amorphous SiO_2

4.6 Conclusion

The phosphor powders from $ZnAl_2O_4$ and SiO_2 host lattices were successfully synthesized by a combustion method and sol-gel respectively. The XRD spectra for $ZnAl_2O_4$ powder samples confirm a highly crystalline face-centered cubic spinel $ZnAl_2O_4$ with a space group *Fd3m.* On the other hand, the XRD also can reveal the small traces of ZnO at 34.7º which appear as a secondary phase [26]. For SiO_2, the XRD exhibits a broad peak which can be attributed to amorphous phase at $2\theta \sim 23^{o}$. Although the other peak also came out as broad, there is a slight shift towards a lower diffraction angle and this suggests the evolution of crystallinity due to the nucleation through the formation of nuclei if the powder is produced via combustion. Hence, this behavior resembles the low quartz phase of silica. It is also noted that the presence of the uniform strain influences the location of the diffraction peak from the low quartz sample. The UV-VIS studies on $ZnAl_2O_4$ show that $ZnAl_2O_4$ absorbs more below a wavelength of 400 nm. Diffused reflectance on SiO_2 exhibits a shift of absorption towards lower wavelength in low quartz, which suggests the band gap tuning due to shrinkage effect.

4.7 References

[1] X. Duan, D. Yuan, X. Wang, H. Xu, *J. Sol–Gel Sci. Technol*. **35** (2005) 221-224.

[2] Z. Lou, J. Hao, *Appl. Phys*. **A 80** (2005) 151-154.

[3] S. Mathur, M. Veith, M. Haas, H. Shen, N. Lecerf, V. Huch, S. Hufner, R. Haberkon,H.P. Beck, M. Jilavi, *J. Am. Ceram. Soc*. **84** (9) (2001) 1921-1928.

[4] X. Wang, M. Zhang, H. Ding, H. Li, Z. Sun, *J. Alloys Compd*. **509** (2011) 6317-6320.

[5] F. Davar, M. Salvati-Niasari, *J. Alloys Compd*. **509** (2011) 2481-2492.

[6] M. Zawadzki, J. Wrzdyszcz, W. Strek, D. Hreniak, *J. Alloys Compd*. **332–324** (2001) 279 - 282.

[7] B.S. Barros, P.S. Mellow, R.H.G.A. Kiminami, A.C.F.M. Costa, G.F. de Sa, S. Alves Jr., *J. Mater. Sci.* **41** (2006) 4744 - 4748.

[8] I. Mindru, G. Marinescu, D. Gingasu, L. Patron, L. Diamandescu, C. Ghica, B. Mironov, *Mater. Sci. Eng*. **B 170** (2010) 99 - 106.

[9] H.H. Le, T.L. Phung, N.L. Nguyen, T.L. Trinh, *J. Phys: Conf. Ser*. **187** (2009) 012053 (1–6).

[10] S.S. Pitale, V. Kumar, I.M. Nagpure, O.M. Ntwaeaborwa, H.C. Swart, *Appl. Surf.Sci*. **257** (2011) 3298 - 3306.

[11] C.E. Chryssou, A.J. Kenyon and C.W. Pitt, *Mater. Sci. Eng.* **B 81** (2001) 16.

[12] M. Ferrari and C. Armellini, *J. Sol-Gel Sci. Technol* **19** (2000) 569.

[13] M. Morita, S. Kajiyama , T. Kai, D. Rau and T. Sakurai *J. Lumin*. **94** (2001) 91.

[14] M.A. Garcia, E. Borsella, S.E. Paje, J. Llopis, M.A. Villegas and R. Polloni, *J. Lumin*. **93** (2001) 253.

[15] K.C Patil, S.T Aruna, S. Ekambaram, *Current Opinion in Solid State & Mater.Sci **2*** (1997) 158.

[16] F. Booth, *Trans. Faraday Soc.* **49** (1953) 272.

[17] K.C Patil, S.T. Aruna, T. Miami, *Current Opinion in Solid State & Mater. Sci* **6** (2002) 507.

[18] N. Mngheddu,. P. Bertolino, C. Guilani, U. Zanotti, and U.A. Tamburini, *J. Appl. Phys.* **90** (2002) 594.

[19] K.C Patil, S.T. Aruna, T. Miami, *Current Opinion in Solid State & Mater. Sci* **6** (2002) 507.

[20] B.M. Mothudi, *PhD Thesis*, University of the Free State, South Africa (2009) 35.

[21] S.R. Jain, K.C. Adiga and V.R. Pai Verneker, *Combust. Flame* **40**, (1981) 71.

[22] D. Segal, *J. Mater*. **7** (1997) 1297-1305.

[23] I.M. Nagpure, Shreyas S. Pitale, K.G. Tshabalala, Vinay Kumar, O.M. Ntwaeaborwa, J.J. Terblans and H.C. Swart, *Materials Research Bulletin* **46** (2011) 2359-2366.

[24] M. Zawadzki, W. Staszak, F.E. López-Suárez, M.J. Illán-Gómez, A. Bueno-López, *Appl. Catal. A- Gen*. **371** (1-2) (2009) 92-98.

[25] M Yang, S Li and G Chen, *Applied Catalysis B: Environment* **101** (2011) 409-416

[26] Y.T. Prabhu, K.V. Rao, V.S.S. Kumar and B.S. Kumari, World Journal of Nano Science and Engineering, 4 (2014) 21−28.

[27] W. Lijuan, L. Anhuai, W. Changqiu, Z. Xishen, Z. Dongjun and L. Rui *J. Colloid Interface Sci.* **295 (**2006) 436

[28] U. Kalapathy, A. Proctor and J. Shultz, *Bioresour Technol.* **73 (**2000) 257

[29] A. Hernandez, I. Maya, E. Sanchez-Mora, E.M. Sanchez, *Jounal of Sol-Gel Science and Technology* **42** (2007) 71 – 78

[30] S. Sakthivel, S.U. Geissen, D.W. Bahnemann, V. Murugesan, A. Volgelpohl, *Journal of Photochemistry and Photobiology A- Chemistry* **148** (2002) 283- 293.

[31] P. Yu. Gnatenko, A.O. Borshch, N. Kukhatareva, T. Kukhatareva, I.O. Faryna and L.D. Paranchych, *J Applied Phys*. **94** (8) (2013), 4896-4901.

CHAPTER 5 LUMINESCENCE PROPERTIES AND X-RAY PHOTOELECTRON SPECTROSCOPY STUDY OF $ZnAl_2O_4$:Ce^{3+} ,Tb^{3+} PHOSPHOR

J. Alloy.Comp. 509 (2011) 10115-10120

5.1 Introduction

Zinc aluminate ($ZnAl_2O_4$) is a well-known semiconductor with a wide bulk band gap of 3.5-3.9 eV [1-6]. It belongs to a class of mixed-metal oxides called spinel and is commonly represented by a general chemical formula AB_2O_4 where A and B are divalent (2+) and trivalent (3+) cations respectively. In AB_2O_4 spinels unit cells, 8 of 64 tetrahedral interstices are occupied by A^{2+} cations while 16 of 32 octahedral interstices are occupied by B^{3+} cations [7]. It is well known that $ZnAl_2O_4$ can crystallize in a cubic normal or inverse spinel structure depending on the preparation procedure. In the normal spinel structure, the 3+ ions occupy the octahedral site while the 2+ ions occupy the tetrahedral site. In an inverse spinel the divalent and trivalent ions are not just exchanged, but there is a mixed occupation by different amounts of A^{2+} and B^{3+} on the octahedral site while the tetrahedral site is only occupied by the B^{3+} cations. In most cases, intermediate structures between normal and inverse spinels are crystallized [8]. Traditionally, $ZnAl_2O_4$ with normal, intermediate or inverse spinel structure is widely used as a catalyst or ceramic [9]. Today, it is used in many applications such as optoelectronics, sensor technology and information display technology [1,2,5,6] because of its excellent optical and hydrophobic properties and high chemical and thermal stability [10]. For application in display technologies, $ZnAl_2O_4$ is used as host matrix for trivalent rare-earth ions (e.g. Tb^{3+}, Eu^{3+} and Dy^{3+}) [11-13] or transition metals (e.g. Mn^{2+} and Cr^{3+}) [14-15] to prepare phosphors emitting mostly in the visible range of the electromagnetic spectrum. Researchers in this study are particularly interested in the performance of a nanocrystalline $ZnAl_2O_4$ because of the speculation that nanocrystalline materials may have better optical properties than their bulk counterparts [11]. Different

synthesis methods such as sol-gel [16-17], hydrothermal [18], combustion [6], [19, 20] and solid state reaction [21] are commonly used to prepare rare-earths/transition metals doped nanocrystalline $ZnAl_2O_4$ phosphors. In this chapter, the solution combustion method was used to prepare Ce^{3+}-Tb^{3+} co-activated nanocrystalline $ZnAl_2O_4$ phosphors. Compared to other methods, the combustion method has advantages such as cost-effectiveness, low processing temperature, extremely shorter reaction time, high purity and homogeneity of the final product. The flame temperature during urea assisted combustion was sufficient to enable some Al ions in the zinc aluminate spinel structure to occupy tetrahedral sites (spinel inversion) [22]. The objective of this chapter was to prepare an efficient green emitting phosphor through sensitization of Tb^{3+} by Ce^{3+}. It is well known that Ce^{3+} can absorb UV photons and sensitize emission of other rare-earths by a down-conversion process [23-24]. This chapter was also intended to investigate the effects of different parameters such as relatively low activator concentrations, annealing temperature and excitation wavelengths on emission efficiency of nanocrystalline $ZnAl_2O_4$:Ce,Tb phosphor. In addition, the X-ray photoelectron spectroscopy (XPS) was used to determine the chemical and electronic states of the elements present in as prepared and post-preparation annealed samples. This phosphor was evaluated for application in display technologies and also as a UV down-converting layer for improved efficiency of photovoltaic cells.

5.2 Experimental procedure

5.2.1 Powder preparation

The raw materials used were analytical reagent (AR) grade zinc nitrate hexahydrate, aluminium nitrate, rare-earth nitrates: (cerium nitrate and terbium nitrate), and urea (ACS reagent). All the chemicals were of AR grade from Merck South Africa with ~99% purity. The rare earth (Ce^{3+} and Tb^{3+}) nitrates were from Aldrich-Sigma with ~99.99 % purity. Stochiometric amounts of zinc nitrate, aluminium nitrate and urea were dissolved in triple de-

ionized (DI) water. A homogeneous transparent solution was obtained after stirring vigorously for 20 minutes. The solution was transferred to a muffle furnace maintained at 400 ±10°C. After all the liquid had evaporated, the mixture decomposed and released large amounts of gases. Due to the exothermic nature of this process, the reaction continued for a while and the mixture swelled to a larger volume. Large exothermicity resulted in a flame that further decomposed the mixture into gaseous phases and aluminates. The flame persisted for ~45 s. The entire combustion process was completed in less than 5 min. The powder products were gently ground using an alumina mortar and pestle and were then annealed at different temperatures either in air or hydrogen atmosphere to improve their crystallinity and optical properties. $ZnAl_2O_4:Ce^{3+},Tb^{3+}$ powder phosphors with different concentrations of Ce^{3+} and Tb^{3+} were prepared and investigated. The amounts of zinc nitrate, aluminium nitrate and urea used were 2.91 g, 7.57 g and 4.037g respectively. To avoid concentration quenching effects, the dopants (Ce^{3+} and Tb^{3+}) concentration was kept as low as reasonably achievable and the experiments were designed in such a way that the total doping concentration added up to ~2 mol%. For example, the typical concentrations of Ce and Tb ion pairs used were respectively 0.86 and 1.14 mol%, 1 and 1 mol% and 1.33 and 0.66 mol%.

5.2.2 Characterization

Room temperature X-ray diffraction (XRD) patterns were recorded from 10º to 75º (2θ) using a PANalytical X'Pert PRO diffractometer with wavelength radiation of 1.5406 Å (CuK_α). Luminescent properties were investigated at room temperature using Hitachi F−7000 fluorescence spectrophotometer. The decay data were recorded using an inverted-type scanning confocal microscope (MicroTime-200, Picoquant, Germany). A single-mode pulsed diode laser (375 nm wavelength with an instrumental response function of ~240 ps in full-width at half maximum, 40 MHz repetition rate, and an average power ~1 μW) was used

as an excitation source. The morphological and structural properties were investigated using FEI Tecnai F20G2 high-resolution transmission electron microscopy (HRTEM) with an accelerating voltage of 200 kV. The chemical composition was analyzed using a PHI 5000 *versa probe* X-ray photoelectron spectrometer (XPS). The XPS data were collected when the samples were irradiated with a monochromatic Al K_α radiation ($h\nu$ = 1486.6 eV). Survey scans were performed using a 1 eV/ step (binding energies ranging from 0 to 1400 eV). High resolution XPS peaks of individual elements were fitted using Multipack **v8.2c** data analysis software. The sample area analyzed was about 1 mm^2 and the pressure during data acquisition was typically under 1×10^{-8} Torr. The experimental curves were fitted using a *multipack v8.2c* data analysis software provided with the PHI-5000 versa-probe ESCA instrument that made use of a combination of Gaussian–Lorentzian lines.

5.3 Results and discussions

5.3.1 XRD analysis

The XRD patterns of pure/undoped and Ce^{3+}-Tb^{2+} co-activated $ZnAl_2O_4$ are respectively shown in Fig. 5.1 and 5.2. Undoped $ZnAl_2O_4$ samples in Fig. 5.1 were (a) as prepared and (b) annealed in air at 600^{o}C and (c) 700^{o}C for 4 hours, respectively. Figure 5.2 show the room temperature XRD patterns of the $ZnAl_2O_4$:Ce^{3+},Tb^{3+} samples annealed at 700^{o}C in a hydrogen atmosphere for 4 hours. The concentrations of Ce^{3+} and Tb^{3+} were (a) 1.33 mol%, 0.66 mol%; (b) 1.14 mol%, 0.86 mol%; (c) 1 mol%, 1 mol%; (d) 0.66 mol%, 1.33 mol%; and (e) 0.86 mol%, 1.14 mol%. The diffraction patterns of Fig. 5.1 and 5.2 confirmed that all the samples consisted of $ZnAl_2O_4$ spinel structure with space group *Fd3m* as indexed by JCPDS file No. 01-082-1043. All the peaks obtained are in agreement with the spinel structure reported by Zawadzki et al. [25]. The intensity of the peaks relative to the background signal demonstrates high crystallinity of the samples. The peak intensities and the FWHM values (not shown) of undoped $ZnAl_2O_4$ phosphors in Fig. 5.1 were

approximately the same regardless of annealing. It therefore shows that even without post-preparation annealing, highly crystalline material can be obtained at processing temperature as low as 400^{o}C. This result is different from conventional solid state reaction where high processing temperature (usually > 400^{o}C) is required to enhance crystallinity.

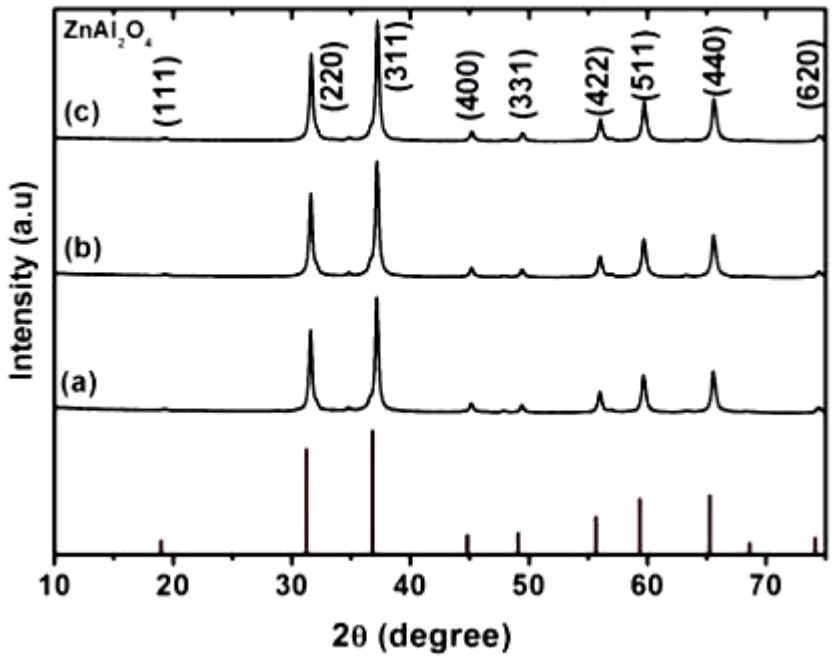

Figure 5-1 Room temperature XRD patterns of $ZnAl_2O_4$ (a), as-prepared (b), annealed at 600° C (c) and 700° C in air for 4 h.

Although the XRD patterns of Fig. 5.2 resemble those of Fig. 5.1, the peaks have broadened and their intensities were also reduced. It is well known that in addition to instrumental setup, the diffraction peak broadening is also a result of crystallite sizes and lattice strains. That is, large crystallite sizes cause sharp reflections whereas small sizes lead to broad reflections; and variations in lattice spacings due to lattice strains can also cause broadening [26]. Since the same procedure was used to prepare all samples in this study, the crystallites size of the samples with or without activators (Ce^{3+} and Tb^{3+}) must be in the same range. It is therefore reasonable to attribute the peak broadening of Fig. 5.2 to lattice strains due to incorporation of the Ce^{3+} and Tb^{3+} activator ions. Note that Ce^{3+} and Tb^{3+} are

expected to occupy Al^{3+} sites in the $ZnAl_2O_4$ lattice and since the ionic radii of Ce^{3+} (1.11Å) and Tb^{3+} (1.00 Å) are larger than that of Al^{3+} (0.50Å), their incorporation will most likely strain the lattice. In understanding that crystal imperfections and distortion of strain-induced peak broadening, it can be seen that Scherrer's relation follows a $1/\cos\theta$ dependency but not $\tan\theta$ as indicated from Williamson-Hall method. Moreover, the basic difference is that the small crystallite size is caused by microstrutural and the occurrence of the microstrain from the reflection broadening. Thus, it is clear that from W-H, a given sample $ZnAl_2O_4$:Ce,Tb with different concentrations of Ce and Tb may result in different values for lattice strain and crystallite size as shown in Table 5-1. In Fig. 5.3 it can also be seen that by incorporating more of Ce-content into $ZnAl_2O_4$ there is slight increase in strain as indicated by a dotted horizontal line. However, if the Ce-content is fixed and Tb is varied as shown in Fig. 5.4 the strain is minimal as discussed earlier due to the difference in ion radii between Ce and Tb ions. The unidentified XRD peak at 34.6° may be attributed to species/impurities such as aluminium oxides, hydroxides and oxyhydroxides in the tetrahedral environment.

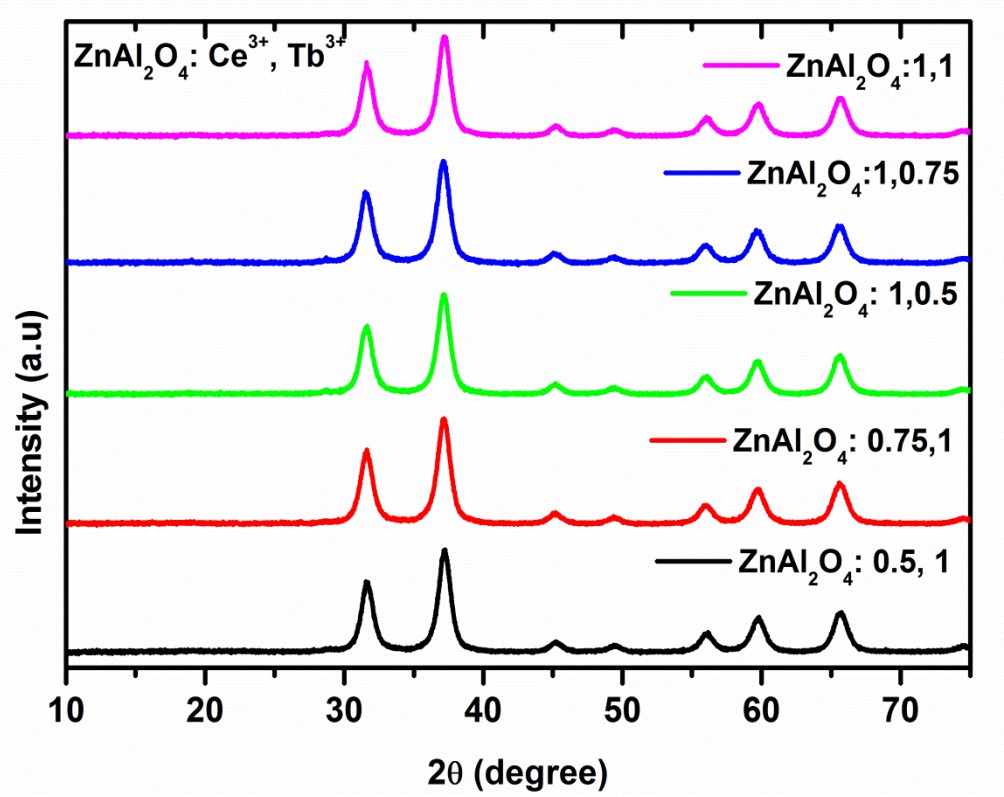

Figure 5-2 Room temperature XRD patterns of annealed $ZnAl_2O_4:Ce^{3+}$, Tb^{3+} with different concentrations of Ce^{3+} and Tb^{3+}

Table 5-1 Geometric parameters of the $ZnAl_2O_4$:Ce,Tb nanoparticles

$ZnAl_2O_4$:Ce, Tb	$\langle t \rangle$ crystallite size (nm)	ε Strain %
0.5%Ce, 1%Tb	8.92	4.34
0.75%Ce, 1%Tb	8.72	4.41
1%Ce, 1%Tb	8.74	4.43
1%Ce, 0.5%Tb	8.97	4.31
1%Ce, 0.75%Tb	9.10	4.25

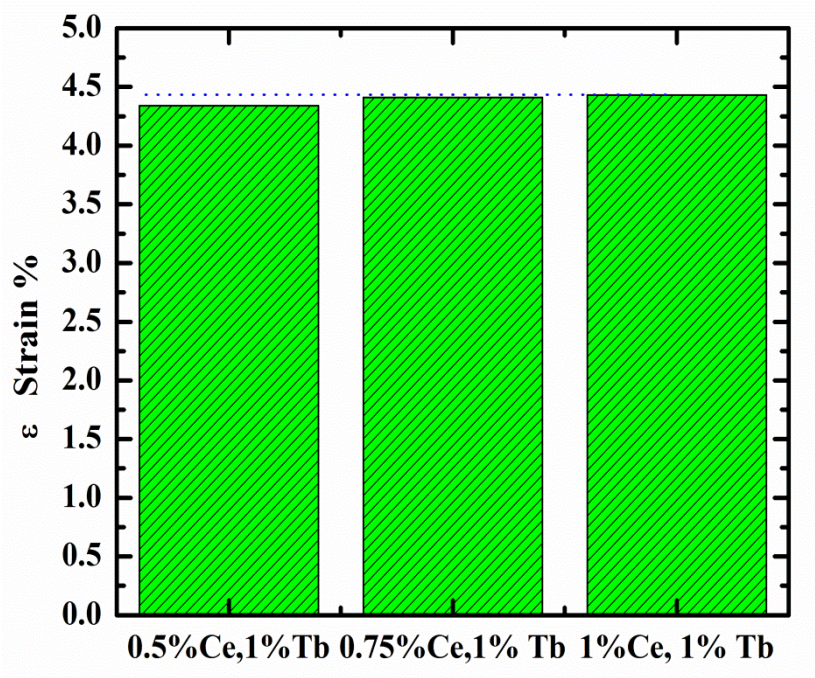

Figure 5-3 The strain as a function of $ZnAl_2O_4$:Ce, Tb where Ce-content is varied while that of Tb is capped fixed

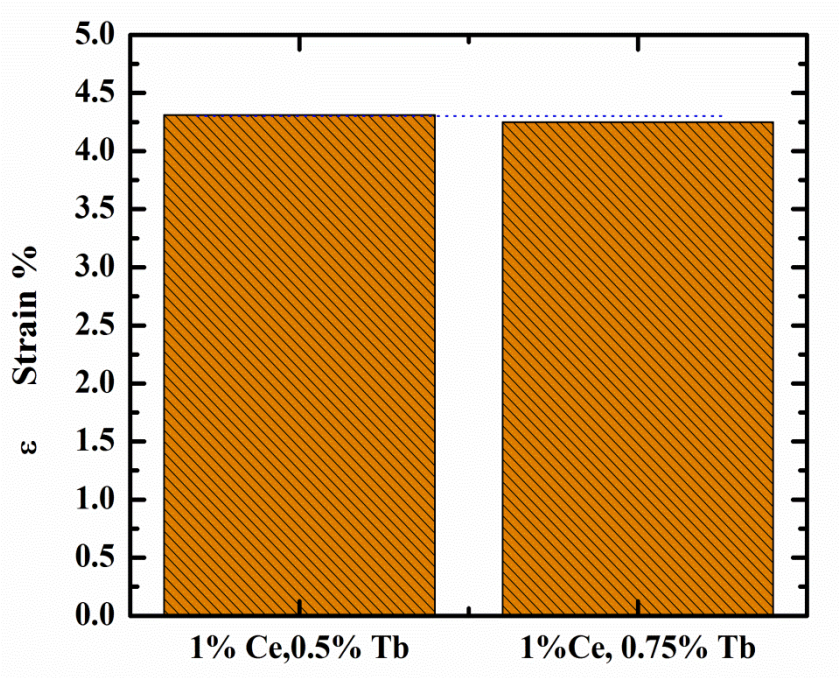

Figure 5-4 The strain as a function of $ZnAl_2O_4$:Ce, Tb where Ce-content is fixed while that of Tb is varied

5.3.2 TEM analysis

Transmission electron microscope (TEM) images of pure $ZnAl_2O_4$ and $ZnAl_2O_4:Ce^{3+},Tb^{3+}$ powder annealed in the hydrogen atmosphere are shown in Fig. 5.5. The concentrations of Ce^{3+} and Tb^{3+} were 0.86 and 1.14 mol% respectively. Fig. 5.5 (a) and (c) shows agglomerated $ZnAl_2O_4$ and $ZnAl_2O_4:Ce^{3+},Tb^{3+}$ particles with individual particles appearing circular (implying spherical shapes, although some faceting exists) with an average diameter of ~20 nm. High resolution TEM (HRTEM) image in Fig. 5.5 (b) and (d) show well defined lattice fringes in various regions with agglomerated particles. As shown by lattice fringes in the images (Fig. 5.5 (b) and (d)), this sample is highly crystalline and is consistent with the XRD data. The lattice spacing estimated from the selected area diffraction pattern (inset- Fig.5.5(d)) was 0.24 nm, corresponding to the (311) lattice spacing of $ZnAl_2O_4$ [27].

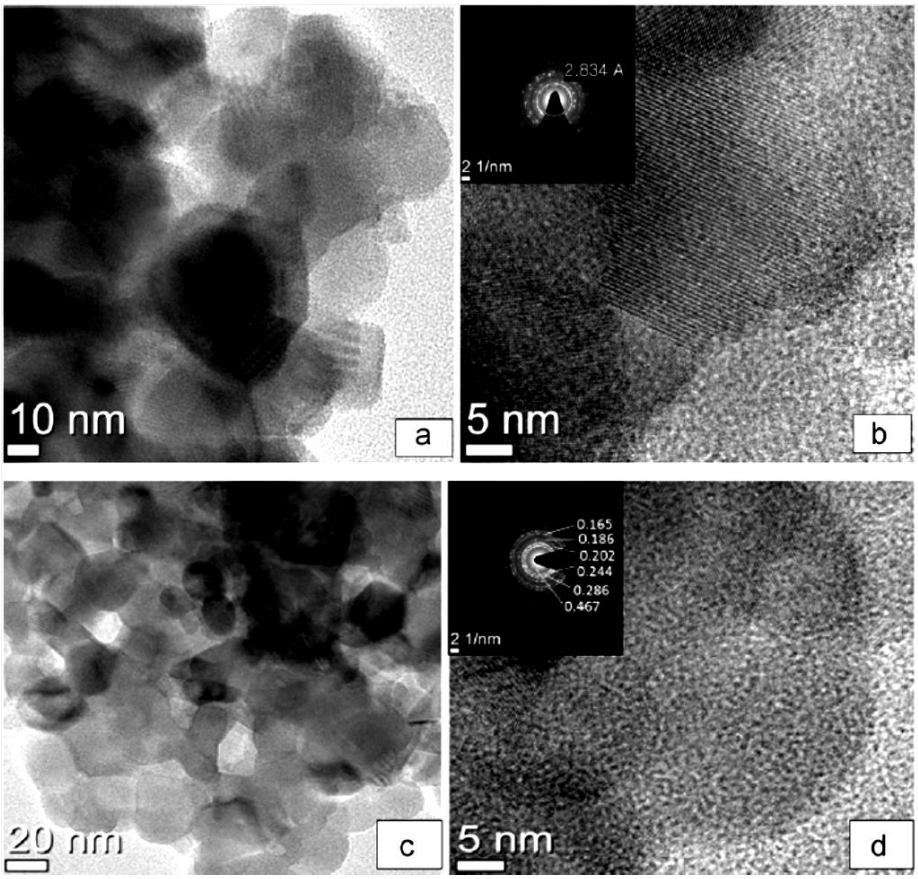

Figure 5-5 (a) TEM image of $ZnAl_2O_4$:0.86 mol% Ce^{3+} - 1.14 mol% Tb^{3+} showing agglomerated particles and (b) an enlarged view of the same sample showing fringes corresponding to the atomic planes. The inset is the selected area diffraction patterns of the sample.

5.3.3 Photoluminescence

Photoluminescence emission spectra of $ZnAl_2O_4$:Ce^{3+}, Tb^{3+} nano-powder phosphors and that of Ce^{3+} (2 mol%) singly doped $ZnAl_2O_4$ are presented in Fig. 5.6. The $ZnAl_2O_4$:Ce^{3+}, Tb^{3+} nanopowders with different concentrations of Ce^{3+} and Tb^{3+} were excited in air at room temperature using different excitation wavelengths. The emission spectrum of Ce^{3+} singly doped $ZnAl_2O_4$ phosphor excited at 256 nm consists of a broad band with two maxima at 350 and 410 nm. These emissions correspond to the allowed transitions from the lowest sublevel of the 5d state to the $^2F_{7/2}$ and $^2F_{5/2}$ multiplets of the 4f configuration in Ce^{3+} [28].

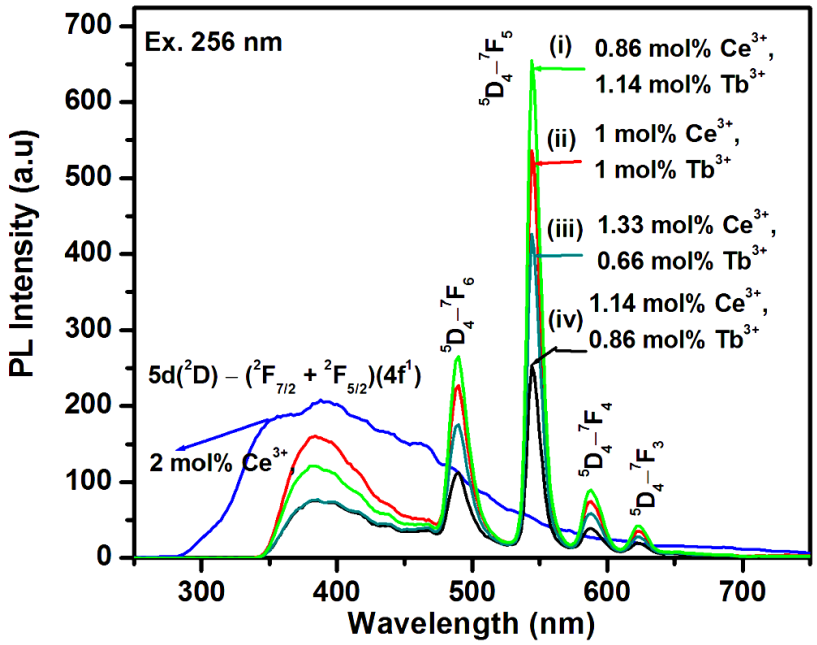

Figure 5-6 PL emission spectra of annealed $ZnAl_2O_4$: Ce^{3+}, Tb^{3+} with different concentrations of Ce^{3+} and Tb^{3+}

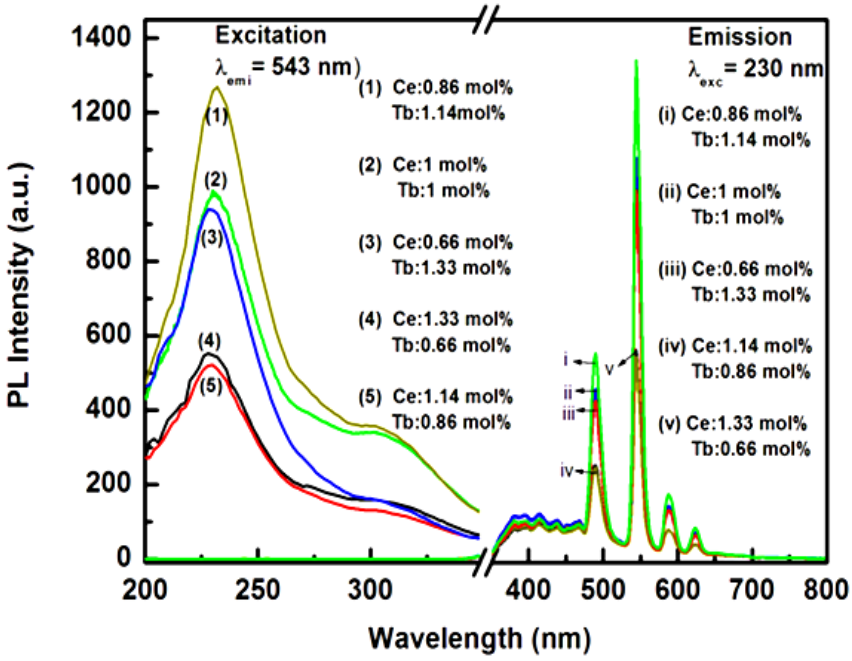

Figure 5-7 PL and PLE spectra of $ZnAl_2O_4$:Ce^{3+}, Tb^{3+} excited at 230 nm.

Dual emission was observed from the $ZnAl_2O_4$ powders co-activated with different concentrations of Ce^{3+} and Tb^{3+}. This was a combination of line emissions from Tb^{3+} ions and broad emission from Ce^{3+}. The green line emission associated with $^5D_4 \rightarrow {}^7F_5$ transitions of Tb^{3+} at 544 nm was more intense than the purplish-blue broad emission of Ce^{3+} at 350-410

nm. The green emission was maximized when 1.14 mol% of Tb^{3+} was co-doped with 0.86 mol % of Ce^{3+}. The enhancement of the green emission and the subsequent decrease in the blue emission suggests that energy was transferred, most probably by phonon mediated processes, from Ce^{3+} to Tb^{3+}. This transfer of energy is a well established phenomenon found in several host matrices. For example, energy transfer from Ce^{3+} to Tb^{3+} was demonstrated in amorphous SiO_2 host [29]. It is demonstrated in this study that in addition to energy transfer through direct excitation of Ce^{3+}, the emission intensity is also dependent on the excitation wavelength. For example, from the list of selected excitation wavelengths (230 – 325 nm), the most intense excitation was observed at 230 nm and it gave green emission (λ_{em} = 544 nm) in all the samples. The excitation at 230 nm is consistent with the 232 nm excitation attributed to the $4f^8 \rightarrow 4f^85d^1$ transitions of Tb^{3+} by Barros et al. [11].

Figure 5.7 shows the PL excitation (λ_{exc} = 230 nm) and emission (λ_{em} = 544 nm) of $ZnAl_2O_4$ powders with different concentrations of Ce^{3+} and Tb^{3+}. The most intense green emission was observed from the powder co-doped with 1.14 mol% of Tb^{3+} and 0.86 mol% of Ce^{3+}. The maximum intensity as a function of excitation wavelength of 1.14 mol% of Tb^{3+} and 0.86 mol% of Ce^{3+} co-doping shown in Fig. 5.8 confirms that the 230 nm excitation gave the most intense green emission at λ_{em} = 544 nm. The other excitation wavelengths (256, 300 and 325 nm) with relatively less intense emissions can be attributed to either direct excitation of Ce^{3+} or charge transfer transition from O^{2-} to Tb^{3+}.

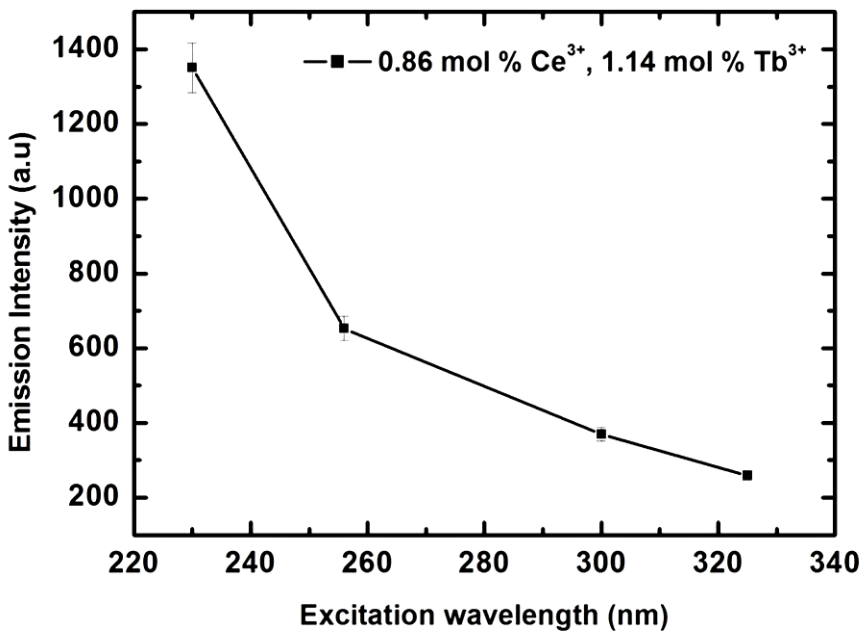

Figure 5-8 Maximum emission intensity of $ZnAl_2O_4$: 0.86 mol% Ce^{3+}, 1.14 mol% Tb^{3+} (λem = 544 nm) as a function of excitation wavelengths (230, 256, 300 and 325 nm).

5.3.4 Decay dynamics of Ce^{3+} singly doped and Ce^{3+} −Tb^{3+} co-doped $ZnAl_2O_4$

Figure 5.9 compares the fluorescence decay dynamics of singly activated and $ZnAl_2O_4$:Ce^{3+} (2 mol%) and $ZnAl_2O_4$:Ce^{3+},Tb^{3+} (0.86 mol%, 1.14 mol%) powders, which gave the maximum PL intensity. The powders were excited at 375 nm monitoring Ce^{3+} emission at 410 nm. A single-mode pulsed diode laser wavelength with an instrumental reponse function of ~240 ps in full-width at half maximum, 40 MHz repetition rate, and an average power of ~1 μW was used. The decay curves were fitted using the bi-exponential function:

$$I = A_1 \exp(-t_1/\tau_1) + A_2 \exp(-t_2/\tau_2), \quad (5.1)$$

where I represents the phosphorescent intensity; A_1 and A_2 are constants; t_1 and t_2 are the decay times and τ_1 and τ_2 are the decay constants. The fitting parameters are presented in table 5.2. The average lifetimes were calculated using the following equation:

$$(\tau) = \frac{A_1\tau_1^2 + A_2\tau_2^2}{A_1\tau_1 + A_2\tau_2} \tag{5.2}$$

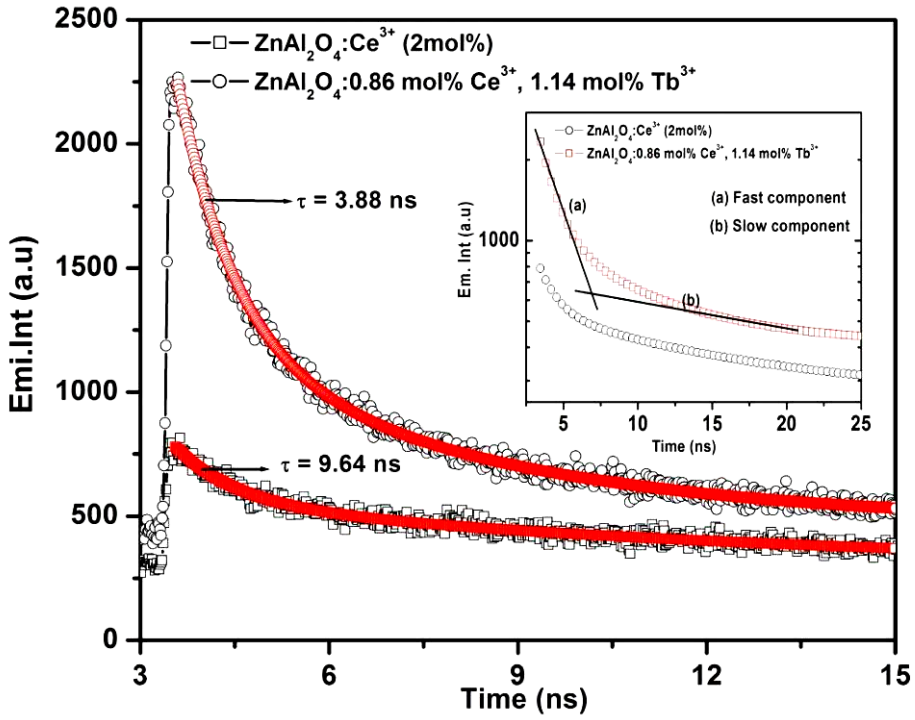

Figure 5-9 Decay curves of the $ZnAl_2O_4:Ce^{3+}$ (2 mol%) and $ZnAl_2O_4$:0.86 mol% Ce^{3+}, 1.14 mol% Tb^{3+} measured in air at room temperature.

The lifetime values for the Ce^{3+} singly activated and Ce^{3+}-Tb^{3+} co-activated $ZnAl_2O_4$ samples were 9.62 and 3.88 ns respectively. The fact that the average lifetime of the Ce^{3+}-Tb^{3+} co-activated sample was shorter than the Ce^{3+} singly activated sample indicates that the decay rate of the 410 nm emission was faster in the co-activated sample. Since the decrease in the peak intensity of the 410 nm emission was simultaneous with the increase in the peak intensity of Tb^{3+} emission at 544 nm, it is reasonable to attribute the shorter life time (faster decay rate) of this emission to energy transfer from Ce^{3+} to Tb^{3+}. The simultaneous radiative emission and energy transfer from Ce^{3+} to Tb^{3+} suggests that Ce^{3+} is capable of creating a potential well for trapping charge carriers, thereby playing a dual role of a luminescent and trap centre [30-31]. The inset of Fig. 5.9 shows that the bi-exponential decay curves can be resolved into two components, namely: the fast and slow components with decay times of

0.911 ns and 4.736 ns respectively. Birowosuto et al. [30] attributed the slow and fast components to exciton trapping by Ce^{3+} and lattice (and subsequent transfer to Ce^{3+}) respectively. The fitting parameters for $ZnAl_2O_4$:Ce^{3+} (2 mol%) and $ZnAl_2O_4$:0.86 mol% Ce^{3+}, 1.14 mol% Tb^{3+} samples are listed in table 5.2.

Table 5-2 Fitting parameters for the half life times of $ZnAl_2O_4$:Ce^{3+} and $ZnAl_2O_4$:Ce^{3+}, Tb^{3+}

Sample name	**Fitting parameters**			
	A_1	τ_1 (ns)	A_2	τ_2 (ns)
$ZnAl_2O_4$:Ce^{3+}	225.54	0.968	275.22	10.31
$ZnAl_2O_4$:Ce^{3+},Tb^{3+}	1101.34	0.911	736.15	4.736

5.3.5 X-ray photoelectron spectroscopy (XPS)

The chemical composition and electronic state of the $ZnAl_2O_4$:Ce^{3+}, Tb^{3+} system were analysed by X-ray photoelectron spectroscopy (XPS). The XPS survey spectrum in Fig. 5.10 confirms the presence of Al 2*p*, O 1*s*, Zn $2p_{3/2}$ and C 1*s* (from adventitious hydrocarbons) with binding energies (BE) of 74.2 eV, 531.1 eV, 1022.1 eV and 285.3 eV, respectively on the surface. These values are consistent with those reported by Strohmeier [32].

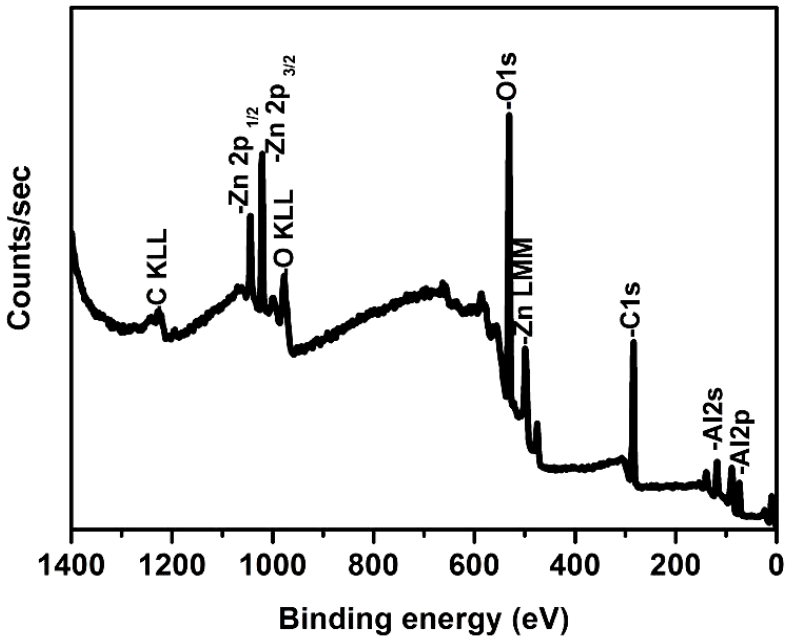

Figure 5-10 X-ray photoelectron spectroscopy (XPS) survey scan of $ZnAl_2O_4$:Ce^{3+}, Tb^{3+} phosphor

Figure 5.11 and 5.12 show respectively the fitted data for the O1*s* peak from $ZnAl_2O_4$:0.86 mol% Ce^{3+}, 1.14 mol% Tb^{3+} powder before and after annealing. In both figures, the lattice O1*s* peak was stable at ~531.1 eV suggesting that the chemical and hence electronic states were not affected by annealing in hydrogen. This peak is consistent with the O1*s* peak with the binding energy of 531.4 eV reported by Strolmeier [32]. The satellite peaks at ~528.5 eV and ~529.5 eV in Fig. 5.9 and 5.10 can be assigned to binding energies of O1*s* peak in Ce-O and Tb-O metallic oxides respectively [33]. That is, it is most likely that small traces of CeO_x and TbO_x ($x \leq 2$) were present in both annealed and unannealed $ZnAl_2O_4$:Ce^{3+},Tb^{3+} samples. It is worth noting that these peaks were really small and in the noise levels of our measurements. Fig. 5.12 shows the XPS fittings of the O1*s* peak from the sample annealed in hydrogen atmosphere. Again in Fig. 5.12, the photoelectron peak position measured at 531.3eV is consistent with the theoretical value of O1*s* peak in $ZnAl_2O_4$

listed in ref. [32]. In addition, a new band appeared at 532.6 eV and it can be assigned to chemisorbed water and/or oxygen molecules from environmental moisture [34].

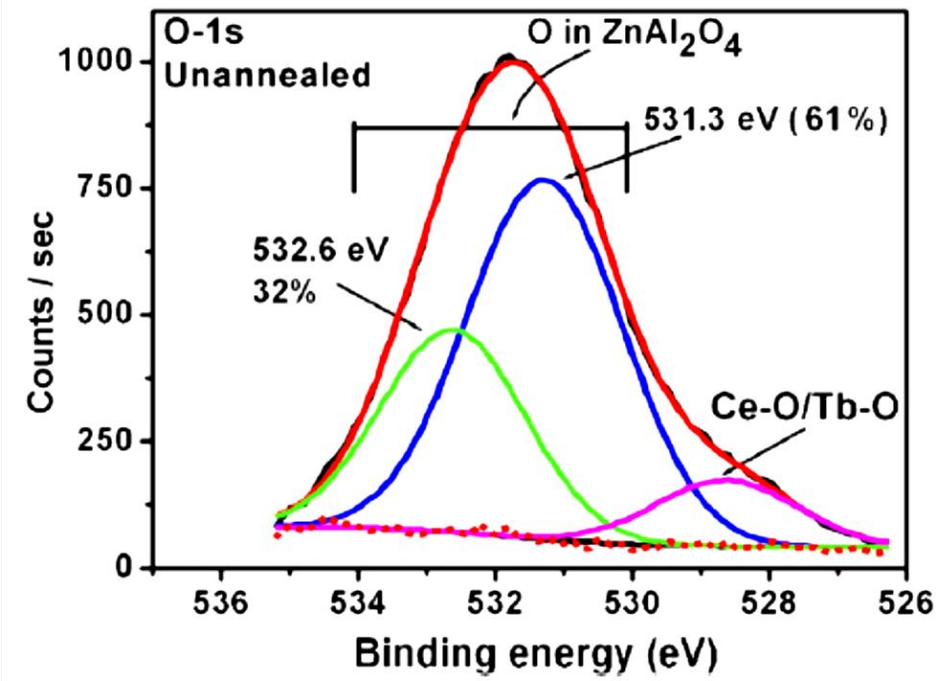

Figure 5-11 XPS peak fitting of the O 1s peak from as-prepared $ZnAl_2O_4$:0.86% Ce^{3+}, 1.14% Tb^{3+}.

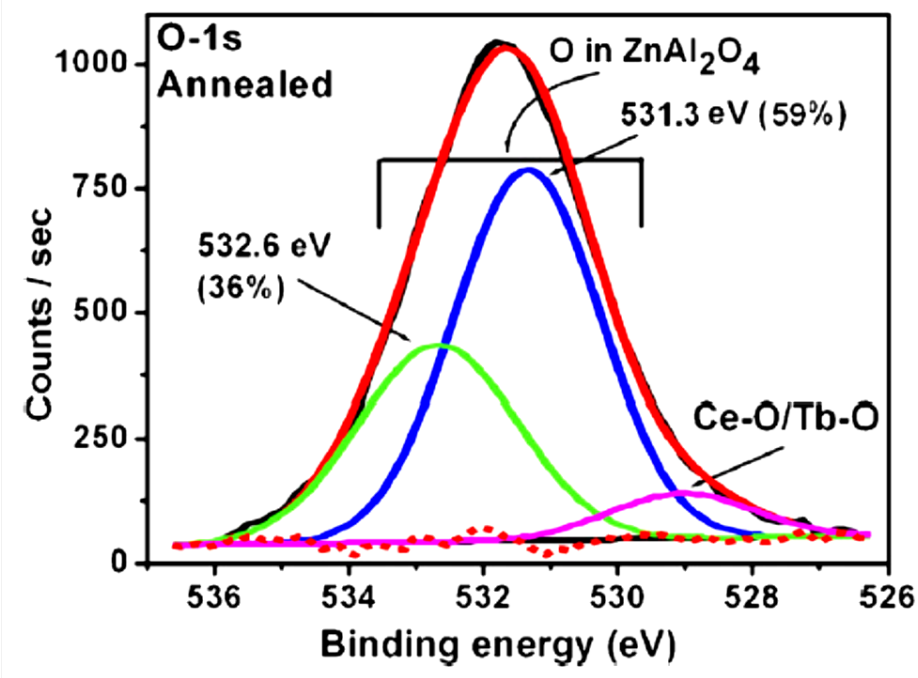

Figure 5-12 XPS peak fitting of the O 1s peak after annealing $ZnAl_2O_4$:0.86% Ce^{3+}, 1.14% Tb^{3+} in hydrogen atmosphere.

The fitted data of the Al 2*p* peak of the $ZnAl_2O_4$:0.86 mol% Ce^{3+}, 1.14 mol% Tb^{3+} before and after annealing are shown respectively in Fig. 5.13 and 5.14. In both figures, the Al 2*p* peaks at lower binding energies (74.2 eV) can be assigned to Al ions occupying the tetrahedral (IV) sites while the Al 2*p* peaks at higher binding energies (75.6 eV) can be assigned to the Al ions occupying the octahedral (VI) sites. This assignment is consistent with the Al 2*p* yttrium aluminium garnet, $Y_3Al_5O_{12}$ (YAG), reported by Pawlak et al. [34]. Furthermore, they reported the peak area ratio of the Al 2*p* in the octahedral to tetrahedral sites of 2:3 (40%:60%).

Note that it is generally accepted that when a material consists of a mixture of octahedrally and tetrahedrally bonded oxides, the octahedral site is more cationic with a partial positive charge $(\delta+)$ and the tetrahedral site will be more anionic with a partial negative charge $(\delta-)$ [34]. It is therefore reasonable to assign the tetrahedral site with less binding energy because less energy is required to take out an electron from more anionic species. The concentrations of Al in the octahedral and tetrahedral sites of the unannealed sample (Fig. 5.13) as determined from the area of the fitted Al peaks were 36% and 64% respectively. Recall that the high concentration of 3+ ions (Al^{3+}) in the tetrahedral site with respect to that in the octahedral site points to the partial inversion of the $ZnAl_2O_4$ nanocrystal structure. Upon annealing, the concentration of Al in the octahedral site increased from 36% to 40%, while that in the tetrahedral site decreased from 64 to 60% as shown in Fig. 5.14. This can be attributed to possible structural readjustment from inverse to normal spinel as a result of annealing. There is, however, no physically possible way in a spinel structure for being more than 50% of the trivalent ions on the tetrahedral site as in this case. It must, however, be pointed out that XPS is a surface sensitive technique, with the XPS signal coming from the top few layers which might be slightly different from the bulk. Extra contributions from possible surface species/impurities such as aluminium oxides, hydroxides

and oxyhydroxides with binding energies around 73.7 eV might contribute toward the excess amount of Al in the tetrahedral sites.

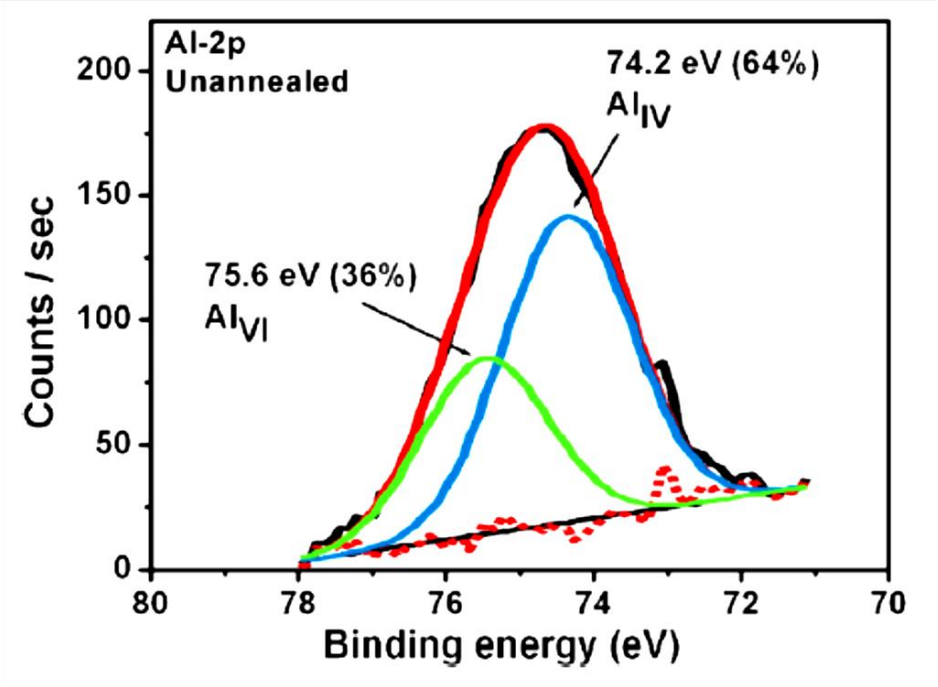

Figure 5-13 XPS peak fitting of the Al 2p peak from as-prepared $ZnAl_2O_4$:0.86% Ce^{3+}, 1.14% Tb^{3+}

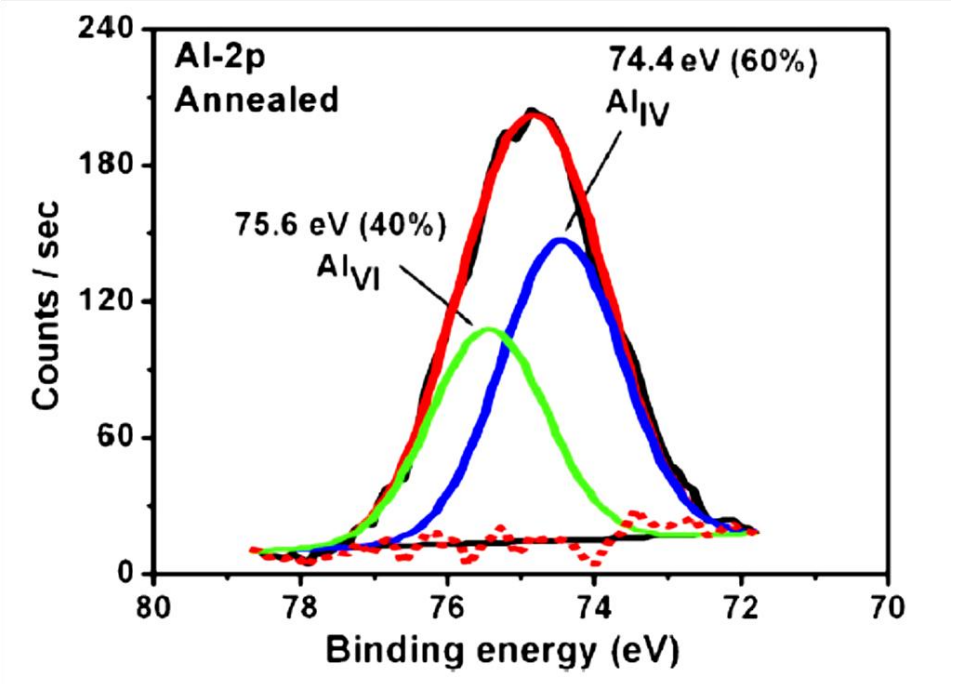

Figure 5-14 XPS peak fitting of the Al 2p peak from as-prepared $ZnAl_2O_4$:0.86% Ce^{3+}, 1.14% Tb^{3+}

5.4 Conclusion

In conclusion, the $ZnAl_2O_4$: Ce^{3+}, Tb^{3+} powder phosphors were successfully synthesized using a one-step combustion technique. As confirmed from the X-ray diffraction data, $ZnAl_2O_4$ was highly crystalline with or without post-synthesis annealing. The X-ray photoelectron spectroscopy data confirmed that there was structural readjustment from inverse to normal spinel as a result of annealing. The TEM data showed that the particles were spherical in shape, with some degree of faceting, and their average size was ~20 nm in diameter. The PL intensity of the green line emission from Tb^{3+} at 544 nm increased as a result of Ce^{3+} co-doping. The fact that the increase was simultaneous with the decrease in blue emission from Ce^{3+} suggests that excitation energy was transferred from Ce^{3+} to Tb^{3+}. The maximum intensity was obtained from the sample co-activated with 0.86 mol% of Ce^{3+} and 1.14 mol% of Tb^{3+} when the sample was excited at 230 nm. The other excitation wavelengths (256, 300 and 325 nm) with relatively less intense emissions were attributed to either direct excitation of Ce^{3+} or charge transfer transition from O^{2-} to Tb^{3+}. It therefore shows that the activator concentration and excitation wavelength are important parameters for sensitized emission of phosphors by the UV down-conversion process.

5.5 References

[1] Z. Lou and J. Hao, *Appl. Phys*. **A 80** (2005) 151-154.

[2] S. Mathur, M. Veith, M. Haas, H. Shen, N. Lecerf, V. Huch**,** S. Hufner, R Haberkon, H.P. Beck and M. Jilavi, *J. Am. Ceram. Soc*. **84 (9)** (2001) 1921- 1928.

[3] R.F. Martinez and O.A. Serra, J. Braz. *Chem. Soc.* **21 (7)** (2010) 1395-1398.

[4] V. Ciupina, I Garazeanu and G. Prodan, *J. Opt. Adv. Mater*. **6 (4)** (2004) 1317-1322.

[5] X. Wang, M. Zhang, H. Ding, H. Li and Z. Sun, *J. Alloys. Compd*. **509** (2011) 6317-6320

[6] F. Davar, M. Salvati-Niasari, *J. Alloys. Compd*. **509** (2011) 2481-2492

[7] J. Popović, B. Gržeta, B. Rakvin, E. Tkalčec, M. Vrankić and S. Kuranjica, *J. Alloys. Compd.* **509** (2011) 8487-8492

[8] J. Zhao, H. Chai and F. Zhang, *JMEPEG*. **19** (2010) 46-51

[9] X. Duan, D. Yuan, X. Wang and H. Xu, *J. Sol-gel Sci. Technol*. **35** (2005) 221-224.

[10] M. Zawadzki, J. Wrzdyszcz, W. Strek and D. Hreniak, *J. Alloys. Compd*. **332-324** (2001) 279 -282.

[11] B.S. Barros, P.S. Mellow, R.H.G.A. Kiminami, A.C.F.M. Costa, G.F. de Sá and S. Alves Jnr, *J. Mater. Sci*. **41** (2006) 4744-4748.

[12] S.F. Wang, F. Gu, M.K. Lu, X.F. Cheng, W.G. Zhou, G.J. Zhou, S.M. Wang and Y.Y. Zhou, *J. Alloys. Compd*. **394** (2005) 255-258.

[13] I. Mindru, G. Marinescu,D. Gingasu, L. Patron, L. Diamandescu, C. Ghica and B. Mironov, *Mat. Sci. Eng*. **B. 170** (2010) 99-106.

[14] H.H. Le, T.L. Phung, N.L. Nguyen and Trinh T.L., *J. Phys:Conference Series*. **187** (2009) 012053 (1-6).

[15] S.S. Pitale, V. Kumar, I.M. Nagpure, O.M. Ntwaeaborwa and H.C. Swart, *Appl. Surf. Sci*. **257** (2011) 3298-3306.

[16] Y. Wu, J. Du, K.-L. Choy, L.L. Hench, J. Guo, *Thin Solid Films*, **472** (1-2) (2005) 150-156.

[17] M.-T. Tsai, Y.-X. Chen, P.-J. Tsai, Y.-K. Wang, *Thin Solid Films*. **518** (24) (2010) e9-e11.

[18] C.-C. Yang, S.-Y. Chen, S.-Y. Cheng, *Powder Technol*. **148 (1)** (2004) 3-6.

[19] X.Y. Chen and C. Ma, *Opt. Mater*. **32** (2010) 415-421

[20] V. Singh, V. Natarajan, Jun-Jie Zhu, *Opt. Mater*. **29** (2007) 1447–1451.

[21] N. J. van der Laag, M. D. Snel, P. C. M. M. Magusin, G. de With, *J. Eur. Ceram Soc*. **24 (8)** (2004) 2417-2424

[22] T. Mimani, *J. Alloys. Compd*. **315** (2001) 123.

[23] P. Thiyagarajan, M. Kottaisamy, M.S. Ramachandra Rao, *J. Lumin*. **129 (9)** (2009) 991-995.

[24] Q.Y. Zhang, X.Y. Huang, *Prog. Mater. Sci*. **55 (5)** (2010) 353-427.

[25] M. Zawadzki, W. Staszak, F.E. López-Suárez, M.J. Illán-Gómez, A. Bueno-López, *Appl. Catal. A- Gen*. **371 (1-2)** (2009) 92-98

[26] J.-D. Kaminga and L.J. Seijbel, *J. Res. Inst. Stand. Technol*. **109** (2004) 64-75.

[27] O.M. Ntwaeaborwa, H.C. Swart, R.E. Kroon, P.H. Holloway and J.R. Botha, *J. Phys. Chem. Sol*. **67** (2006) 1749-1753

[28] A.A. da Silva, A.S. Goncalves, M.R. Davolos, and S.H. Santagneli, *J. Nanosci. Nanotechnol.* **8** (2008) 5691.

[29] V.R Bandi, Y.T. Nien and I.G. Chen, *J. Appl. Phys*. **108** (2010) 02311-2

[30] M.D. Birowosuto, P. Dorenbos, C.W.E van Eijk, K.W. Krämer and H.U. Güdel, *Phys. Stat. Sol.* **(a) 204 (3)** (2007) 850 - 860.

[31] E.V.D. van Loef, P. Dorenbos, C.W.E van Eijk, K.W. Krämer and H.U. Güdel, *Nucl. Instr. Meth. Phys. Res*. **A. 496** (2003) 138 - 145.

[32] B. R. Strohmeier, *Surf. Sci. Spec*. **3** (1995) 129-134.

[33] J.F. Moulder, W.F. Stickle, P.E. Sobol and K.D. Bomben, *Handbook of X-ray Photoelectron Spectroscopy*, Physical Electronic, Inc. Minnnesota (USA), (1995).

[34] S.J. Kerber, J.J. Bruckner, K Wozniak, S. Seal, S Hardcastle and T.L. Barr, *J. Vac. Sci. Technol*. **A. 14 (3)** (1996) 1314-1320. D.A. Pawlak, K Wozniak, Z Frukacz, T.L. Barr, D. Fiorentino and S. Seal, *J. Phys. Chem*. **B. 103** (1999) 1454 – 1461.

CHAPTER 6 LUMINESCENCE PROPERTIES OF Ce^{3+} and Tb^{3+} CO -ACTIVATED $ZnAl_2O_4$ PHOSPHOR

Phys. B; Condens. Matter. 407 (2012) 1489-1492

6.1 Introduction

Zinc alluminate ($ZnAl_2O_4$) is one of the metal oxides which are currently being investigated as possible hosts for rare-earth ions to prepare light emitting materials (phosphors) that can be used in different types of light emitting devices. Traditionally, $ZnAl_2O_4$ is widely used as a catalyst or ceramic [1]. Because of its excellent optical properties, high chemical and thermal stability, it is also used in optoelectronic devices, [2,3]. In addition, it has been demonstrated that pure (undoped) and impurities-activated (-doped) $ZnAl_2O_4$ produce efficient emissions that can be used in lighting. Emission from pure $ZnAl_2O_4$ is characterized by two broad bands with maxima at ~450 and ~770 nm, which are respectively ascribed to $Al^{3+} \rightarrow O^{2-}$ charge transfer and anionic oxygen vacancies (V_O) [4], while the impurities-activated $ZnAl_2O_4$ emission is due to the intrinsic nature of the incorporated impurity. Today; orange, green and red emissions have respectively been observed from Mn^{2+}, Tb^{3+} and Eu^{3+} ions incorporated in $ZnAl_2O_4$ host [5-7].

In this chapter, Ce^{3+} and Tb^{3+} ions were simultaneously incorporated with different concentrations in $ZnAl_2O_4$ resulting in a green emitting phosphor that was evaluated for possible applications in, among other things, photovoltaic cells and display technologies. We demonstrated that upon excitation by UV radiation, the UV photons were absorbed and transferred from Ce^{3+} to Tb^{3+} by a down conversion process. The down conversion process involves absorption of UV photons in the short wavelength range (typically ~200 – 350 nm) and emission of visible photons in the wavelength range of ~400-700 nm. Today, rare-earths doped phosphors are extensively investigated for possible application as down-converting layers to improve the absorption efficiency of the silicon (Si) photovoltaic (PV) cells [8].

That is, by shifting the sunlight wavelengths from the UV region where the spectral response of the Si PV cells is low to the visible region where the spectral response is high. In this study, the down-conversion process between Ce^{3+} and Tb^{3+} in $ZnAl_2O_4$ was investigated. The possible down-conversion mechanism through energy transfer from Ce^{3+} to Tb^{3+} is discussed. In addition cathodoluminescence intensity of the $ZnAl_2O_4:Ce^{3+},Tb^{3+}$ phosphors was also investigated for its possible application as a green emitting phosphor in low voltage field emitting displays (FEDs). These phosphors were prepared by the solution combustion method.

6.2 Experimental procedure

A detailed procedure about the combustion reaction synthesis of impurities-activated $ZnAl_2O_4$ can be found in refs. [5,7,9]. In a typical synthesis, stochiometric amounts of zinc nitrate, aluminium nitrate, cerium nitrate, terbium nitrate and urea were dissolved in de-ionized water. A homogeneous transparent solution was obtained after stirring vigorously for 20 minutes. The solution was transferred to a muffle furnace maintained at 400 ±10°C. After all the liquid had evaporated, the mixture decomposed and released large amounts of gases. Due to the exothermic nature of the combustion process, the reaction continued for a while and the mixture swelled to a larger volume. Large exothermicity resulted in a high-temperature flame that further decomposed the mixture into gaseous phases and aluminates. The combustion process was completed in less than 5 min. The resulting powders were gently ground and annealed in hydrogen atmosphere. $ZnAl_2O_4:Ce^{3+},Tb^{3+}$ powder phosphors with different concentrations of Ce^{3+} and Tb^{3+} were prepared in this manner. These were analyzed with x-ray diffraction (XRD), scanning electron microscopy, photoluminescence spectroscopy, and Auger electron spectroscopy (AES) coupled with cathodoluminescence (CL) spectroscopy.

6.3 Results and discussions

Figure 6.1 shows the XRD patterns of undoped $ZnAl_2O_4$ (annealed in air at 700^oC) and $ZnAl_2O_4$:Ce^{3+},Tb^{3+} powders (annealed at 700^oC in H_2 atmosphere). Annealing in H_2 was meant to among other things reduce Ce from non-luminescing Ce^{4+} oxidation state to the luminescing Ce^{3+} state. The XRD patterns confirm that both undoped and Ce^{3+}-Tb^{3+} co-doped samples crystallized in a well known spinel structure of $ZnAl_2O_4$ as indexed by JCPDS file No. 082-1043. Note that the diffraction peaks of the Ce^{3+}-Tb^{3+} co-doped sample were more broadened than those of the undoped sample. This is probably due to lattice strains [10] as a result of incorporation of Ce^{3+} and Tb^{3+} ions and this behavior is consisted with the results explained in the previous chapter through the use of Williamson-Hall method. The HR-SEM images of the $ZnAl_2O_4$ powders in Fig. 6.2 (a) show the platelet-like particles encrusted with smaller particles on the surface. Fig. 6.2 (b) shows an agglomeration of spheroidal particles on the surface of a platelet like particle. It is therefore clear that the powders are composed of platelets like particles encrusted with spherical nanoparticles (with some degree of faceting) with an average diameter of ~20 nm.

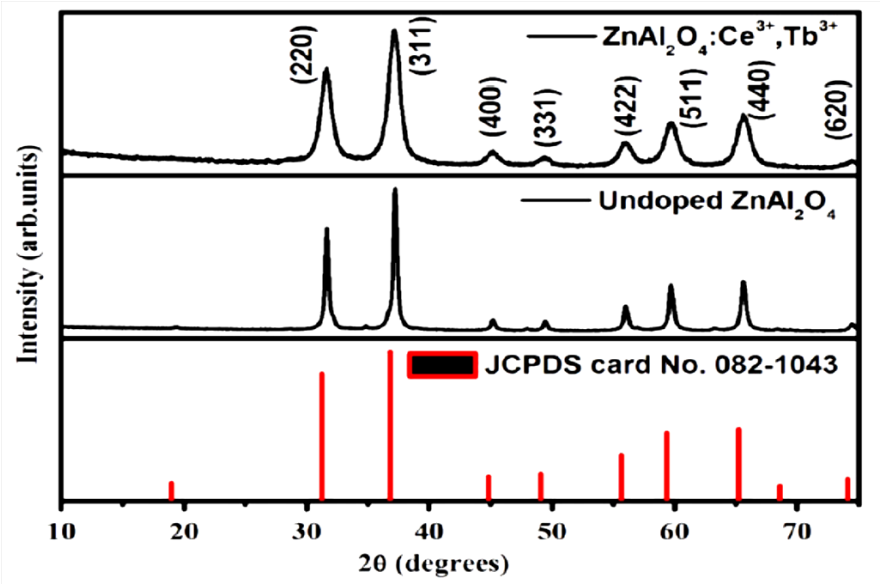

Figure 6-1 The XRD patterns of $ZnAl_2O_4$ and $ZnAl_2O_4$:Ce^{3+},Tb^{3+} powders annealed at 700^oC.

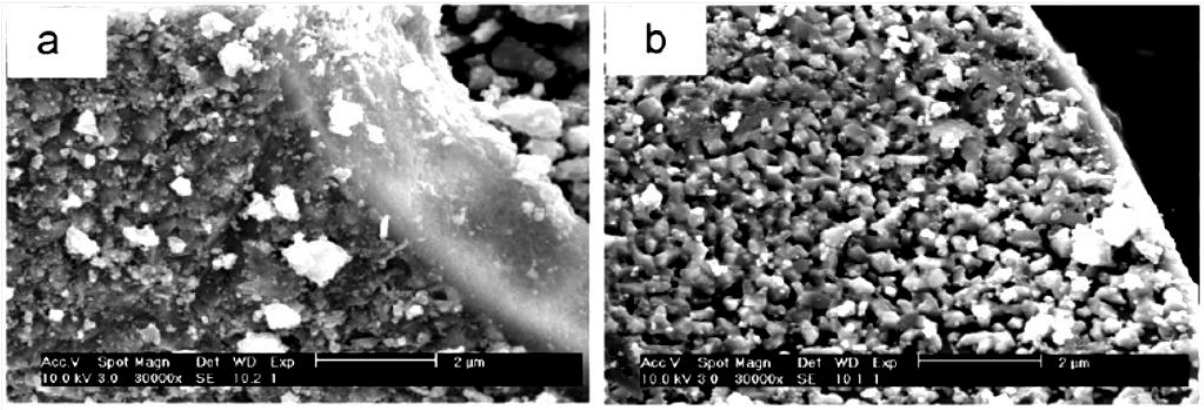

Figure 6-2 High resolution SEM images of the $ZnAl_2O_4$:Ce^{3+}, Tb^{3+} powder annealed at 700°C.

The emission spectrum of Ce^{3+} singly doped $ZnAl_2O_4$ phosphor excited at 256 nm in Fig. 6.3 consists of a broad band with two maxima at 350 and 410 nm. These emissions correspond to the allowed transitions from the lowest sublevel of the 5d state to the $^2F_{7/2}$ and $^2F_{5/2}$ multiplets of the 4f configuration in Ce^{3+} [4]. Dual emission was observed from the $ZnAl_2O_4$ powders co-activated with different concentrations of Ce^{3+} and Tb^{3+} when excited at 230 nm. This was a combination of line emissions from Tb^{3+} ions and broad emission from Ce^{3+}. The green line emission associated with $^5D_4 \rightarrow {}^7F_5$ transitions of Tb^{3+} at 543 nm was more intense than the purplish-blue broad emission of Ce^{3+} at 350−410 nm. The green emission was maximized when 1 mol% of Tb^{3+} was co-doped with 0.75 mol % of Ce^{3+}. The enhancement of the green emission and the subsequent decrease in the blue emission suggests that energy was transferred, most probably by phonon mediated processes, from Ce^{3+} to Tb^{3+}. The proposed mechanism for this transfer is presented in Fig. 6.4. According to this mechanism, the excitation energy absorbed by Ce^{3+} is transferred by the low lying $^5D_{3/2}$ of the Ce^{3+} to the $^5D_4$ state of Tb^{3+} ion followed by an improved emission of green photons at 543 nm.

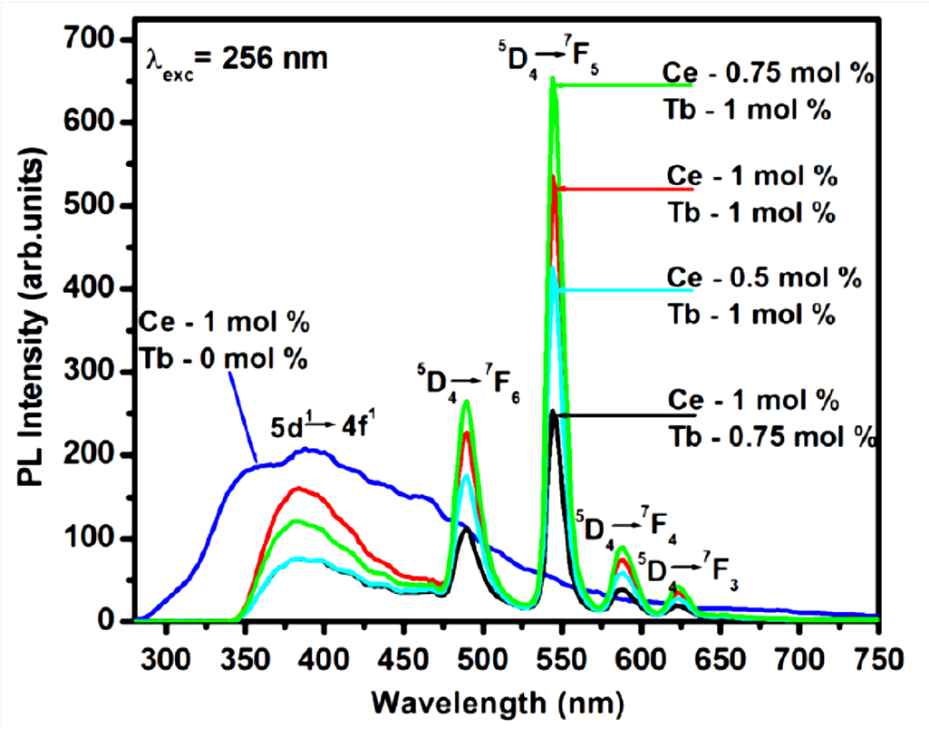

Figure 6-3 PL emission and excitation of $ZnAl_2O_4:Ce^{3+}$, Tb^{3+} with different concentrations of Ce^{3+} and Tb^{3+}

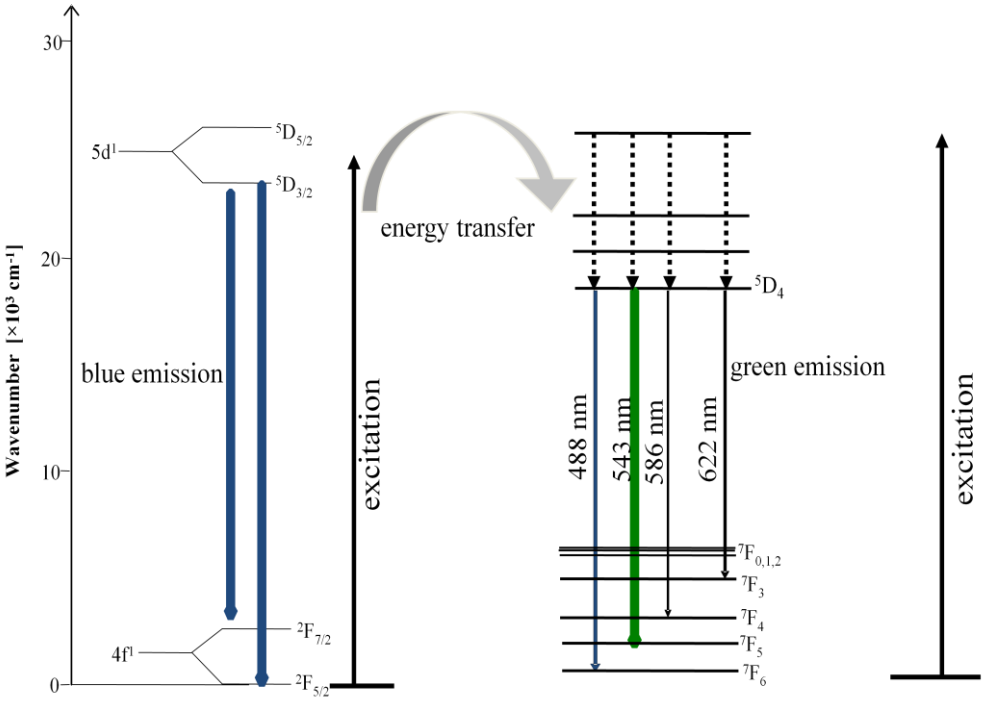

Figure 6-4 Possible mechanism of energy transfer from Ce^{3+} to Tb^{3+}

Figure 6.5 show the Auger-peak-to-peak heights (APPHs) of O, Al, Zn, adventitious C and CL intensity as a function of electron dose. The AES and CL data were collected simultaneously when the powders were irradiated with a beam of electrons (for 10 hrs) in a vacuum chamber maintained at 1×10^{-7} Torr O_2 atmosphere. The O and Zn Auger peaks were almost stable during the electron beam irradiation. The Al peak increased from 0 – 300 $C.cm^{-2}$ and then stabilized while the adventitious C peak decreased drastically from 0 – 600 $C.cm^{-2}$ before stabilizing. The C was probably removed from the surface as CO_x ($x \leq 2$) following the reaction with volatile O species. The simultaneous increase of the CL intensity with the removal of C between 0 – 600 $C.cm^{-2}$ suggests that the presence of C on the surface inhibited light emission from the surface. The CL intensity decreased slightly after 600 $C.cm^{-2}$ and then remained stable to the end of the experiment. The data in Fig. 6.5 can be explained by the well known electron stimulated surface chemical reaction (ESSCR) model [11].

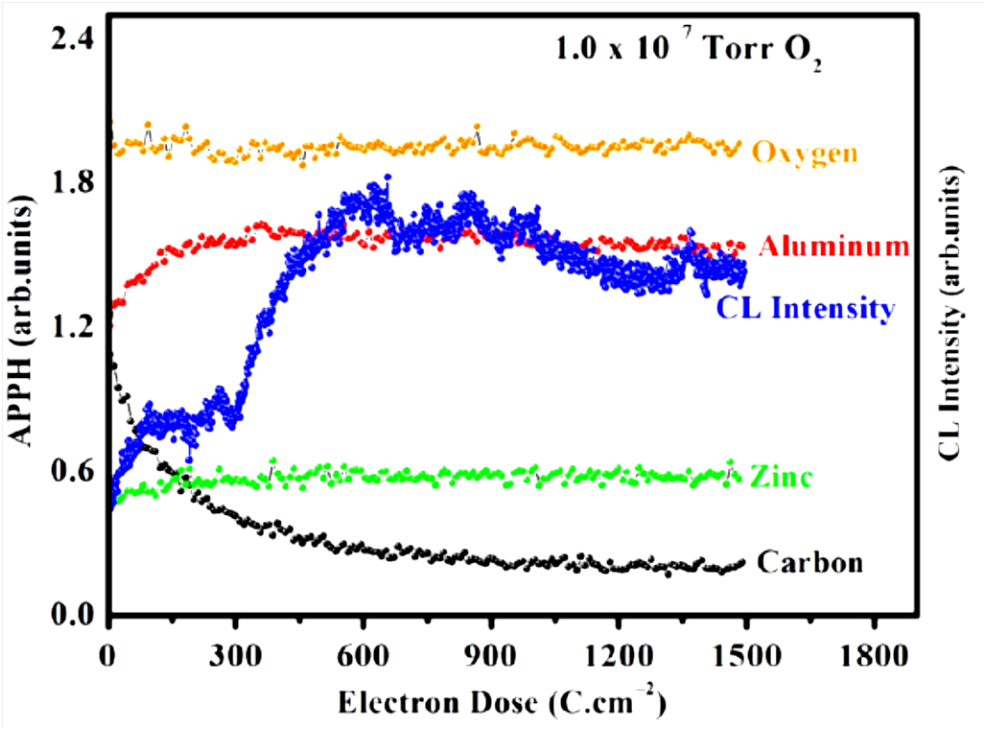

Figure 6-5 Auger peak-to-peak heights of O, Zn, Al and C and the CL intensity as a function of electron dose

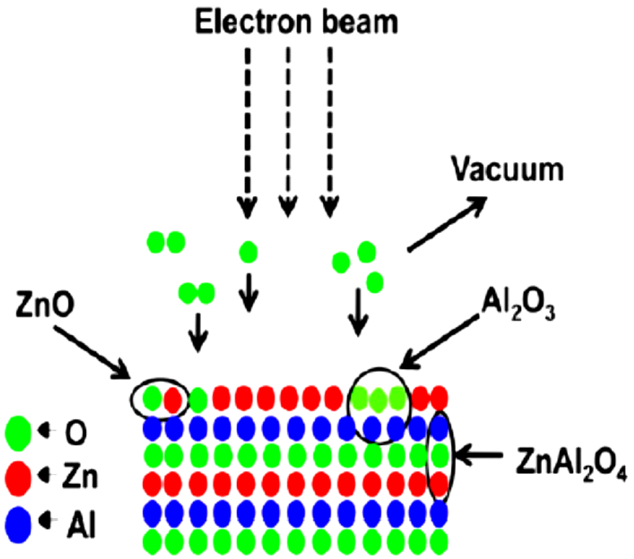

Figure 6-6 The electron stimulated surface chemical reaction (ESSCR) model explaining the possible chemical reaction on the surface of $ZnAl_2O_4:Ce^{3+}$, Tb^{3+} following electron beam irradiation.

The ESSCR model is illustrated in Fig. 6.6. According to this model, electron beam irradiation may dissociate the O-O (from O_2 introduced in the vacuum chamber) and Zn-Al-O bonds resulting in highly reactive O^{2-}, Zn^{2+}, Al^{3+}. The following possible reaction may take place:

$$Zn^{2+} + O^{2-} \rightarrow ZnO, \text{ and} \qquad (\Delta H_f = -348 \text{ kJ/mol}) \qquad (1)$$

$$Al^{3+} + O^{2-} \rightarrow Al_2O_3 \qquad (\Delta H_f = -31676 \text{ kJ/mol}) \qquad (2)$$

Note that both reactions are thermodynamically possible because of their negative values of the enthalpy of formation (ΔH_f). The fact that the Zn and O Auger peaks were stable in Fig. 6.5 suggests that reaction (1) did not take place. The initial increase in the Al Auger peak from 0 – 300 $C.cm^{-2}$ suggest that a possible reaction between Al and O took place resulting in the formation of the Al_2O_3 layer on the surface. As speculated by Pitale et al. [5] this layer acted to protect the surface from degrading. Unlike the adventitious C, it is believed that the protective Al_2O_3 layer did not inhibit light emission from the surface. The fact that the surface did not degrade and the CL intensity was stable after 10 hrs of degradation confirms that this material is chemical stable and needs to be investigated further for a possible future application as a green emitting phosphor in low voltage field emission displays.

6.4 Conclusion

The green emitting $ZnAl_2O_4:Ce^{3+},Tb^{3+}$ phosphor was successfully prepared by the combustion method. The phosphor crystallized in the normal cubic spinel structure of $ZnAl_2O_4$. The green emission was enhanced by energy transferred from Ce^{3+} to Tb^{3+} and the possible mechanism of the energy transfer was discussed. The cathodoluminescence intensity degradation data suggested that the intensity was stable after 10 hrs of electron beam irradiation. This stability was attributed to the formation of the protective Al_2O_3 layer.

6.5 References

[1] X. Duan, D. Yuan, X. Wang and H. Xu, *J. Sol-gel Sci. Technol*. **35** (2005) 221-224

[2] Z. Lou and J. Hao, *Appl. Phys*. **A. 80** (2005) 151-154.

[3] S. Mathur, M. Veith, M. Haas, H. Shen, N. Lecerf, V. Huch**,** S. Hufner, R Haberkon, H.P. Beck and M. Jilavi, *J. Am. Ceram. Soc* **84 (9)** (2001) 1921- 1928.

[4] A.A. da Silva, A.S. Goncalves, M.R. Davolos, and S.H. Santagneli, *J. Nanosci. Nanotechnol*. **8** (2008) 5690-5695.

[5] S.S. Pitale, V. Kumar, I.M. Nagpure, O.M. Ntwaeaborwa, H.C. Swart, *Appl. Surf. Sci.* **257** (2011) 3298-3306

[6] M. Garcia-Hipolito, A. Corona-Ocampo, O. Avarez-Fregoso, E. Martinez, J. Guzman-Mendoza. C. Falcony, *Phys. Stat. Sol*. **(a) 201(1)** (2004) 72-79

[7] B.S. Barros, P.S. Mellow, R.H.G.A. Kiminami, A.C.F.M. Costa, G.F. de Sá and S. Alves Jnr, *J. Mater. Sci*. **41** (2006) 4744-4748.

[8] B.S. Richards, *Solar Energy Materials and Solar Cells*, **90** (2006) 1189-1207.

[9] V. Singh, V Natarajan, J.-J. Zhu, *Opt. Mater*. **29** (2007) 1447-1451

[10] J.-D. Kaminga and L.J. Seijbel, *J. Res. Inst. Stand. Technol*. **109** (2004) 64-75

[11] H.C. Swart, L. Oosthuizen, P.H. Holloway, G.L.P. Berning, *Surf. Interface Anal*. **26** (1998) 339.

CHAPTER 7 ENHANCED GREEN EMISSION FROM UV-DOWN CONVERTING Ce^{3+} - Tb^{3+} CO-ACTIVATED $ZnAl_2O_4$ PHOSPHOR

J. Vac. Sci. Technol. B 30(3) (2012) 031401.1- 031401.6

7.1 Introduction

Zinc aluminate ($ZnAl_2O_4$) with a cubic spinel crystal structure is a family of metal aluminate semiconducting materials that is widely used as ceramic or catalyst. It has a wide band gap of ~ 3.8 eV that makes it suitable for application in optoelectronics. It is used in modern research as a host for rare-earth (e.g. Ce^{3+} and Tb^{3+}) and alkali earth metal ions (e.g. Mn^{2+} and Co^{2+}) [1-5] to prepare phosphors that can be used in different types of light emitting devices. In our preliminary study, we investigated the effects of different parameters such as low activator concentrations, annealing temperatures and excitation wavelengths on the efficiency of green emission from $ZnAl_2O_4$:Ce^{3+},Tb^{3+} [6]. In the present study, we set out to determine systematically the maximum concentration of Tb^{3+} or Ce^{3+} singly activated $ZnAl_2O_4$ and in turn the maximum concentration of Tb^{3+}- Ce^{3+} co-activation that could result in an efficient energy transfer from Ce^{3+} to Tb^{3+} by UV down-conversion process. The objective of this study was to prepare efficient phosphors that can be used as UV down-converting layers to improve the absorption efficiency, hence general performance of the conventional silicon photovoltaic cells. In addition, the phosphors were evaluated for possible application in low voltage cathodoluminescent devices such as field emission display. This was done by irradiating them with 2 keV electrons and monitors the effects of prolonged irradiation on the CL intensity and the electron-beam induced chemical changes taking place on the surface.

7.2 Experimental procedure

Ce^{3+} and Tb^{3+} singly or co-activated $ZnAl_2O_4$ phosphors with different concentrations of Ce^{3+} and Tb^{3+} were prepared by a combustion method. A detailed discussion of the combustion method for the preparation of $ZnAl_2O_4$: Ce^{3+} and $ZnAl_2O_4$: Ce^{3+}, Tb^{3+} phosphors can be found in the literature [6]. In a typical preparation, stoichiometric amounts of zinc nitrate hexahydrate $Zn(NO_3)_2{\cdot}6H_2O$, aluminium nitrate nanohydrate ($Al(NO_3)_3{\cdot}9H_2O$)), urea (CH_4N_2O), cerium nitrate hexahydrate ($Ce(NO_3)_3{\cdot}6H_2O$) and/or terbium nitrate hexahydrate ($Tb(NO_3)_3{\cdot}6H_2O$) of AR grate from Sigma Aldrich (South Korea) were dissolved in de-ionized water. The combustion reaction was carried out in a muffle furnace maintained at 500^{o}C. $ZnAl_2O_4$:Ce^{3+}, $ZnAl_2O_4$:Tb^{3+} and $ZnAl_2O_4$:Ce^{3+}, Tb^{3+} powder phosphors with different concentrations of Ce^{3+} and Tb^{3+} were prepared.

X-ray diffraction (XRD) measurements were performed using a PANalytical X′Pert PRO diffractometer with an X′Celerator detector using CuKα radiation (λ = 1.5406 Å) in the 2θ range of 10 − 80°. An accelerating voltage was set at 40kV and current at 30mA. Photoluminescence (excitation and emission) measurements were carried out at room temperature using Hitachi F-7000 fluorescence spectrometer coupled with a monochromatized xenon lamp with an output power of 150 W. The fluorescence decay data were recorded using an inverted-type scanning confocal microscope (MicroTime-200, Picoquant, Germany). A single-mode pulsed laser diode (375 nm wavelengths with an instrumental response function of ~240 ps in full-width at half maximum, 40 MHz repetition rate, and an average power of ~1 μW) was used as an excitation source. Cathodoluminescent (CL) data were collected via an optical fiber mounted on one of the ports of a vacuum chamber of the PHI 549 Auger spectrometer using Ocean Optics S2000 CL spectrometer. The data were collected when the powders were irradiated with 2 keV electrons continuously for 10 hrs at the chamber pressure of 1.3×10^{-8} Torr. The chemical and electron states of the

irradiated and un-irradiated powders were analyzed using PHI 5000 *versa probe* X-ray photoelectron spectrometer (XPS). High resolution XPS peaks of individual elements were fitted using Multipack **v8.2c** data analysis software.

7.3 Results and discussions

7.3.1 X-ray diffraction (XRD)

Fig. 7.1 shows the XRD patterns of $ZnAl_2O_4$ powder with and without Ce^{3+} and Tb^{3+} activators. The patterns are consistent with cubic $ZnAl_2O_4$ spinel referenced in the JCPDS file No. 05 - 0669. A very small impurity peak that can be ascribed to the (311) diffraction peak of ZnO [7] was detected at $2\theta = 34.9°$ and it was most likely formed as a result of an unwanted reaction between Zn^{2+} and O^{2-} species during the combustion process. The diffraction peaks were all broadened after introduction of the activators. In addition to instrumental settings, peak broadening may be a result of smaller crystallite sizes and/or lattice strains. We however do not expect instrumental settings or preparation procedure to influence the peak broadening because the settings and procedure were kept the same in all cases. It is therefore reasonable to attribute the peak broadening to lattice strains probably induced by the introduction of the rare-earth activators [6]. Note that post-preparation annealing at 700^oC (data not shown) did not influence either the crystallinity or peak intensities of the samples, suggesting that it is possible to obtain highly crystalline $ZnAl_2O_4$ at an initiating combustion temperature of 500^oC without post-preparation heat treatment.

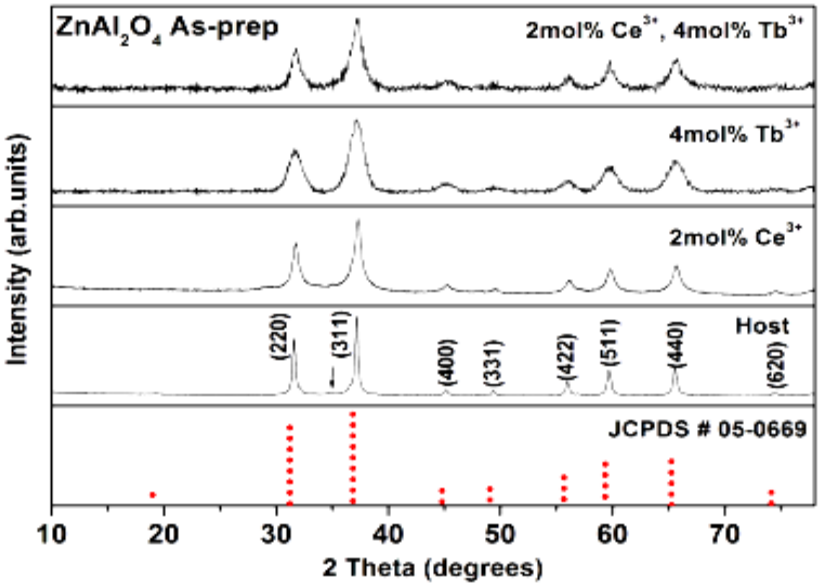

Figure 7-1 XRD patterns of as-prepared $ZnAl_2O_4$, $ZnAl_2O_4:Ce^{3+}$, $ZnAl_2O_4:Tb^{3+}$ and $ZnAl_2O_4:Ce^{3+}$, Tb^{3+} powders.

7.3.2 Photoluminescence (PL)

The maximum intensity from Ce^{3+} and Tb^{3+} singly doped $ZnAl_2O_4$ was obtained with the dopant concentration 2 and 4 mol% respectively. Fig. 7.2 shows emission spectra of $ZnAl_2O_4$:4mol%Tb^{3+} (λ_{exc} = 228 nm) and $ZnAl_2O_4$:2mol%Ce^{3+} (λ_{exc} = 275 nm). The well-known characteristic emissions associated with the $^5D_4 - {}^7F_J$ ($_{J = 3, 4, 5 \& 6}$) transitions of Tb^{3+} were observed with the major emission at 543 nm ($^5D_4 - {}^7F_5$ transition). The PL emission spectrum of $ZnAl_2O_4:Ce^{3+}$ consists of broad emission band with a maximum at 360 nm. This emission can be associated with $5d^1 \rightarrow 4f^1$ transitions of Ce^{3+} [8-10]. The PL emission (λ_{exc} = 275 nm) spectra of the co-activated $ZnAl_2O_4:Ce^{3+}$, Tb^{3+} powders are compared to that of Tb^{3+} (4 mol%) singly activated $ZnAl_2O_4$ in Fig. 7.3. The concentration of Ce^{3+} was fixed at 2 mol. % and that of Tb^{3+} was varied from 1-5 mol% in $ZnAl_2O_4:Ce^{3+}$, Tb^{3+}. It is clear that the intensity of the green emission at 543 nm from $ZnAl_2O_4:Tb^{3+}$ was much smaller than that from $ZnAl_2O_4:Ce^{3+}$, Tb^{3+}. The broad blue emission from Ce^{3+} at ~360 nm was almost quenched while the major green emission from Tb^{3+} at 543 nm was improved due to Ce^{3+} co-doping. Similar to the PL data of Ce^{3+} and Tb^{3+} singly doped samples (Fig. 7.2), the green

emission was maximized when 2 mol% of Ce^{3+} was co-doped with 4 mol% of Tb^{3+}, which suggest that the 4 mol% Tb^{3+} content was the critical concentration for enhancement of luminescence when coupled with the critical concentration from Ce^{3+} at 2 mol% as shown in the inset. The enhancement of the green emission from Tb^{3+} and the simultaneously quenching of Ce^{3+} emission at ~360 nm suggest that Ce^{3+} acted to harvest high energy UV photons from the excitation source and they were subsequently down-converted to low energy visible photons to enhance the green emission from Tb^{3+}. As previously reported [11] energy transfer from Ce^{3+} to Tb^{3+} by the down-conversion process is probably by phonon mediated processes. UV down-converting phosphor can be used as coatings in conventional silicon photovoltaic (PV) cells to absorb UV photons from sunlight and down-convert them to visible photons that can be easily captured and converted to electrical energy by silicon and a subsequent improvement of the general performance of PV cells. Chung and Holloway [12] reported improved performance of the PV cells when the cells were coated with a photoluminescent Y_2O_3:Eu^{3+} layer.

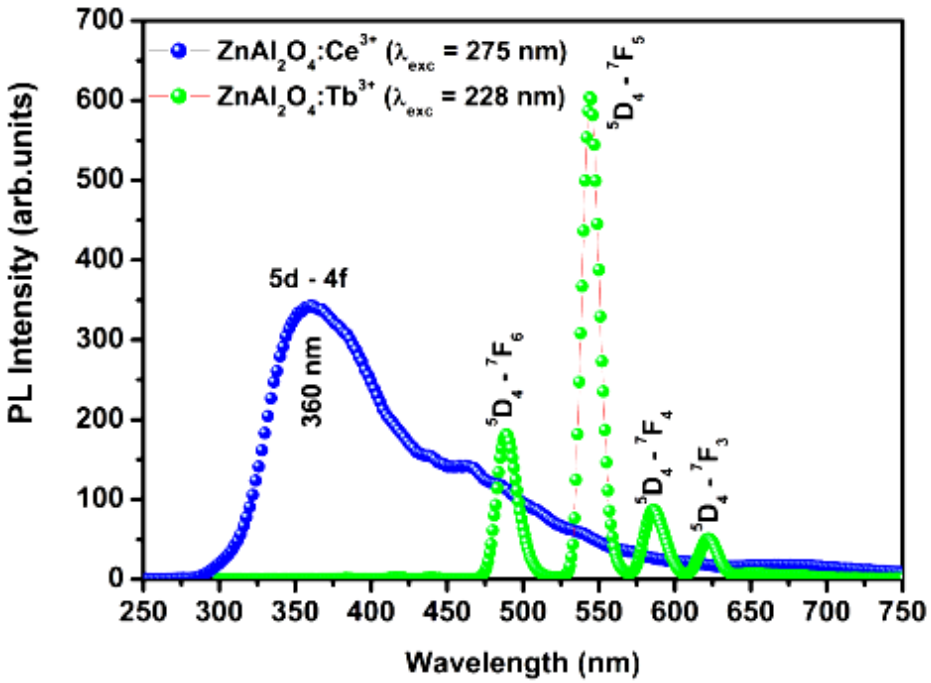

Figure 7-2 PL emission spectra $ZnAl_2O_4$: Tb^{3+} (λ_{exc} = 228 nm) and $ZnAl_2O_4$: Ce^{3+} (λ_{exc} = 275 nm)

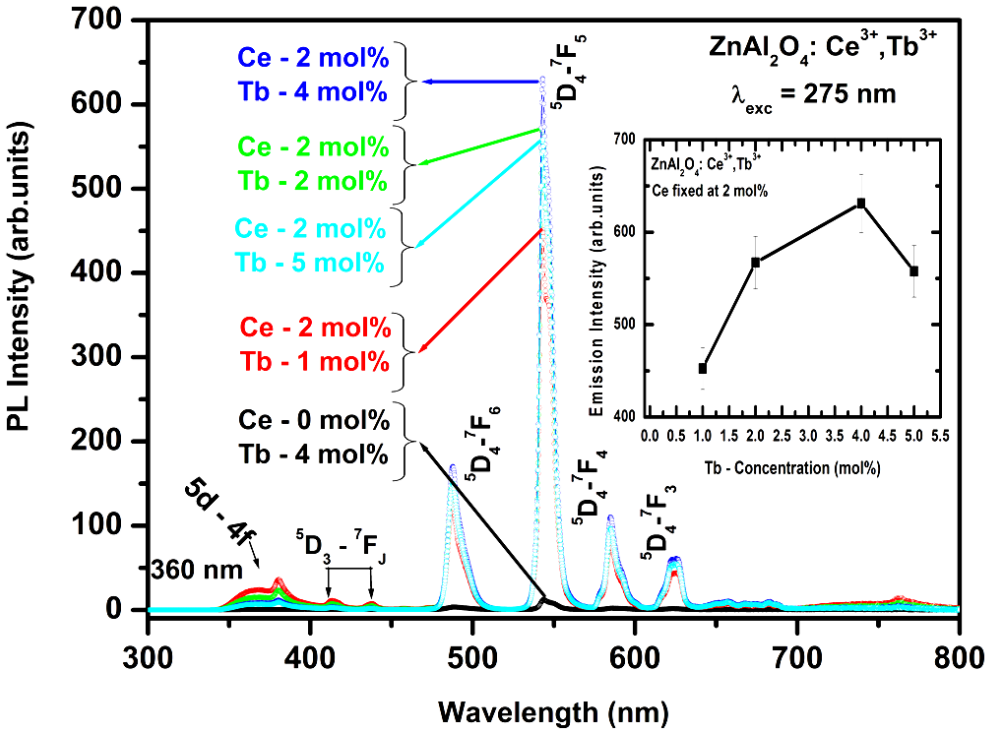

Figure 7-3 PL emission spectra of $ZnAl_2O_4$:Ce^{3+}, Tb^{3+} (λ_{exc} = 275 nm) with different concentrations of Tb^{3+} whereas the Ce^{3+} concentration was fixed at 2 mol. %. The inset is the plot of maximum emission intensity of the 543 nm peak as a function of Tb-concentration

7.3.3 Fluorescence Decay

Fig. 7.4 shows fluorescence decay curves of $ZnAl_2O_4$: 2mol%Ce^{3+} (λ_{em} = 410 nm), $ZnAl_2O_4$: 4mol%Tb^{3+} (λ_{em} = 543 nm) and $ZnAl_2O_4$: 2mol%Ce^{3+}, 4mol%Tb^{3+} (λ_{em} = 410 nm) powders recorded when the powders were excited at 375 nm using a single mode pulsed diode laser. The average lifetimes calculated using the procedure reported in ref. [7] were 39.22 ns, 8.01 ns and 28.93 ns for $ZnAl_2O_4$: 2mol%Ce^{3+}, $ZnAl_2O_4$: 4mol%Tb^{3+} and $ZnAl_2O_4$:2mol%Ce^{3+}, 4mol%Tb^{3+} respectively. Notice that the lifetime of the 410 nm emission of $ZnAl_2O_4$:2mol%Ce^{3+}, 4mol%Tb^{3+} was 10.29 ns shorter than that of $ZnAl_2O_4$: 2mol%Ce^{3+}. The shortening of this emission suggests that some of the absorbed UV photons were transferred to Tb^{3+} at a rate faster than the radiative emission by Ce^{3+}.

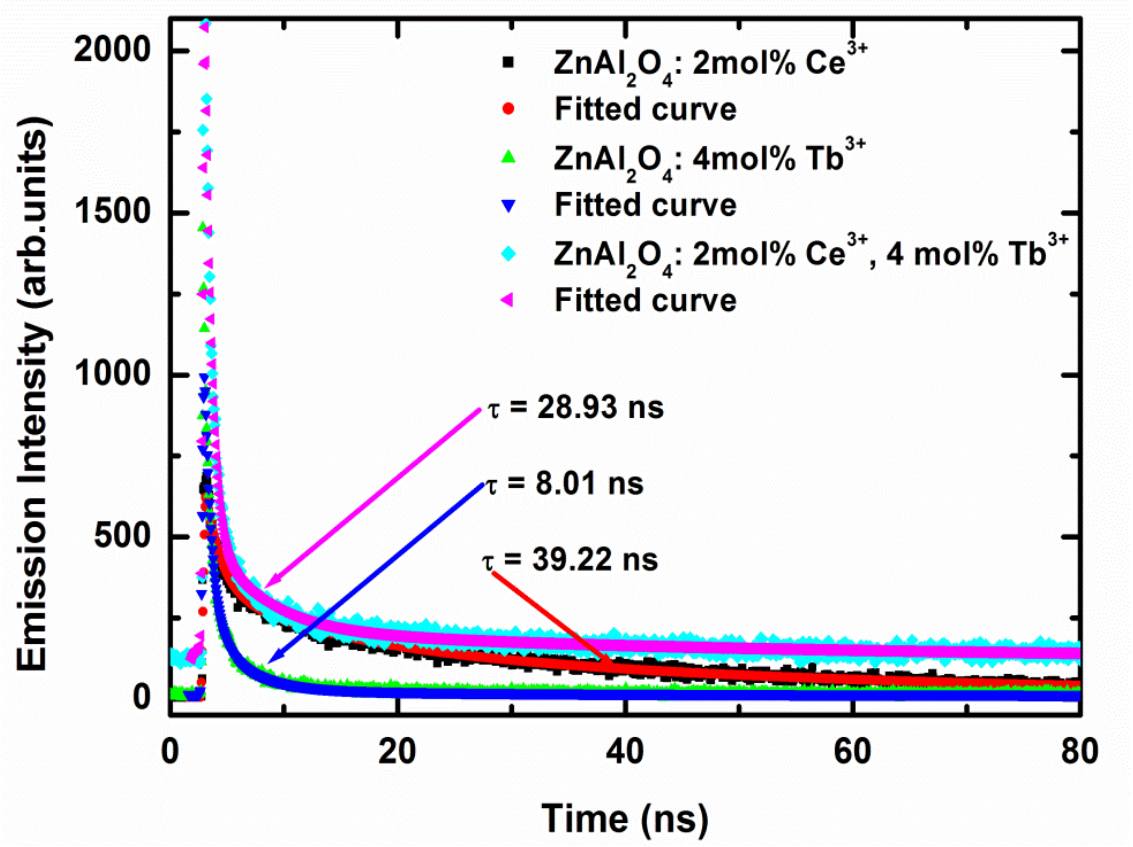

Figure 7-4 Decay curves of $ZnAl_2O_4$: 2 mol % Ce^{3+}, $ZnAl_2O_4$: 4 mol % Tb^{3+} and $ZnAl_2O_4$: 2 mol % Ce^{3+}, 4 mol % Tb^{3+}.

7.3.4 Cathodoluminescence and X-ray photoelectron spectroscopy

Fig. 7.5 shows the CL emission spectra of $ZnAl_2O_4$: 2mol% Ce^{3+}, 4mol% Tb^{3+} powder recorded before and after the powder was irradiated with 2 keV electrons for 10 hrs. The irradiation was carried out in a vacuum chamber of the PHI 549 Auger spectrometer at a base pressure of 1.3×10^{-8} Torr. The CL intensity of the main emission peak at 543 nm was reduced to ~55% of the initial intensity after 10 hrs of continuous irradiation, i.e. the CL intensity was degraded by 45%. This reduction was relatively slow suggesting that to some extent this material can withstand electron irradiation and can therefore be developed into a good phosphor for possible application in low voltage flat panel displays.

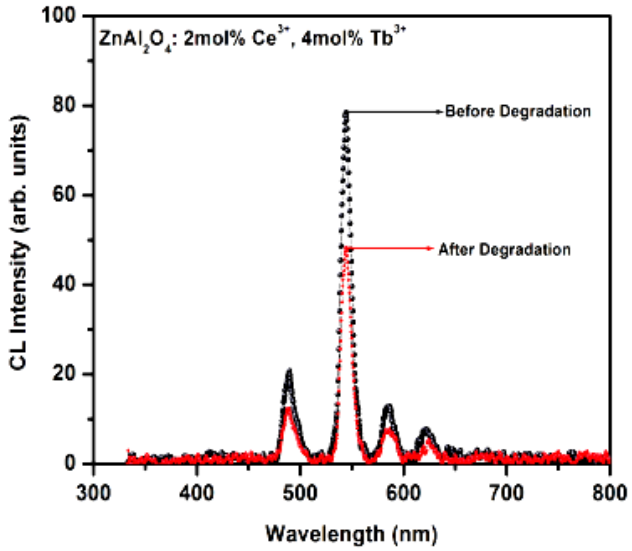

Figure 7-5 CL emission spectra of $ZnAl_2O_4$:2mol% Ce^{3+}, 4mol% Tb^{3+} powder phosphor before and after electron irradiation (degradation).

The chemical and electronic states of degraded (irradiated) and undegraded $ZnAl_2O_4$:Ce,Tb powders were analyzed using X-ray photoelectron spectroscopy (XPS). Figures 7.6 and 7.7 show respectively the fitted O 1s XPS peak before and after degradation. The peaks at 530.1 and 531.3 eV in Fig. 7.6 are O peaks in the $ZnAl_2O_4$ lattice [16], while the 532.7 eV and 528.8 eV peaks can respectively be assigned to O atoms chemically bonded to chemisorbed and Ce/Tb-O [13,14]. As shown in Fig. 7.7, additional peaks developed at 529.6 eV and 529.7 eV after 10 hrs of electron irradiation and they can be assigned to O in

newly formed oxygen-deficient $ZnO_{x<1}$ and Al_2O_3 compounds. These compounds were possibly formed as a result of chemical rearrangements on the surface following bond breaking by irradiation with 2 keV electrons. While $ZnO_{x\leq1}$ is known to affect the CL intensity negatively since it is non-luminescent [15], Al_2O_3 has been reported to act as a protective layer slowing down the rate of the CL intensity degradation [16].

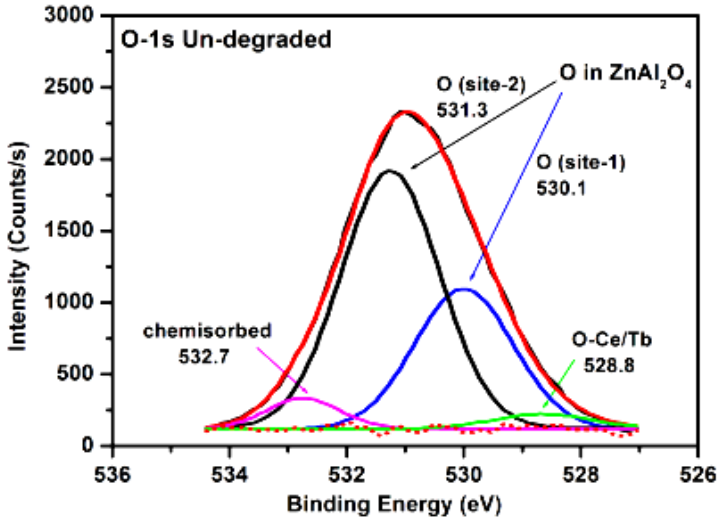

Figure 7-6 XPS spectrum of O 1s in $ZnAl_2O_4$ before degradation

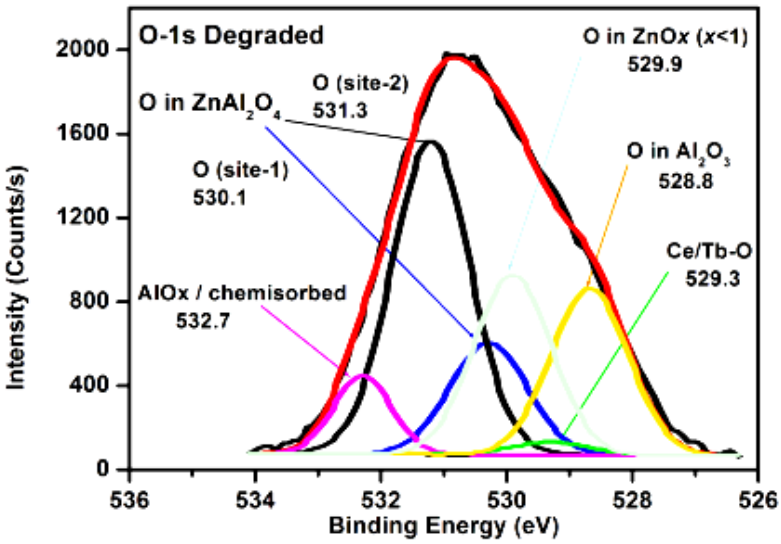

Figure 7-7 XPS spectrum of O 1s (degraded) in $ZnAl_2O_4$ after degradation

Figure 7.8 is the high resolution XPS profile of the Al-2p before degradation. It shows that Al occupies two different lattice sites, namely: the tetrahedral and octahedral. Al peak occupying the tetrahedral site (AlO_4) was detected at 72.7 eV [17] while the peak occupying the octahedral site (AlO_6) was at 74.2 eV [17]. After 10 hrs of irradiation, additional two peaks developed at 75.4 and 71.6 eV (Fig. 7.9) and they can be assigned to Al bonded to Al_2O_3 [18] and oxygen-deficient $Al_2O_{x<3}$ [19] respectively.

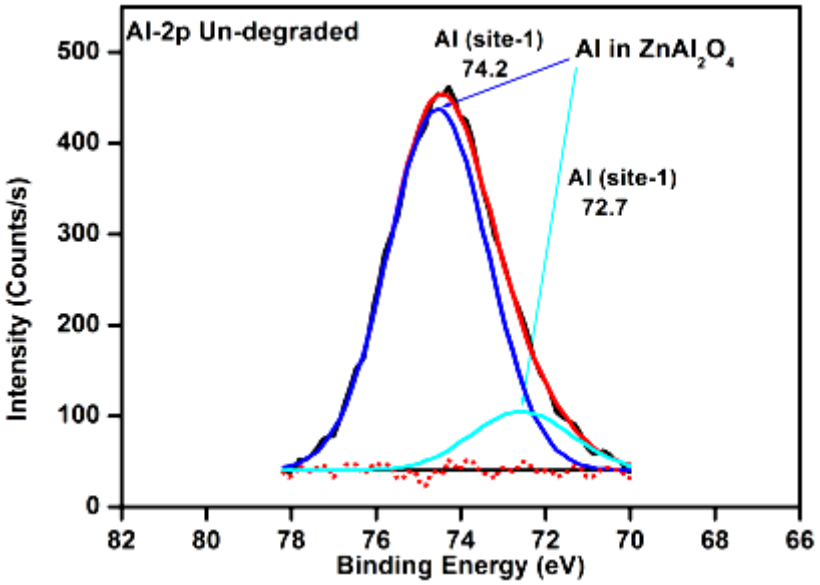

Figure 7-8 XPS spectrum of Al 2p in $ZnAl_2O_4$ before degradation

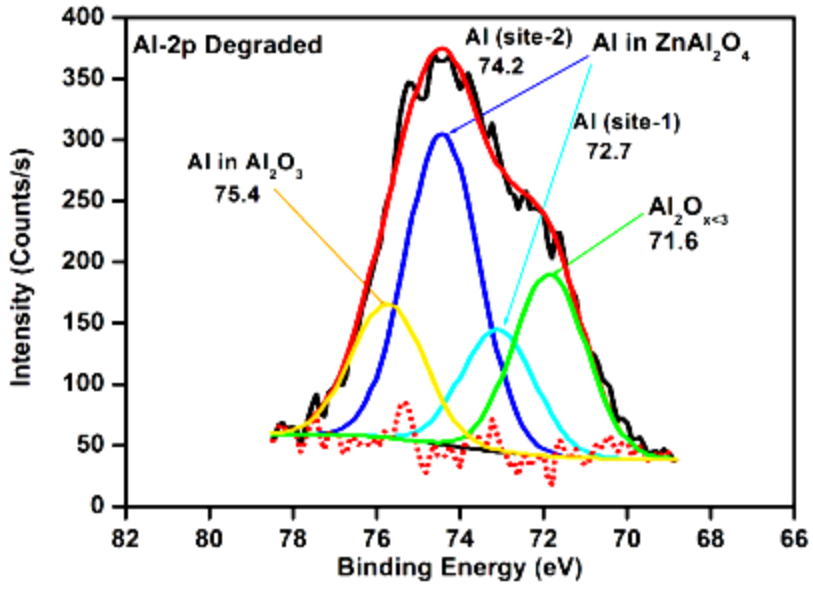

Figure 7-9 XPS spectrum of Al 2p in $ZnAl_2O_4$ after degradation

Fig. 7.10 shows undegraded 3d XPS peak of Ce. The peaks at 880.9, 885.8, 899.6 and 904.9 eV can be attributed to Ce^{3+}, while those at 883, 902.6 and 907.8 eV can be attributed to Ce^{4+} [20]. Similar peaks were observed after degradation as shown in Fig. 7.11. A very distinct satellite peak also assigned to Ce^{4+} was observed at 917.7 eV [20]. It can therefore be concluded that although Ce was mostly present in trivalent oxidation state (Ce^{3+}) there were traces of Ce^{4+} ions. The development of additional 917.7 eV in the degraded spectrum points to the possible oxidation of Ce^{3+} to Ce^{4+} during electron beam irradiation.

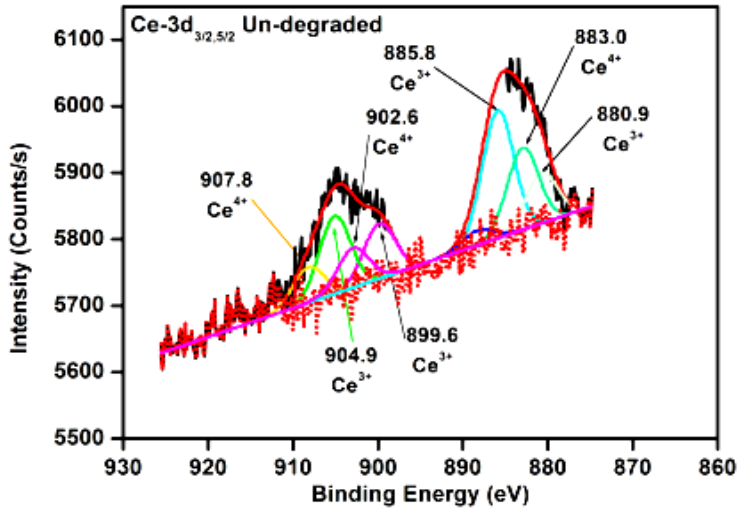

Figure 7-10 XPS spectrum of Ce-3d in $ZnAl_2O_4$ before degradation

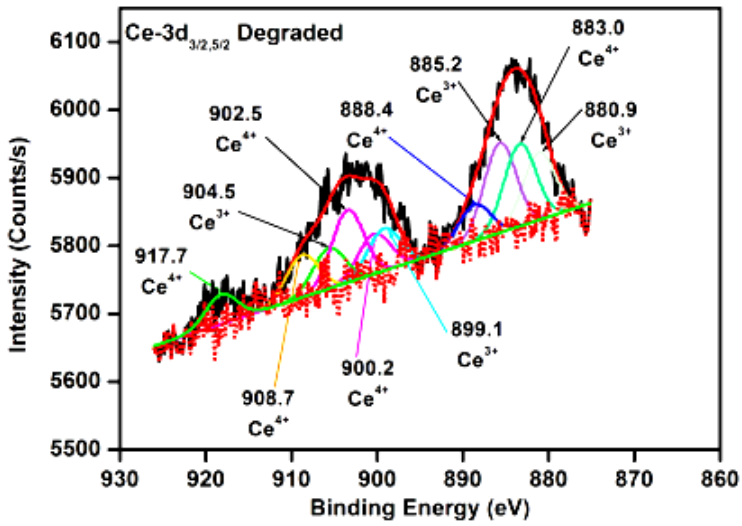

Figure 7-11 XPS spectrum of Ce-3d in $ZnAl_2O_4$ after degradation

The 3d XPS peaks of Tb before and after degradation are shown respectively in Fig. 7.12 and 7.13. Peaks associated with the 3+ and 4+ oxidation states of Tb are clearly marked in both undegraded and degraded XPS spectra and they were assigned according to ref. [21]. Generally, both the peak intensities and positions were stable in both spectra.

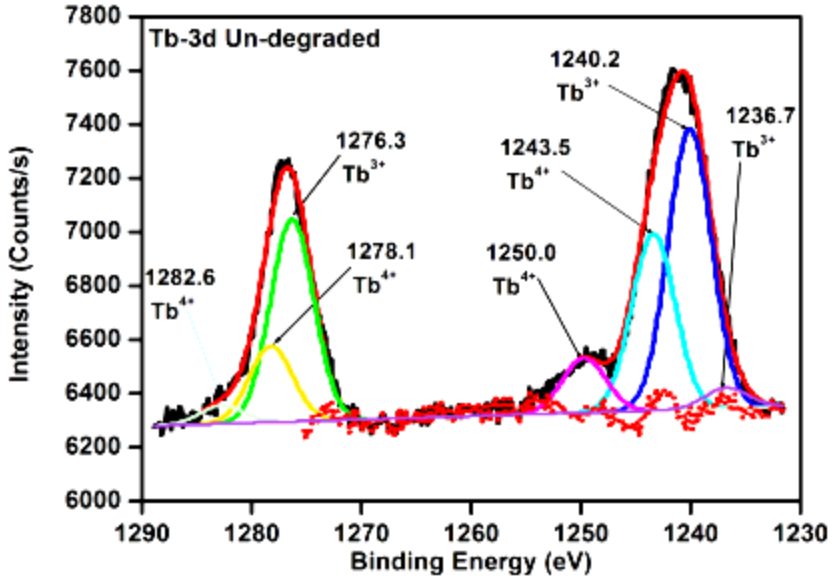

Figure 7-12 XPS spectrum of Tb-3d in $ZnAl_2O_4$ before degradation

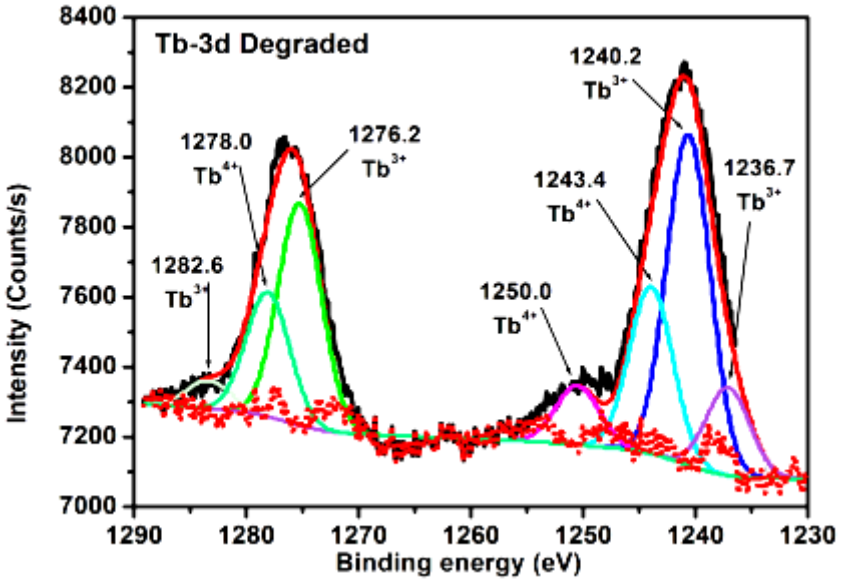

Figure 7-13 XPS spectrum of Tb-3d (degraded) in $ZnAl_2O_4$ after degradation.

Table 7.1 gives a summary of the XPS peak position, chemical bonding, and area distribution of the $ZnAl_2O_4$:Ce, Tb powder before and after degradation.

Table 7-1 XPS peak position, chemical bonding, and area distribution before and after degradation.

$ZnAl_2O_4$:Ce,Tb					
Oxidation state	**Before deg.**		**After deg.**		
	BE (±0.1eV)	**Area distri.**	**BE (±0.1eV)**	**Area distri.**	**Chem. Bonding**
O – 1s					
	528.8	4%	528.8	3%	Ce/ Tb–O
	530.1	31%	530.1	14%	O in $ZnAl_2O_4$
	531.3	60%	531.3	37%	O in $ZnAl_2O_4$
	532.7	6%	----	---	chemisorbed sp.
.			527.9	20%	O in Al_2O_3
			532.7	7%	AlOx /chemisorbed
			529.6	20%	O in ZnOx (x<1)
Al– 2p					
	72.7	14%	72.7	12%	Al in AlO_4 of $ZnAl_2O_4$
	74.2	86%	74.2	41%	Al in AlO_6 of $ZnAl_2O_4$
			75.4	18%	Al in Al_2O_3
			71.6	25%	Al in $Al_2O_{x<3}$
Ce– 3d					
	880.9	10%	880.9	12%	Ce^{3+} bonding
	885.8	25%	885.2	17%	
	899.6	11%	899.1	8%	
	904.9	16%	904.5	8%	
	883.0	16%	883.0	16%	Ce^{4+} bonding
			888.4	7%	
			900.2	7%	
	902.6	7%	902.5	13%	
	907.8	7%	908.7	8%	
			917.7	5%	
Tb – 3d					
	1240.2 ($3d_{5/2}$)	33%	1240.2 ($3d_{5/2}$)	33%	Tb^{3+} bonding
	1276.3 ($3d_{3/2}$)	24%	1276.2 ($3d_{3/2}$)	22%	
	1236.7	3%	1236.7	8%	
	1243.5 ($3d_{5/2}$)	21%	1243.4 ($3d_{5/2}$)	16%	Tb^{4+} bonding
	1278.1 ($3d_{3/2}$)	9%	1278.0 ($3d_{3/2}$)	10%	
	1250.0($3d_{5/2}$)	6%	1250.0 ($3d_{5/2}$)	6%	
	1282.6 ($3d_{3/2}$)	3%	1282.6 ($3d_{3/2}$)	2%	

7.4 Conclusion

We have demonstrated improved UV down-converted green photoluminescence from $ZnAl_2O_4$:Ce,Tb powders (with different concentrations of Ce^{3+} and Tb^{3+}) as a result of energy transfer from Ce^{3+} to Tb^{3+}. The maximum PL intensity was observed from the powder co-activated with 2 mol% and 4 mol% of Ce^{3+} and Tb^{3+} respectively. As evidence of energy transfer, we demonstrated the shortening of the decay lifetime of Ce^{3+} in $ZnAl_2O_4$:Ce,Tb powder by 10.29 ns and we concluded that the shortening was a result of a transfer of absorbed UV photons at a rate faster than the radiative transition of Ce^{3+} states. In addition, we demonstrated a 45% reduction of cathodoluminescence intensity of the green emission at 543 nm as a result of prolonged irradiation of the $ZnAl_2O_4$:Ce,Tb powders by 2 keV electrons. The XPS data suggest that additional phases such as oxygen deficient $ZnO_{x<1}$ and $Al_2O_{x<3}$ were formed on the surface during electron irradiation. Since $Al_2O_{x\leq3}$ was reported to protect the surface from degrading, we attributed the loss of the CL intensity to the non-luminescent $ZnO_{x\leq1}$ phase. It is also likely that non-luminescent Ce^{4+} and Tb^{4+} ions contributed to the loss of the CL intensity.

7.5 References

[1] X. Duan, D. Yuan and F. Yu, *Inorg. Chem*. **50**, (2011) 5465.

[2] B. Cheng, S. Qu, H. Zhou, Z. Wang, *Nanotechnology* **17**, (2006) 2982–2987.

[3] X.Y. Chen, C. Ma, S.P. Bao, Z. Li, *J. Colloid Interface Sci.* **346**, (2010) 8–11.

[4] C.D.Herna´ndez-Pe´rez, M.Garcı´a-Hipo´lito, M.A.A´ . lvarez-Pe´rez, O.A´ . lvarez-Fregoso, F.Ramos-Brito,C.Falcony, *Phys.Status Solidi* **A 207**, (2010) 417–422.

[5] G. Müller, *Electroluminscence II Semiconductor and Semimetal*, Academic Press, New York, (2002).

[6] K.G Tshabalala, S-H. Cho, J.-K. Park, Shreyas Pitale, I.M. Nagpure, R.E. Kroon, H.C. Swart and O.M. Ntwaeaborwa, *J. Alloys Compd* **509** (2011) 10116.

[7] B.S. Barros, P.S. Melo, R.H.G.A. Kiminami, A.C.F.M. Costa, G.F. de Sá and S. Alves Jr, *J. Mater Sci*. **41**, (2006) 4745.

[8] G. Blasse, B.C. Grabmaier, *Luminescent Materials*; ISBN 3-540-58019-0 Springer Verlag: New York. (1994). pp 91- 107

[9] O.M. Ntwaeaborwa and P.H. Holloway, *Nanotechnology*, **16**, (2005) 865

[10] J. Holsa, M. Leskela, L. Niinisto, *J. Solid. State Chem.* **37**, (1981) 267

[11] O.M. Ntwaeaborwa, H.C. Swart, R.E. Kroon, P.H. Holloway and J.R. Botha, *J. Phys. Chem. Sol.* **67**, (2006) 1749

[12] P. Chung and P.H. Holloway, *J. Vac. Sci. Technol* **A. 25(1)** (2007) 61

[13] E. Paparazzo, *Surf. Sci*. **234**, (1990) L253

[14] D.D., Sarma, C.N.R. Rao *J. Electron Spectrosc. Relat. Phenom*. **20**, (1980) 25

[15] H.C. Swart, L. Oosthuizen, P.H. Holloway, G.L.P. Berning, *Surf. Interface Anal*. **26**, (1998) 339

[16] S. S. Pitale, V Kumar, I.M. Nagpure, O.M. Ntwaeaborwa, H.C. Swart, *Applied Surface Science*, **257,** (2011) 3298–3306

[17] R. B., Strohmeier, *Surf. Sci. Spectra* **3 (2)**, (1995) 128–134

[18] I. Olefjord, H.J. Mathieu, P. Marcus, *Surf. Interface Anal*. **15**, (1990) 68

[19] V.K Yatsimirskii, V.V. Lesnyak, I.N. Gut and O. Yu. Boldyreva, *Theoretical and Experimental Chemistry*, **41**, (2005) 135-138

[20] E. Beche, P. Charvin, D. Perarnau, S.Abanades and G. Flamant, *Surf. Interface Anal*. **40**, (2008) 264–267

[21] I.M. Nagpure, Shreyas S. Pitale, E. Coetsee, O.M. Ntwaeaborwa, J.J. Terblans, H.C. Swart, *Applied Surface Science* **257**, (2011) 10147–10155.

CHAPTER 8 STRUCTURE, PHOTOLUMINECENCE PROPERTIES AND XPS STUDIES OF LOW QUARTZ SiO_2 HOST

8.1 Introduction

The fact that SiO_2 can exist in numerous crystalline and amorphous forms, and its status as one of the most prevalent compounds on earth, has stimulated a long history of experimental and theoretical investigations. In recent years, SiO_2 is used as coating material due to its favourable band alignment when forming a heterojunction with other commercial cathode ray tube (CRT) phosphors [1]. It is difficult to achieve spherical morphology with nano sized particles in the SiO_2 glassy matrix. morphology mono-dispersion of particles is very important in terms of application purposes. Several researchers used the melt method [2], precipitation [3] and sol-gel technique [4] as the prominent routes to prepare SiO_2 matrix but these applied routes are not enough to achieve the required morphology.

In the interest of luminescence applications, Ce is one of the most extensively employed activator in the optical industry. The Ce ion was observed in two different states, the luminescence trivalent Ce^{3+} state due to allowed 5d – 4f transition and the non-luminescence Ce^{4+} state. The optical features of Ce in many crystalline and amorphous SiO_2 matrices were intensively investigated from both experimental and theoretical points of view [5, 6]. In fact, the strong dependence of both the energy and the splitting of the 5d levels upon the host matrix significantly affect the rare earth (RE) optical response and works as a powerful probe of the host crystal field [7]. Specifically, the incorporation of Ce as well as of other rare-earth ions inside the glassy matrices, and homogeneous distribution are not straightforward and thus, was the subject of several studies [7- 10]. Meng et al. [11] and Kim et al. [12] used a sol gel route to incorporate Eu^{3+} and Tb^{3+} to investigate energy transfers

between them in the silica matrices. Ntwaeaborwa et al. [4] also used the sol-gel technique to incorporate Ce^{3+}, Tb^{3+} and Eu^{3+} ions and study their mutual energy transfer into nano silica matrices. Nogami [13] and Ntwaeaborwa et al. [14] provide a proof that rare-earth doped amorphous SiO_2 nanophosphor could be used in low voltage FEDs and other related light emitting devices.

In this study, investigations were done on the preparation of nano sized undoped, Ce doped SiO_2 and Ce/Tb co-doped SiO_2 matrices by using the urea assisted combustion method. A reducing atmosphere with the mixture of 4%H_2 and 96%Ar was used during annealing to achieve the homogeneous distribution of luminescence Ce^{3+} ions in the SiO_2 matrix because unlike Ce^{4+}, it is optically active. The structure of the powder samples was studied for phase analysis. The optical properties through photoluminescence (PL) were studied in all prepared powder samples. The morphological analysis was investigated using the scanning electron microscopy (SEM). The oxidation state of the doped Ce ion and main elements such as Si 2p orbital and O 1s orbital before and after annealing in a reducing atmosphere were reported using X-ray photoelectron spectroscopy (XPS).

8.2 Experimental procedure

Undoped nano sized SiO_2, Ce or Tb singly doped SiO_2, and Ce-Tb co-doped SiO_2 were prepared by a solution combustion method as described in reference [15]. Silicic acid ($SiO_2 \cdot nH_2O$) and ammonium nitrate (NH_4NO_3) were used as the starting materials, while urea (CH_4N_2O) was used as fuel. All these materials were dissolved in 10 mL distilled water and stirred for 2 hours in order to obtain a homogeneous transparent mixture. The mixer was then transferred into a muffle furnace which was maintained roughly at 500 ± 5ºC. Lastly, the dried powder after the incorporation of dopants was then annealed in a reducing atmosphere (4% H_2 and 96% Ar) gas at 1000ºC for 2 hours. The phase purity and crystallinity of the

powder samples was characterized by X-ray powder diffraction (XRD). XRD measurements were carried out with a Bruker D8 Advanced powder diffractometer with Cu-Kα radiation (λ = 1.5418 Å) in the 2θ range from 10° to 80°. The morphology of the prepared nanoparticles was analyzed by scanning electron microscopy (SEM) using a Shimadzu model ZU SSX−550 Superscan. The photoluminescence (PL) properties of the powder phosphors were characterized using a Cary Eclipse fluorescence spectrophotometer. The detailed XPS analysis were carried out with a PHI 5000 versa probe spectrometer using monochromatic Al Kα radiation.

8.3 Results and discussion

8.3.1 *X-ray diffraction*

The XRD patterns of the pure SiO_2 and singly doped SiO_2: 4mol%Tb^{3+}, SiO_2:2mol%Ce^{3+} and co-doped SiO_2:2mol%Ce^{3+}, 4mol%Tb^{3+} powders prepared by the combustion method are shown in figure 8.1. The undoped SiO_2 and singly doped SiO_2: 4mol%Tb^{3+} patterns exhibit only a broad peak around 2θ ~ 22°. Although the broadness can be observed from these two profiles, there is peak shift towards lower angle in comparison to the normal amorphous phase in silica where the peak position is mainly located at 2θ ~ 23° as reported in reference [16]. On the other hand, the singly doped SiO_2:2mol%Ce^{3+} and the co-doped sample show a broad peak and some small signatures emanating from low quartz silica. Taking into consideration that the ionic radii of Ce^{3+} (~ 1.11 Å) and Tb^{3+} are larger and the more their concentration is added this induces the microstrains into the SiO_2 system. Thus, the broadening can be attributed to the presence of strain. The observed peaks were assigned by comparing the JCPDS database file no 86-1565 [17], which is the characteristic diffraction pattern of the low quartz's phase of a SiO_2 glassy matrix.

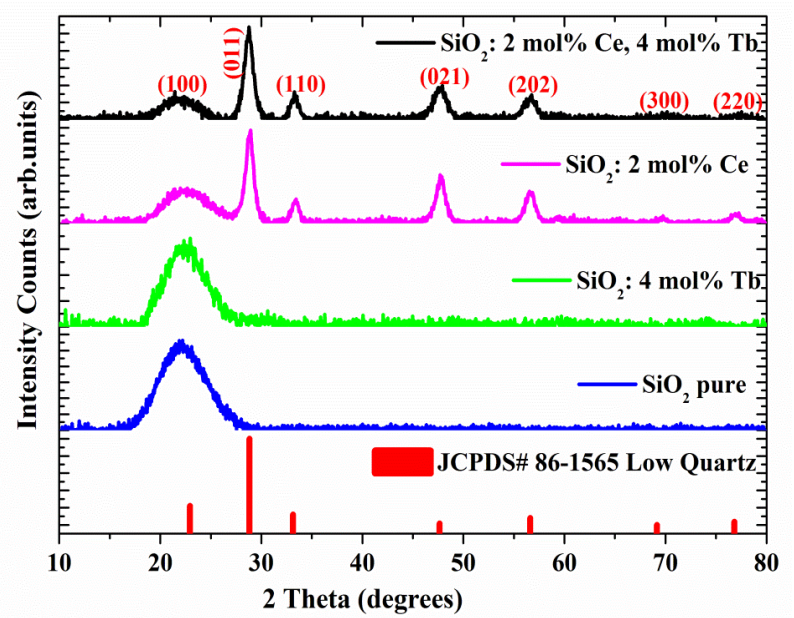

Figure 8-1 Room temperature XRD patterns of (as cast) pure SiO_2 and a singly doped SiO_2: 4mol%Tb^{3+}, SiO_2:2mol%Ce^{3+} and co-doped SiO_2:2mol%Ce^{3+}, 4mol%Tb^{3+} from combustion derived route.

8.3.2 *Scanning electron microscopy (SEM)*

The SEM images in figure 8.2 show the general morphology of the (a) SiO_2:2mol% Ce and SiO_2:2mol% Ce, 4mol% Tb samples, respectively. The SEM image in figure 8.2 (a) shows the agglomerated SiO_2:Ce with small particles appearing circular confirming spherical shapes. However, in figure 8.2 (b) the particles are relatively smaller than that shown in (a), which suggest that the Tb incorporation influenced the rate of nucleation and crystal growth [18].

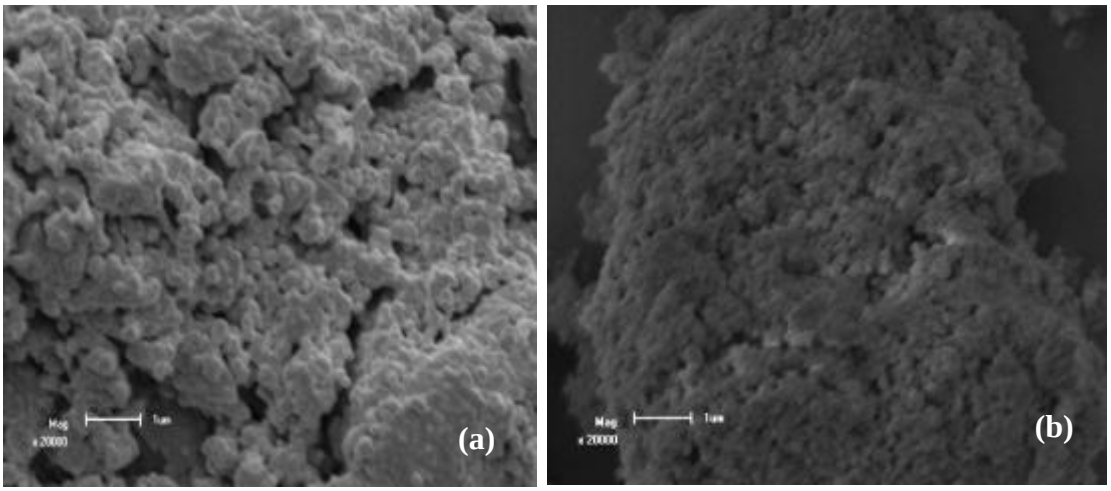

Figure 8-2 SEM images of the (a) SiO_2:2mol%Ce and (b) SiO_2:2mol%Ce,4mol%Tb samples

8.3.3 *Photoluminescence studies*

Figure 8.3 exhibits the PL emission spectra of the reduced singly doped SiO_2:2mol% Ce^{3+}, and SiO_2:4mol% Tb^{3+} and co-doped SiO_2:2mol% Ce^{3+}, 4mol% Tb^{3+} respectively. The emission from singly doped SiO_2:2mol% Ce^{3+} with the maximum roughly at 402 nm is consistent with the 400 nm emission ascribed to Ce^{3+} ions as reported by Kroon et al [19]. On the other hand, PL emission corresponding to Tb^{3+} characteristics from singly doped SiO_2:4mol%Tb^{3+} show sharp emission peaks from upper-laying levels, i.e., $^5D_4 \rightarrow {}^7F_{6,5,4,3}$ at 488, 543, 585 and 620 nm, respectively. These peaks match well with emission intensities from Tb^{3+} ions into nanocrystalline silica, confirming their incorporation into the system, according to the previous results obtained by the authors using sol–gel derived SiO_2 doped with Tb^{3+} [20]. Another interesting observation from Tb singly doped is that the emission shows a well pronounced intensity at 543 nm compared to the co-doped sample. The broad emission band from Ce^{3+} at ~400 nm (fig. 8.3) is suppressed implying that there was no radiative emission from Ce^{3+} when exciting at 227 nm. It is therefore reasonable to conclude that at 227 nm, only Tb ions are excited. Consistent with the report of Barros et al [21] in the $ZnAl_2O_4$: Tb system, this band can be attributed to the $4f^8 \rightarrow 4f^8 5d^1$transition (f → d transition) of Tb^{3+}.

In figure 8.4 the photoluminecence (PL) emission (λ_{exc} = 322 nm) of singly doped SiO_2:2mol% Ce attributed to $5d(^2D) \rightarrow (^2F_{7/2} + {}^2F_{5/2})\ 4f^1$ transition is shown. Figure 8.5 compares the PL emissions (λ_{exc} = 322 nm) for singly doped SiO_2:4mol% Tb and co-doped SiO_2:2mol% Ce, 4mol% Tb in low quartz silica matrix. The PL emission from the singly doped Ce exhibits a broad band centered at 405 nm. This band is also ascribed to Ce^{3+} ions corresponding to the short wavelength defect emission of SiO_2 suggested to be associated with Ge impurities [8,19-21]. The most interesting part about this emission is that it displays a strong signal when the excitation of 322 nm is used compared to 227 nm. Therefore, this excitation of 322 nm is ascribed to direct excitation of Ce^{3+} ions from the 4f → 5d transition

of Ce. The PL intensity of the green emission from Tb^{3+} at 543 nm is high while the blue emission from Ce^{3+} is suppressed when the Ce^{3+}-Tb^{3+} co-doped system is excited at 322 nm. These results suggest that Ce^{3+} acts to harvest excitation energy and transfer it non-radiatively to Tb^{3+}.

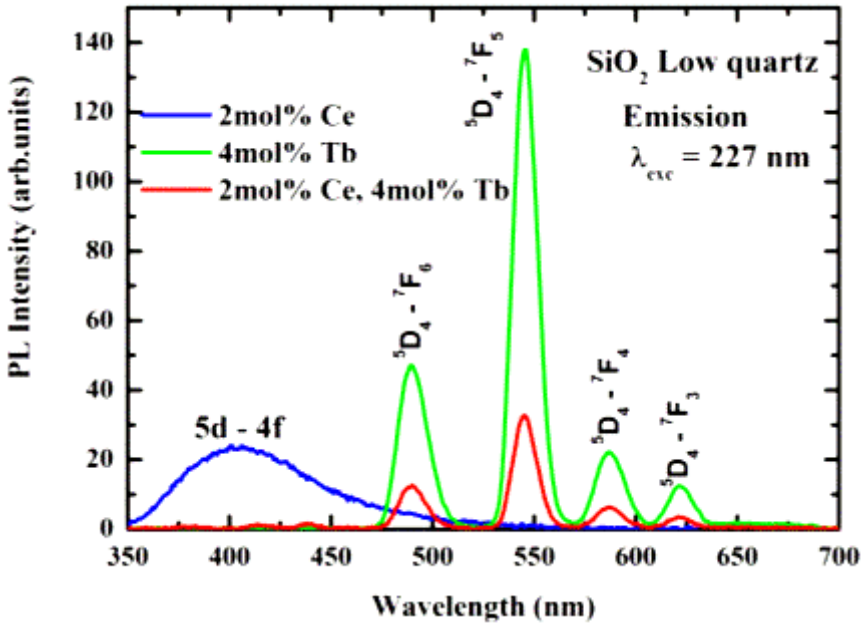

Figure 8-3 PL emission spectra SiO_2:2mol% Ce, SiO_2:4 mol% Tb and SiO_2:2mol% Ce, 4mol% Tb (λexc = 227 nm).

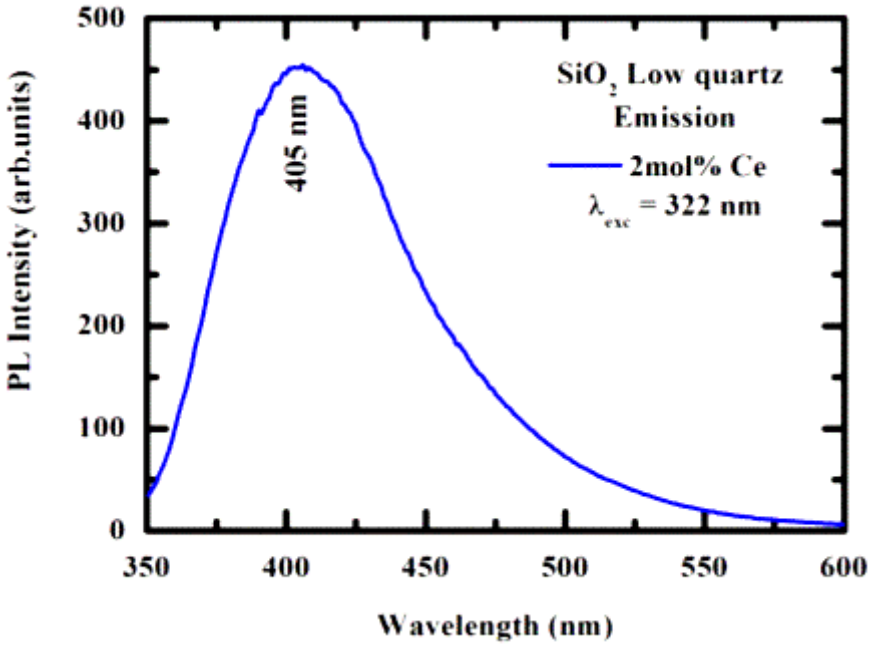

Figure 8-4 PL emission spectra of SiO_2 singly doped with 2 mol%Ce^{3+} under excitation at 322 nm.

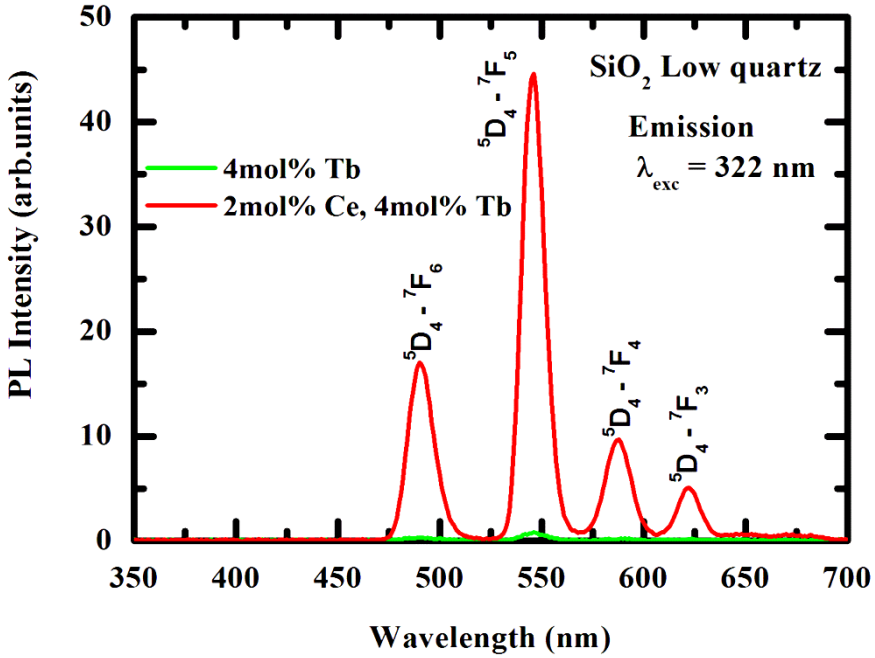

Figure 8-5 PL emission spectra of SiO_2 singly doped 4 mol%Tb^{3+} and co-doped with 2mol%Ce^{3+} and 4mol%Tb^{3+} in mol% under excitation at 322 nm.

8.3.4 *X-ray photoelectron spectroscopy*

In figure 8.6 high resolution Ce $3d_{3/2,5/2}$ XPS peaks of the as-cast and reduced samples are presented. In the reduced sample the signal indicated by (a) is less than that of the as-cast sample indicated by the letter (e). This small difference observed on the shape of the Ce peaks in the two spectra is mainly due to the oxidation state of the Ce in the two samples. The Ce peak at (e) can be attributed to the final state of Ce^{4+} since the peak position is roughly around 915 eV. Moreover, the peaks at (b) and (c) in the reduced sample are more pronounced compared to that of as-cast at (e) and (f). The increase in the peak intensities of (b) and (c) suggest that the Ce^{4+} ions are now being converted into Ce^{3+} ions into silica matrix. Thus, the population of Ce^{3+} has increased remarkably into a reduced sample as confirmed by PL studies.

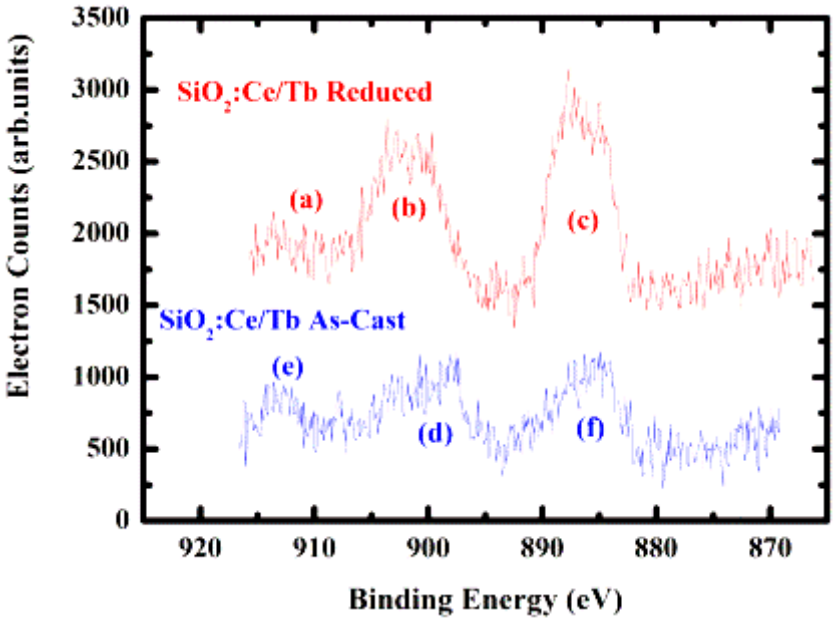

Figure 8-6 XPS spectrum of Ce-3d as-prepared and reduced in SiO_2.

Figure 8.7 and 8.8 show the detailed scans of oxygen O 1s orbital before and after annealing in a reduced atmosphere respectively. Multipak version *9* software [22] was used to deconvolute the O1s XPS peak. In the as-prepared sample (fig. 8.7) the O 1s peak was fitted with two peaks with the maxima at 532.5 and 533.2 eV. The peak at 532.5 eV is arising from the oxygen present in the SiO_2 lattice as Si−O bond from quartz structure. Furthermore, the peak at 533.2 eV correspond to O^{2-} arising from SiO_2 lattice. The peak of oxygen O1s of the reduced sample was fitted into three main peaks with the maxima at 530.5, 532.5 and 533.2eV. The oxygen O1s of the reduced shows a new species at 530.5 eV and this is ascribed to oxygen in CeO_2. However, the peak intensity at 532.5 eV has increased in a reduced sample compared to that of the as-prepared due to stable quartz silica attained after annealing. In addition, the peak intensity at 533.2 eV from the reduced sample ascribed to oxygen in a stable SiO_2 has decreased as compared to that of as-prepared sample. However, more conclusive evidence of oxygen transport involved in the system during annealing is not available. At present, only an overall scenario can be drawn to verify the existence and

recrystallization of SiO_2 with higher temperature treatment as a result of hydrogen passivation.

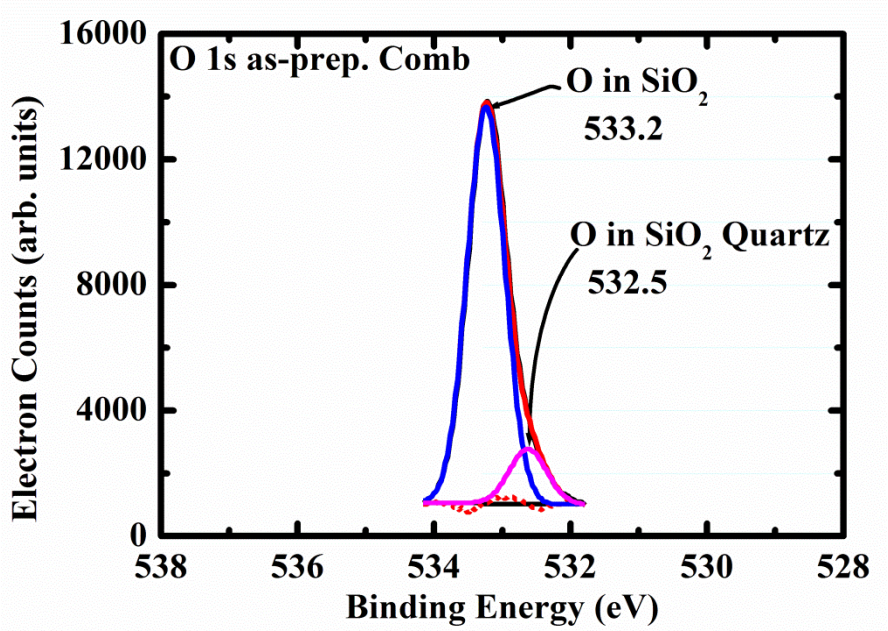

Figure 8-7 XPS spectrum of O 1s in as-prepared SiO_2

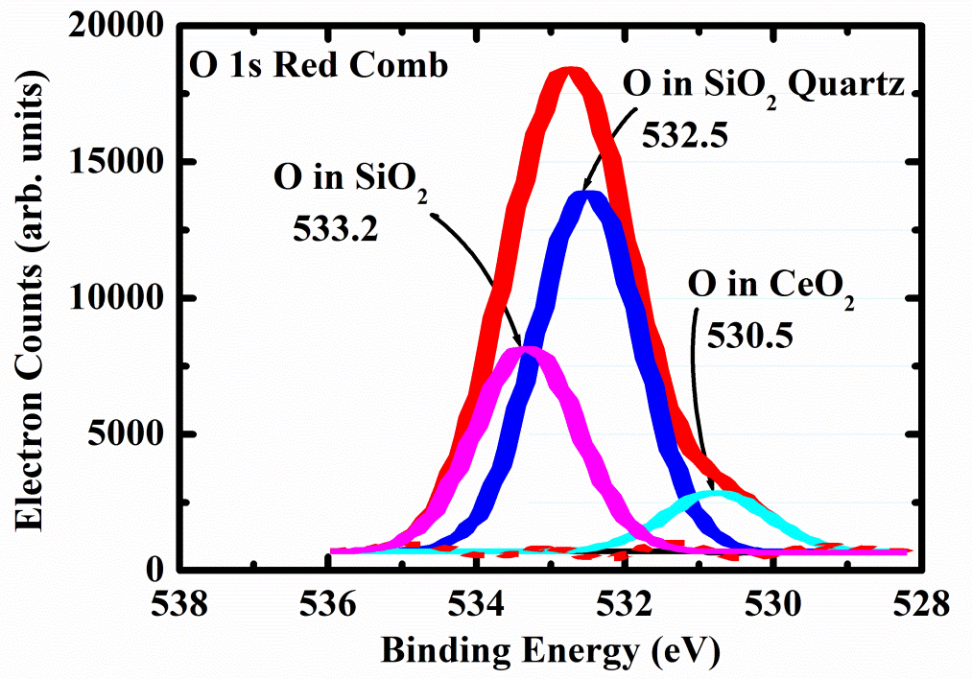

Figure 8-8 XPS spectrum of O 1s in reduced SiO_2

In figure 8.9 and 8.10 the high resolution scans of Si 2p from the as-prepared sample and reduced sample are shown respectively. In the as-prepared sample the Si 2p peak

was fitted with two peaks with the maxima at 102.2 and 103.3 eV binding energies. The peak at 102.2 eV can be ascribed to silicon in $SiO_{1.02}$ which suggests existence of the oxygen deficiency in silica matrix. On the other hand, the peak at 103.3 eV can be assigned to silicon in the stable SiO_2. In figure 8.10 the peak of Si 2p from the reduced sample has been fitted into three peaks with the maxima at 102.2, 103.3 and 104.0 eV respectively. In the reduced sample the peak at 103.3 eV has been decreased compared to that of as-prepared sample. At the same time one can observe the presence of the new peak at 104.0 eV which is ascribed to silicon into SiO_x and comes about because of the uncontrolled combustion reaction.

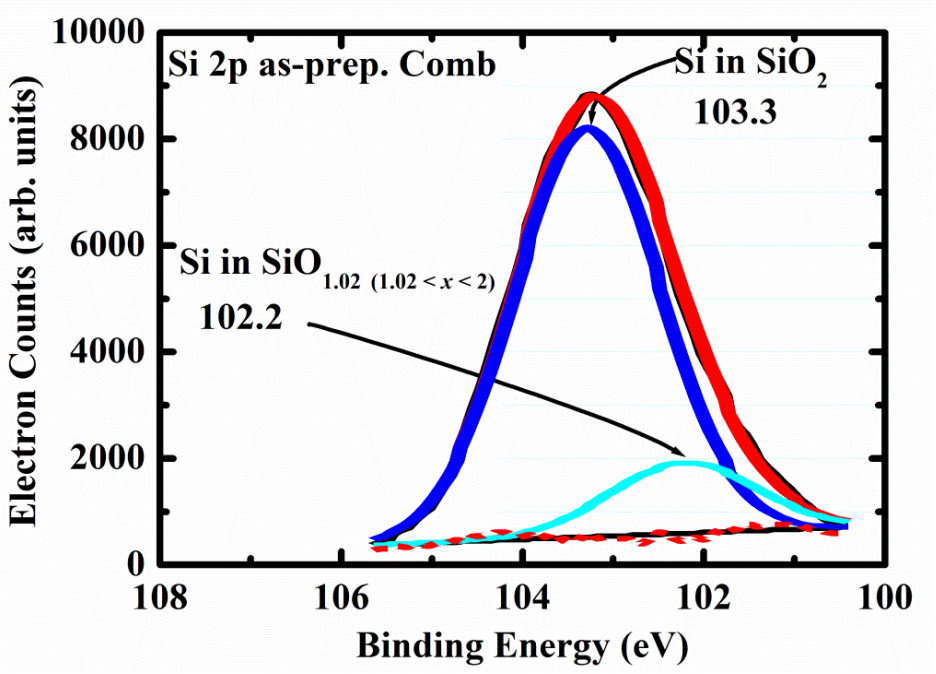

Figure 8-9 XPS spectrum of Si 2p in as-prepared SiO_2

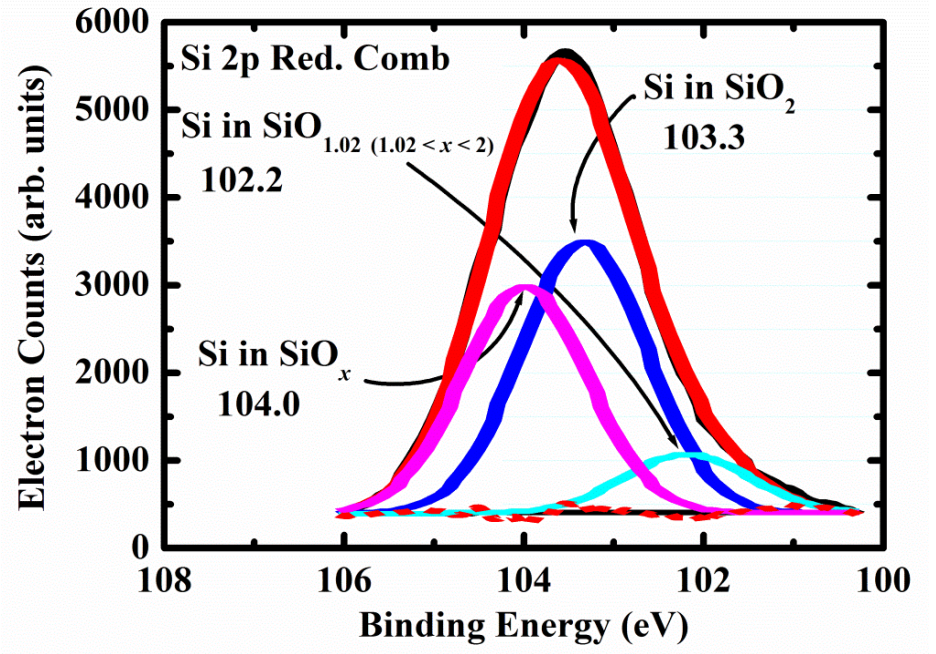

Figure 8-10 XPS spectrum of Si 2p in a reduced SiO_2

8.4 Conclusion

The phosphor powders of SiO_2, SiO_2: Ce, SiO_2: Tb and SiO_2: Ce,Tb were successfully synthesized using urea assisted combustion route and later reduced in a mixture of 4%H_2/96%Ar at 1000°C for 2 hrs. The XRD data from a singly doped SiO_2:2mol%Ce^{3+} and co-doped samples show a broad peak and some small signatures emanating from low quartz silica. The observed peaks were assigned by comparing the JCPDS database file no 86-1565 [17], which is the characteristic diffraction pattern of the low quartz's phase of a SiO_2 glassy matrix. The SEM images showed the agglomerated platelet-like particles of SiO_2: Ce and SiO_2:Ce, Tb with encrusted small spheroidal particles. Due to the incorporation of Ce^{3+} and Tb^{3+} ions in the silica host, efficient energy transfer from Ce^{3+} to Tb^{3+} ions was observed when the phosphor powders were excited by 322 nm wavelength. The transfer rate was then more efficient due to the reducing atmosphere. Thus, the maximum energy transfer was observed from the sample co-doped with SiO_2: 2 mol%Ce^{3+}, 4 mol%Tb^{3+}. The XPS studies confirm an improved conversion of Ce^{4+} ions into Ce^{3+} ions into silica matrix after annealing in a reduced atmosphere.

8.5 Reference

[1] D. Ban, J. Xue, R. Fang, S. Xu, E. Lu, P. Xu, *J. Vac. Sci. Technol*. **B 16** (1998) 989–995.

[2] Ichiro Tanahashi, Hideyuki Inouye, Koichiro Tanaka, Akihiro Mito, Jpn. *J. Appl.Phys*. **38** (1999) 5079–5082.

[3] X. Song, N. Jiang, Y. Ding, Y. Qu, G. Qiu, *J. Nanoeng. Nanosyst*. **222** (2008) 1–4.

[4] O.M. Ntwaeaborwa, H.C. Swart, R.E. Kroon, J.R. Botha, P.H. Holloway, *J. Vac. Sci.Technol*. **A 25** (2007) 4–9.

[5] R. Reisfeld, J. Hormodaly, B. Barnett, *Chem. Phys. Lett.* **17** (1972) 248–251.

[6] G. Blasse, B.C. Grabmaier, *Luminescent Materials*, Springer-Verlag:, Berlin, Germany, 1994 (Chapter 2–4).

[7] G.E. Malashkevich, G.I. Semkova, A.P. Stupak, A.V. Sukhodolov, *Phys. Solid State* **46 (8)** (2004) 1425–1431.

[8] R. Reisfeld, A. Patra, G. Panczer, M. Gaft, *Opt. Mater*. **13** (1999) 81–88.

[9] R. Reisfeld, H. Minti, A. Patra, D. Ganguli, M. Gaft, *Spectrochim Acta* **A 54** (1998)2143–2150.

[10] L.F. Koao, H.C. Swart, E. Coetsee, M.M. Biggs, F.B. Dejene, *Physica B., Phys. Condens. Matter* **404** (2009) 4499–4503.

[11] Q. Meng, H. Zhang, S. Wang, L. Fu, Y. Zheng, K. Yang, *Mater. Lett.* **45** (2000) 213–216.

[12] T. Kim, Y. Yoon, Y. Kil, Y. Hwang, H. Chung, I.N. Kim, Y. Ahn, *Mater. Lett.* **47** (2001) 290–296.

[13] M. Nogami, T. Enomoto, T. Hayakawa, *J. Lumin*. **97** (2002) 147–152.

[14] O.M. Ntwaeaborwa, P.H. Holloway, *Nanotechnology* **16** (2005) 865–868.

[15] I.M. Nagpure, Shreyas S. Pitale, K.G. Tshabalala, Vinay Kumar, O.M. Ntwaeaborwa, J.J. Terblans and H.C. Swart, *Materials Research Bulletin* **46** (2011) 2359-2366.

[16] Lijuan W, Anhuai L, Changqiu W, Xishen Z, Dongjun Z and Rui L *J. Colloid Interface Sci.* **295 (**2006) 436.

[17] Powder Diffraction File Card No.86-1565, *International Center for Diffraction Data*, Newtown Square, PA, 1990.

[18] Lu Xi-Hong, Li Gao-Ren, Yu Xian-Lan and Tong Ye-Xiang, *Electrochemical and Solid-State letters* **11** (9) (2008) K86.

[19] R.E Kroon, HAA Seed Ahmed, O.M Ntwaeaborwa, L.F Koao, I.M Nagpure, M.A Gusowski, J.R Botha and H.C Swart, *Physica **B*** **407** (2011) 1596.

[20] HAA Seed Ahmed, O.M Ntwaeaborwa, M.A Gusowski, J.R Botha and R.E Kroon *Physica **B*** **407** (2012) 1654.

[21] B.S. Barros, P.S. Mellow, R.H.G.A. Kiminami, A.C.F.M. Costa, G.F. de Sá and S. Alves Jnr, *J. Mater. Sci.* **41** (2006) 4744-4748.

[22] Multipak Version 9, Physical Electronics, Inc., Chanhassen, USA, 2006-2010

CHAPTER 9 STRUCTURE AND LUMINESCENCE PROPERTIES IN AMOPHOURS SiO_2: Ce^{3+}, Tb^{3+}

9.1 Introduction

Silica is widely used in so many fields such as medium layer and silicon-based photoelectron material because of its excellent chemical and thermal stability as well as interfacial combination with silicon semiconductor. SiO_2 doped with metal ions can also be studied as a luminescence material. The rare earth or transition metal ions [1-4] are often used as activator ions to act as luminescent centres in silica because of their unique electronic structures. For example, Tb^{3+} ions due to their extensive use as materials for fabricating various optical re-radiators and cathodoluminescent screens when incorporated into glasses have developed great interest for many researchers [5,6]. However, the problem of enhancing the light output of Tb^{3+} - containing glasses upon UV excitation still remains unresolved. The reason is that the light output of these materials is limited by the occurrence of intense absorption bands in the high-frequency range due to $4f^8 \rightarrow 4f^7(^8S_{7/2})5d^1(T_2)$ and $4f^7(^8S_{7/2})5d^1(E)$ inter configurational transitions [7] and a relatively low efficiency of excitation transfer from the luminescence sensitizers. In this work we have synthesized amorphous SiO_2 host doped with Ce^{3+} and Tb^{3+} ions to investigate how best the energy transfer rate can be improved between Ce and Tb ions such that absorption of ultraviolet (UV) photons can be fully utilized to give an efficient output of visible emission through Tb ions. Thus, the optimal concentrations from the combination of Ce/Tb ions incorporated into silica matrix to produce high energy transfer rate will be investigated.

9.2 Experimental procedure

The phosphor powder SiO_2, SiO_2:2mol%Ce, SiO_2:4mol%Tb and co-doped SiO_2:2mol%Ce, 4mol%Tb samples were prepared by the sol-gel process from the following starting materials: Tetraethylorthosilicate (TEOS), distilled water, ethanol (as a solvent) and nitric acid to catalyze the chemical reaction. After a vigorous stirring on a hot plate maintained at 40ºC, the gel was formed and was then transferred into an open flat-disc like container and was allowed to dry at room temperature. The dried gel was ground by using a pestle and mortar and was later annealed in a reducing atmosphere composed of 4% H_2 and 96% of Ar gas at 1000ºC for 2 hours. The structure of phosphor powder samples was characterized by X-ray powder diffraction (XRD) using a Bruker D8 Advanced powder diffractometer with Cu-Kα radiation (λ = 1.5418 Å) in the 2θ range from 10° to 60°. The photoluminescence (PL) properties of the powder phosphors were characterized using a Cary Eclipse fluorescence spectrophotometer.

9.3 Results and discussion

9.3.1 *X-ray diffraction*

Figure 9.1 show the XRD patterns of the sol-gel derived pure SiO_2, singly doped SiO_2:2mol%Ce^{3+} and SiO_2: 4mol%Tb^{3+} phosphor powders respectively. The broad band peak at 2θ ~ 23.6° is observed in all three XRD profiles. This peak is associated with high amorphous scattering background from SiO_2 [8,9]. The only exception here is that XRD profile from SiO_2:2mol%Ce derived from sol-gel is completely amorphous when compared with SiO_2:2mol%Ce derived from the combustion since there are some traces of crystalline peaks suggesting that there is transformation from disordered structure to ordered as shown in the previous chapters.

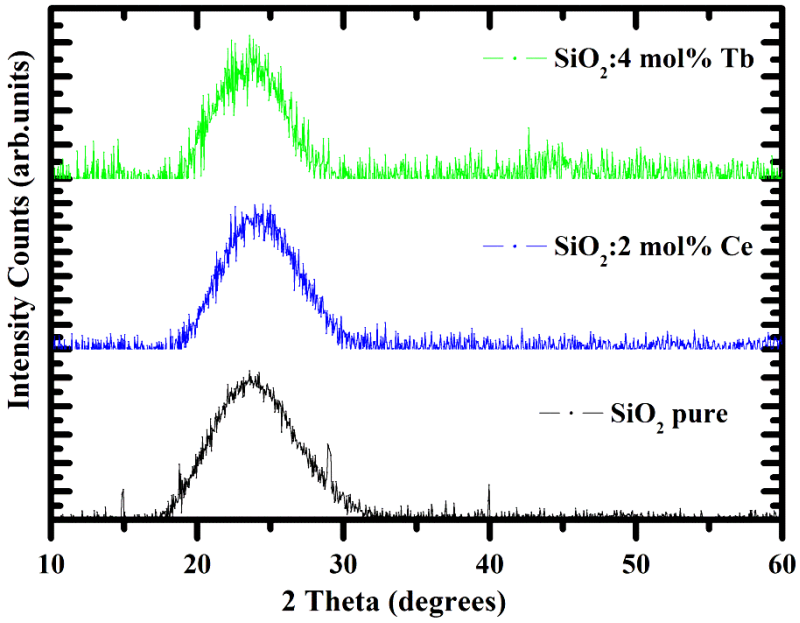

Figure 9-1 Room temperature XRD patterns of (as cast) pure SiO_2, a singly doped SiO_2:2mol%Ce^{3+} and singly doped SiO_2:4 mol%Tb^{3+} from Sol-gel derived route.

9.3.2 *Photoluminescence studies*

In figure 9.2 the emission spectrum of SiO_2:2mol% Ce (λ_{exc} = 227 nm) is presented. The broad emission peak is centered at 410 nm and is ascribed to the characteristic emission from Ce. The peak intensity of this emission is weak when compared to SiO_2:2mol% Ce in low quartz silica presented in chapter 8 (Fig. 8.4). Figure 9.3 present the emission spectra of singly doped SiO_2:4mol% Tb and co-doped SiO_2:2mol% Ce, 4mol% Tb, respectively. The excitation wavelength 227 nm gives well improved emissions from both singly doped SiO_2:4mol% Tb and co-doped samples in amorphous phase compared to low quartz silica (see Fig. 8.3). Even though the trend of the singly doped SiO_2:4mol% Tb in amorphous and low quartz is the same, the better response is evident in amorphous silica. On the other hand, figure 9.4 and 9.5 show PL emissions (λ_{exc} = 322 nm) of singly doped SiO_2:2mol% Ce, singly doped SiO_2:4mol% Tb and co-doped SiO_2:2mol% Ce, 4mol% Tb samples, respectively. The sample doped with cerium (Figure 9.4) exhibited a good photoluminescence spectrum under 322 nm excitation (a common excitation for Ce). In figure 9.5 the co-doped sample shows also a very good photoluminescence spectrum under the excitation of 322 nm. The efficient

energy transfer rate from Ce to Tb is clearly observed from the co-doped sample. At the same time, emission from singly doped terbium is relatively weaker. In conclusion, the high efficient energy transfer rate from Ce to Tb is more favourable in amorphous silica compared to low quartz. This has been seen from the photoluminescence analysis where the co-doped sample from amorphous silica shows a high transfer rate that is four times higher than that of low quartz.

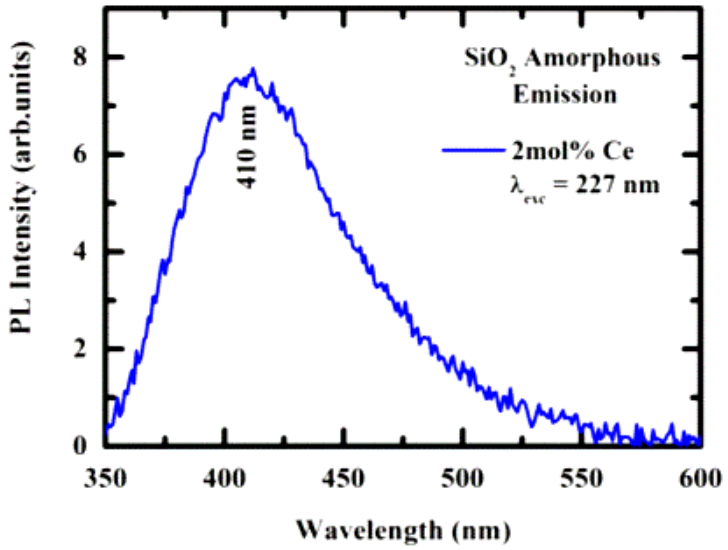

Figure 9-2 PL emission spectra SiO_2:2 mol% Ce (λ_{exc} = 227 nm).

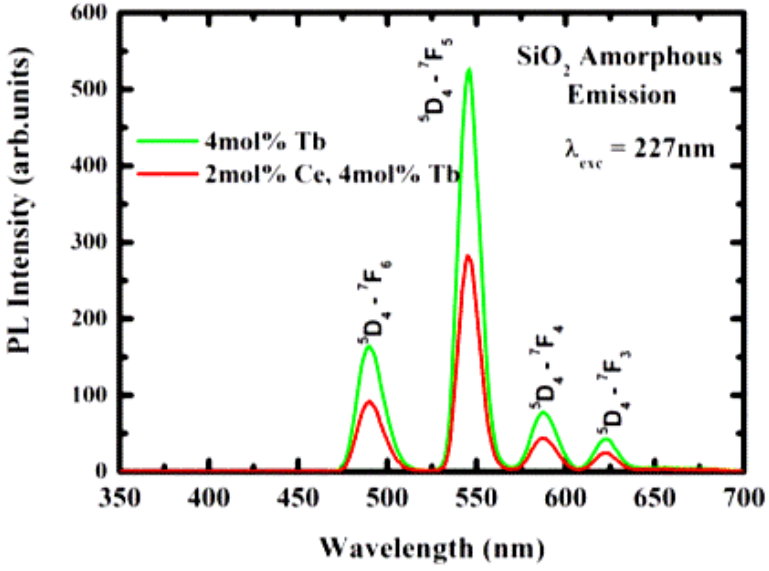

Figure 9-3 PL emission spectra of SiO_2 singly doped with 4 mol%Tb^{3+} and co-doped with 2mol%Ce^{3+} and 4mol%Tb^{3+} under excitation at 227 nm.

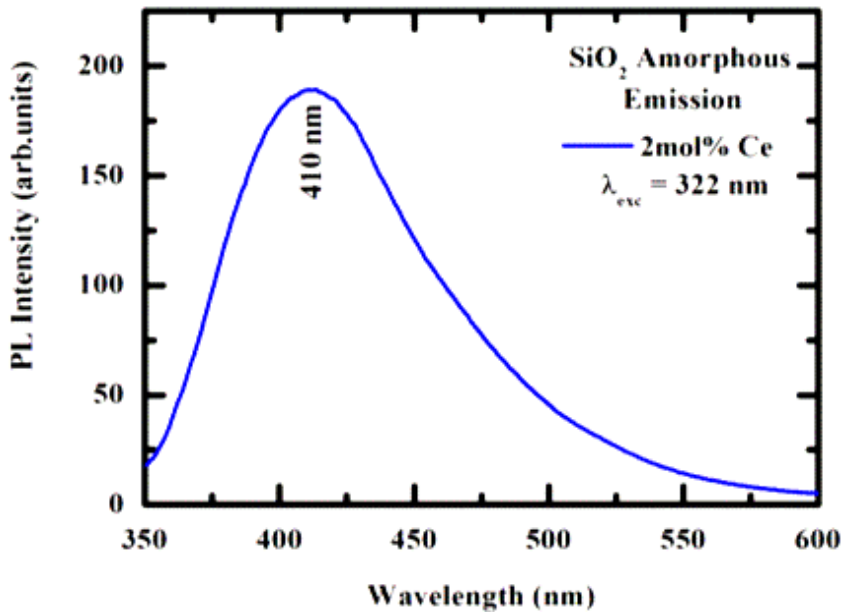

Figure 9-4 PL emission spectra of SiO_2 singly doped 2 mol%Ce^{3+} under excitation at 322 nm.

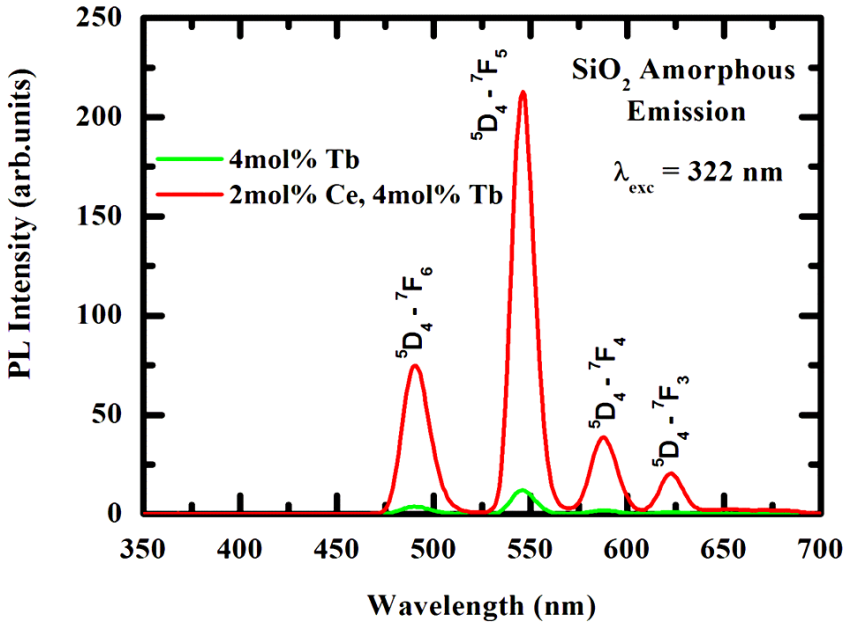

Figure 9-5 PL emission spectra of SiO_2 singly doped 4 mol%Tb^{3+} and co-doped with 2mol%Ce^{3+} and 4mol%Tb^{3+} under excitation at 322 nm.

9.4 Conclusion

The phosphor powders of pure SiO_2, singly doped cerium, singly doped terbium and co-doped samples were successfully prepared by sol-gel method. The XRD studies have confirmed that all powder samples were amorphous by exhibiting a broad peak at $2\theta \sim 23.6°$. Photoluminescence emission from the sample excited by 227 nm exhibits an improved emission from both singly doped and co-doped samples in amorphous silica as compared to its counter parts (low quartz) discussed in chapter 8. On the singly doped SiO2:Ce the emission from the excitation of 227 nm is relatively weaker compared to an excitation of 332 nm because it's attributed to the direct excitation of Ce due to 4f−5d transition. Thus, the efficient energy transfer rate is more evident when the excitation of 322 nm is used compared to 227 nm excitation. . Thus, the PL intensity of the green emission was maximum for 4 mol% Tb co-doped with 2 mol% Ce.

9.5 References

[1] C.E Chryssou, A.J Kenyon and C.W Pitt *Mater. Sci. Eng.* **B 81 (**2001) 16.

[2] M. Ferrari and C. Armellini *J. Sol-Gel Sci. Technol* **19** (2000) 569.

[3] M. Morita, S. Kajiyama , T. Kai, D. Rau and T. Sakurai *J. Lumin*. **94** (2001) 91.

[4] M.A Garcia, E. Borsella, S.E Paje, J. Llopis, M.A Villegas and R. Polloni *J. Lumin*. **93** (2001) 253.

[5] G.S Maciel, A. Biswas and P.N Prasad *Opt. Commun.* **178** (2000) 65.

[6] G.S Martin, A.C Yanes, J. Mendez-Ramos, M.E Torres and V.D Rodriguez *J. Appl. Phys.* **89** (5) (2001) 2520.

[7] V.I Arbuzov, V. Ya. Grabovaskins, N.S Kovaleva, U.T Rogulis and Tolstoĭ *Opt. Spectrosc.* **65** (1988) 555.

[8] W. Lijuan, L. Anhuai, W. Changqiu, Z. Xishen, Z. Dongjun and L. Rui *J. Colloid Interface Sci.* **295 (**2006) 436.

[9] U. Kalapathy, A. Proctor and J. Shultz, *Bioresour Technol.* **73 (**2000) 257.

CHAPTER 10 SUMMARY AND FUTURE WORK

10.1 Summary

This thesis reported on the solution combustion preparation of $ZnAl_2O_4:Ce^{3+}$, Tb^{3+} , $SiO_2:Ce^{3+}$, Tb^{3+}, and the sol-gel preparation of $SiO_2:Ce^{3+}$,Tb^{3+} of powder phosphors with different concentration of Ce^{3+} and Tb^{3+} ions. The energy transfer from Ce^{3+} ions to enhance Tb^{3+} green emission was investigated. The XRD and HRTEM were used to analyze the structure of the samples. The SEM was used for morphological analysis. The UV-Vis-NIR absorbance and diffused reflectance were obtained from the Varian Cary 100 Conc. UV-Vis and Perkin Elmer Lambda 950 UV-Vis spectrometers, respectively. The PL data were obtained from the continuous xenon-lamp Hitachi F7000 fluorescence and Cary Eclipse fluorescence spectrophotometers. The fluorescence decay data were recorded using an inverted-type scanning confocal microscope (MicroTime-200, Picoquant, Germany). A single-mode pulsed laser diode (375 nm wavelengths with an instrumental response function of ~240 ps in full-width at half maximum, 40 MHz repetition rate, and an average power of ~1 μW) was used as an excitation source. The CL data were obtained from the Physical Electron (PHI model 549) Auger electron spectrometer. The elemental composition analysis of the powder phosphors was carried out using X-ray photoelectron spectroscopy (XPS).

The face-centered cubic crystal structure of the $ZnAl_2O_4:Ce^{3+}$, Tb^{3+} powder phosphor was confirmed by the x-ray diffraction and HRTEM from selected area electron diffraction (SAED) patterns. The low-quartz structure from $SiO_2:Ce^{3+}$, Tb^{3+} prepared by solution combustion was also confirmed by x-ray diffraction. However, the SiO_2 powder phosphor prepared from sol-gel showed an amorphous structure even after the incorporation of Ce^{3+} and Tb^{3+} ions. The morphological properties of the $ZnAl_2O_4:Ce^{3+}$, Tb^{3+} powder phosphor

showed plate-like structure that had little porosity distribution due to the excess of gas liberation during the combustion reaction. Low quartz SiO_2 doped with different concentrations of Ce^{3+} and Tb^{3+} showed an agglomerated morphology with small particles distribution.

The intense absorptions at the wavelength of 358 and 360 nm in pure $ZnAl_2O_4$ as-prepared and annealed samples were observed, respectively. This absorption bands are known as a strong absorption of ZnO, and correspond to a charge-transfer process from the valence band (O 2p orbits) to the conduction band (Zn 4s orbits). Thus, the presence of ZnO was confirmed in this powder phosphors. As a result, it was evident from the XRD profile at $2\theta \sim 34.7^{o}$. On the other hand, the diffused reflectance from low quartz SiO_2 sample showed weak absorption bands at 240 and 310 nm attributed to Si−O intrinsic defects absorption. Equally, the amorphous SiO_2 sample showed one absorption band at 220 nm also attributed to intrinsic defects. The estimated values of the band gaps from low quartz and amorphous samples were also obtained and the calculated values were 5.2 eV for low quartz and 5.3 eV for amorphous sample. The average band gap energy obtained between the two samples was found to be less than the theoretical band gap energy of SiO_2 (BG ~ 11.8eV). This shrinkage was attributed to impurity levels which were incidentally introduced in both conduction band as donors and valence band as acceptors.

The photoluminescence properties of $ZnAl_2O_4$: Ce^{3+}, Tb^{3+} showed an increased green emission line ($^5D_4 - {}^7F_5$) from Tb^{3+} as a result of Ce^{3+} co-doping. The fact that the increase in Tb^{3+} green line was simultaneous with the decrease in blue emission from Ce^{3+} suggests that excitation energy was transferred from Ce^{3+} to Tb^{3+}. As evidence of energy transfer, we demonstrated the shortening of the decay lifetime of Ce^{3+} in $ZnAl_2O_4$: Ce, Tb powder phosphor by 10.29 ns and we concluded that the shortening was a result of absorbed UV

photons at a rate faster than the radiative transition of Ce^{3+} states. The maximum intensity was obtained from the sample co-activated with 0.86 mol% of Ce^{3+} and 1.14 mol% of Tb^{3+} when the sample was excited at 230 nm. There were other excitation wavelengths used to excite the material. However, the output emissions were relatively less. These excitation wavelengths were then attributed to either direct excitation of Ce^{3+} or charge transfer from O^{2-} to Tb^{3+}. It can be concluded that the activator concentration and excitation wavelength are very important parameters for sensitized emission of phosphors by the ultra-violet (UV) down-conversion process. The CL intensity degradation data of $ZnAl_2O_4$:Ce^{3+}, Tb^{3+} suggested that the intensity was stable after a prolonged exposure to 2 keV electrons for 10 hours. This stability was attributed to the formation of non-luminescent protective Al_2O_3 layer formed according to the electron stimulated surface chemical reaction (ESSCR).

Photoluminescence from low quartz SiO_2: Ce^{3+}, Tb^{3+} powder reduced at 1000ºC showed a very weak energy transfer from Ce^{3+} to Tb^{3+} when the powder was excited by 227 nm wavelength, but when another excitation of 322 nm was used, then efficient energy transfer was observed. Therefore, the excitation wavelength of 322 nm was attributed to the direct excitation of Ce^{3+} ions while that of 227 nm was the well known excitation from Tb^{3+} ions. Furthermore, the maximum energy transfer rate was observed from the sample co-doped with SiO_2: 2mol% Ce^{3+}, 4mol% Tb^{3+}. Similarly, the PL of amorphous SiO_2: 2mol% Ce^{3+}, 4 mol% Tb^{3+} showed poor energy transfer from Ce^{3+} to Tb^{3+} under the excitation of 227 nm, but better than the low quartz SiO_2 counterparts. Efficient energy transfer rate from Ce^{3+} to Tb^{3+} was observed when an excitation wavelength of 322 nm was used, and this transfer rate was higher than that of the low quartz sample.

Generally, it has been discovered that through PL studies carried out in all these three systems; the $ZnAl_2O_4$: Ce,Tb system which was confirmed to be crystalline, showed better

responses of luminescence compared to both the low quartz and amorphous phases of silica based systems.

The XPS detailed scan of O 1s orbital, Al 2p orbital (as-prepared) and O 1s orbital, Al 2p orbital (annealed) respectively were fitted using the Multipak software. The XPS fitted data of O 1s before and after annealing confirmed that the lattice O 1s peak was stable at a binding energy (B.E) of 531.1 eV suggesting that the chemical state and hence electronic states were not affected by annealing in hydrogen atmosphere. The other satellite O 1s peaks obtained from as-prepared sample were at B.E ~ 528.5 eV and ~ 529.5 eV, and these peaks were assigned to binding energies of O 1s peak in Ce-O and Tb-O metallic oxides respectively. The detection of the metallic oxides suggested that there was most likely small traces of CeO_x and TbO_x ($x \leq 2$) present in both unannealed and annealed $ZnAl_2O_4$: Ce^{3+}, Tb^{3+} samples. Apart from the discovery of new satellite observed from O 1s electronic state, a new band at B.E ~ 532.6 eV was also observed and assigned to chemisorbed water and/or oxygen molecules from environmental moisture.

On the other hand, the fitted data of the Al 2p peak before and after annealing showed Al 2p peaks at lower binding energies (~ 74.2 eV) and these peaks were assigned to Al ions occupying the tetrahedral (IV) sites while the other Al 2p peaks at higher binding energies (~ 75.6 eV) were then assigned to the Al ions occupying the octahedral (VI) sites. Therefore, the XPS data confirmed that there was structural readjustment from inverse to normal spinel as a result of annealing in $ZnAl_2O_4$: Ce^{3+}, Tb^{3+}. Moreover, for low quartz XPS studies confirmed an improved homogeneous distribution of Ce^{3+} ions into the silica matrix after annealing in a reduced atmosphere. This improvement was evident from photoluminescence studies because all as-prepared samples did not give any emission which suggested that Ce^{4+} population was very large and well known to be optically inactive.

10.2 Future Work

It is reported that the structure of $ZnAl_2O_4$ as a host material can be obtained with the special features of a normal spinel or spinel inversion. This behavior was observed from XPS studies as a result of the heat treatment in a reducing atmosphere. The potential of tuning the luminescence properties to the desired area of interest for application purposes can sometimes not be possible due to this. Therefore, further investigations to understand how this structural adjustment can be well controlled are very important to fully comprehend the luminescence properties of this phosphor. It is equally important to investigate the effect of the particle size and size distribution because in the first place, this material was chosen to be a down-converting phosphor where UV photons absorbed from the sun can be converted to visible range. The efficient conversion of light from UV range can entirely depend on the reduced light scattering due to the particle size.

To fully understand the nature of down-converting phosphor where UV light is converted to visible light emission due to different excitation sources, that is, (photons, electrons and synchrotron radiation); extensive investigations are needed. The factors leading to comparison to the performance of crystalline materials versus amorphous materials in order to efficiently down-convert the luminescence into visible region with high external quantum efficiency (EQE) needs further investigations. Interestingly, take into consideration that down-converting phosphor can serve as a potential application for solar cells; it requires a lot of examinations. Furthermore, since the EQE of a solar cell is equally important when experimental devices are being designed, it will be good to carry out further investigations. This is because EQE gives valuable information about how effectively a photon at a specific incident wavelength is converted into *e-h* pair.

10.3 Publications

- **Physica B: Condensed Matter (5 Citation)**

Volume 407, Issue 10, 15 May **2012**, Pages 1489-1492

Luminescence properties of Ce^{3+} and Tb^{3+} co-activated $ZnAl_2O_4$ phosphor

K.G. Tshabalala, S.-H. Cho , J.-K. Park, Shreyas S. Pitale, I.M. Nagpure, R.E. Kroon, H.C. Swart ,O.M. Ntwaeaborwa

- **Journal of Vacuum Science & Technology B (0 Citation)**

Volume 30, Issue 3, March **2012**, 6 Pages 031041

Enhanced green emission from uv down-converting Ce^{3+}–Tb^{3+} co-activated $ZnAl_2O_4$ phosphor

K. G. Tshabalala, I. M. Nagpure, H. C. Swart, O. M. Ntwaeaborwa, S.-H. Cho, and J.-K. Park

- **Materials Research Bulletin (1 Citation)**

Volume 46, Issue 12, December **2011**, Pages 2359-2366

Luminescence response and CL degradation of combustion synthesized spherical SiO_2:Ce nanophosphor

I.M. Nagpure , Shreyas S. Pitale, **K.G. Tshabalala**, Vinay Kumar, O.M. Ntwaeaborwa,

J.J. Terblans, H.C. Swart

- **Journal of Alloys and Compounds (21 Citation)**

Volume 509, Issue 41, October **2011**, Pages 10115-10120

Luminescent properties and X-ray photoelectron spectroscopy study of $ZnAl_2O_4$:Ce^{3+},Tb^{3+} phosphor

K.G. Tshabalala, S.-H. Cho, J.-K. Park , Shreyas S. Pitale, I.M. Nagpure, R.E. Kroon, H.C. Swart ,O.M. Ntwaeaborwa

- **Journal of Physics and Chemistry of Solids (0 Citation)**

Volume 71, Issue 3, March **2010**, Pages 181-186

Magnetic substitution in $CeIn_3$

Moise Bertin Tchoula Tchokonté, **Kamohelo George Tshabalala** , Paul de Villers du Plessis and Dariusz Kaczoroski

10.4 International Conferences

- AVS 58th International Symposium & Exhibition, Nashville, Tennessee (USA). October 2011

  Enhanced green emission from UV down-converting Ce^{3+}-Tb^{3+} co-activated $ZnAl_2O_4$ phosphor

  K.G. Tshabalala, S-H Cho, J-K Park, H.C Swart and **O.M. Ntwaeaborwa**

- 20th New Materials Symposium, Material Research Society of Korea-Spring Conference May 2011

  Luminescence properties of C^{3+}/Tb^{3+} co-activated $ZnAl_2O_4$ phosphor

  K.G Tshabalala, S-H Cho, J-K Park, S. Pitale, I.M. Nagpure, R.E. Kroon, H.C. Swart and O.M. Ntwaeaborwa

- International Conference on the Science and Technology of Emissive Displays and Lighting-St. Petersburg Institute of Technology, Russia. September 2010

  Photoluminescence properties of Ce^{3+} and Tb^{3+} doped $ZnAl_2O_4$ phosphors prepared by combustion method

  K.G. Tshabalala, S-H Cho, J-K Park, S. Pitale, I.M. Nagpure, H.C. Swart and **O.M. Ntwaeaborwa**

- 6th EBASI International Conference on Physics & Technology for Sustainable development in Africa, iThemba LABS (Cape Town), January 2007

  Magnetic Substitution in $CeIn_3$

  K.G. Tshabalala, M.B. Tchoula Tchokonte and P de V. du Plessis

10.5 National Conferences

- 57th Annual Conference of South African Institute of Physics (SAIP), hosted by Univ. of Pretoria (UP), Pretoria, 09−13 July 2012

  Energy transfer from Ce^{3+} to Tb^{3+} in low quartz and amorphous SiO_2 hosts

  K.G. Tshabalala, H.C. Swart and O.M. Ntwaeaborwa

- 56th Annual Conference of South African Institute of Physics (SAIP), hosted by UNISA, St Georges Hotel and Convention Centre, Pretoria, 12−15 July 2011

  Enhanced green emission line from co-activated $ZnAl_2O_4:Ce^{3+}/Tb^{3+}$ phosphor

  K.G. Tshabalala, S-H Cho, J-K Park, I.M. Nagpure, H.C. Swart and O.M. Ntwaeaborwa

- 55th Annual Conference of South African Institute of Physics (SAIP), hosted by CSIR NLC, Pretoria, 27 September−01 October 2010

  Luminescence properties of Ce^{3+} and Tb^{3+} –doped $ZnAl_2O_4$ phosphors prepared by combustion reaction and effect of post annealing

  K.G. Tshabalala, S-H Cho, J-K. Park, H.C. Swart, S Pitale, I.M Nagpure and O.M. Ntwaeaborwa

- 54th Annual Conference of South African Institute of Physics (SAIP), hosted by Univ. of Kwa-Zulu Natal, KZN, 06−10 July 2009

  In attendance

- 52nd Annual Conference of South African Institute of Physics (SAIP), hosted by Univ. of Witwatersrand, Johannesburg, July 2007

  Electrical resistivity of the Kondo lattice systems $(Ce_{1-x}RE_x)In_3$, RE = Gd, Tb and Dy $(0 \leq x \leq 1)$

  K.G. Tshabalala, M.B. Tchoula Tchokonte and P. de V. du Plessis

10.6 BIOGRAPHY

Kamohelo George Tshabalala was born and grew up at Thaba-Bosiu Village Qwa-Qwa in the Eastern Free State Province, Republic of South Africa (RSA). He joined University of the North (UNIQWA) in 2000 as a student and obtained his BSc degree in Physics in 2003. He was appointed as a Laboratory Technician at University of the Free State (QwaQwa campus) after the merger between Free State University and UNIQWA in February 2004. He joined University of the Western Cape in 2005 as an Honours student. In, 2006 he enrolled for MSc in Material Science at University of the Western Cape. He joined University of the Free State (Bloemfontein) in 2009 as a PhD student and later in 2012 was appointed as a Physics Lecturer at Qwa-Qwa Campus. He was a research scholar at Korea Institute of Science and Technology (KIST) –South Korea in 2010 and 2011 respectively, working with Drs So-Hye Cho and Jong-Ku Park on preparation and characterization of luminescent down-conversion nanoparticle phosphors for solar cells application.

Kamohelo George Tshabalala has published 5 articles in internationally accredited journals. He is currently the Subject Head at Physics Department Qwa-Qwa Campus. He was recommended by Prof. Martin Ntwaeaborwa to be a co-supervisor for the students doing an Honours projects and at the same time a co-promoter of the PhD candidate in 2014. He has given over 5 talks at national and international conferences including South African Institute of Physics.

He is an upcoming researcher working on luminescent nanoparticle materials for solar cells application in collaboration with Dr So-Hye Cho (Department of Nano-Materials Science, Korea Institute of Science and Technology). The other avenues of his research are to explore biomedical applications, optical and luminescent properties of quantum dots. This work will be done in collaboration with Prof. Simon Dhlamini (Department of Physics: University of South Africa-Florida Campus).